Experiments on the laminar to turbulent transition under unsteady inflow conditions

A thesis accepted by the Faculty of Aerospace Engineering and Geodesy of the University of Stuttgart in partial fulfillment of the requirements for the degree of Doctor of Engineering Sciences (Dr.-Ing.)

by

Jonas Romblad

born in Österhaninge, Sweden

Main referee:	Prof. Dr.-Ing. E. Krämer
Co-referee:	Prof. Dr.-Ing. C. Tropea
Date of defense:	4 May 2023

Institute of Aerodynamics and Gas Dynamics
University of Stuttgart
2023

Acknowledgements

This thesis was prepared during my time as doctoral researcher at the Institute of Aerodynamics and Gas Dynamics (IAG) of the University of Stuttgart. The main part of the research was conducted in the project "Laminar-turbulente Transition unter instationären Anströmbedingungen" (LTT), Förderkennzeichen 20E1503C in the Luftfahrtforschungsprogramm LUFOV2-790-217 of the Bundesministerium für Wirtschaft und Energie.

I would like to thank my main supervisor Prof. Dr.-Ing. Ewald Krämer for the opportunity to perform the work presented in this thesis. The inspiring and creative atmosphere at the IAG is a result of his efforts.

Special thanks goes to Prof. Dr.-Ing. Cameron Tropea and apl. Prof. Dr.-Ing. Ulrich Rist for ensuring the excellent collaboration with the flight testing and numerical parts of the LTT-project and for fruitful technical discussions. Prof. Tropea also graciously accepted the role of co-referee for this thesis and provided valuable feedback on the manuscript.

I am particularly grateful to Dr. Ing. Werner Würz, who has made the Laminar Wind Tunnel group an extraordinary place to work by creating a very positive and friendly atmosphere as well as by generously sharing his vast knowledge. He will continue to be a great source of inspiration in topics related to both work and to spare time. Thank you for taking me onboard and for guiding me along the journey!

The colleagues at the Laminar Wind Tunnel group have meant a lot during my years at the institute and they have all earned special thanks. Marion Langohr-Kolb for her positive attitude and never-ending willingness to help and Christian Vetter for his reliable support. Michael Greiner for inspiring discussions and a healthy portion of humor, Ulrich Deck for new insights in glider flying and Dominic Seyfert for enthusiastically taking over the autoKite project. The model-makers Jürgen Lutz, Joachim Umbeer and Peter Jost for skillfully creating airfoil models and other devices. I am also very grateful for the help from Armin Baur and Stefan Hans in the mechanical workshop.

It has been a pleasure to work with my partners in the LTT project, Duncan Ohno who performed the very challenging numerical work, and Timo Nemitz

and Amandine Guissart at TU Darmstadt who conducted the likewise difficult flight measurements.

I would like to thank Regina Antunes for her highly skilled way of dealing with project administration, thereby making my life a lot easier. Partly on the same note, Klaus Heudorfer's expertise in managing the projects KiteFlug and autoKite, both administratively and technically, will remain an inspiration in the future.

Finally, I would like to thank my family and friends, in particular my father for always encouraging my curiosity and Sonia for making this thesis possible.

Contents

Nomenclature

Abbreviations

AC	Alternating current
AD	Analog to digital
AoA	Angle of attack
CWT	Contiuous wavelet transform
DC	Direct current
DNS	Direct numerical simulation
DVA	Disturbance velocity approach
FFT	Fast Fourier transform
IAG	Institute of Aerodynamics and Gas Dynamics
IR	Infrared
LST	Linear stability theory
LWT	Laminar wind tunnel
NACA	National Advisory Comittee for Aeronautics
PSD	Power spectral density
RANS	Reynolds averaged Navier-Stokes
RMS	Root mean square
TS	Tollmien-Schlichting
URANS	Unsteady Reynolds averaged Navier-Stokes

Greek letters

α	Angle of attack	$^\circ$
α_{20}	Temperature coefficient of resistance	Ω/K
α_{gen}	Angle of attack, gust generator	$^\circ$
α_i	Growth rate in streamwise direction	1/mm
α_{inflow}	Inflow angle	$^\circ$
α_{main}	Angle of attack, main airfoil	$^\circ$
α_{min}	Upstream turning point for $x_{tr}(t)$	$^\circ$
α_{max}	Downstream turning point for $x_{tr}(t)$	$^\circ$
α_{ref}	Reference angle of attack	$^\circ$
δ	Boundary layer thickness	mm
δ_1, δ^*	Boundary layer displacement thickness	mm
δ_2	Boundary layer momentum thickness	mm

ε	Dissipation rate	m^2/s^3
η	Kolmogorov length scale	m
κ	Reduced frequency, $\kappa = \frac{\pi f c}{U_\infty}$	-
κ_{trans}	Modified reduced frequency	-
Λ	Integral length scale	m
λ	Taylor length scale	m
μ	Dynamic viscosity	Pa·s
ν	Kinematic viscosity	m^2/s

Latin letters

A	Constant in King's law	
a_r	Anisotropy ratio	-
B	Constant in King's law	
b	Anisotropy tensor	-
	Hot-wire overheat ratio	-
c	Airfoil chord	m
c_p	Pressure coefficient	-
C_3	Paramter in the M-TERA intermittency method	
d	Grid rod diameter	mm
E_{ii}	Energy spectrum in direction ii	$(m/s)^2/Hz$
f	Physical frequency	Hz
F	Non-dimensional frequency, $F = \frac{2\pi f \nu}{U_\infty^2}$	-
f_η	Kolmogorov frequency, $f_\eta = U_\infty/(2\pi\eta)$	Hz
	Term in Pope model spectrum	
f_{gen}	Frequency of gust generator oscillations	Hz
f_L	Term in Pope model spectrum	
G	Receptivity coefficient	
k	Turbulent kinetic energy	m^2/s^2
k_r	Receptivity coefficient ratio	-
k_z	Spanwise wavenumber	rad/m
M	Grid mesh width	mm
n	Amplitude ratio	-
	Constant in King's law	
n_{crit}	Critical n-factor	-
p'	Flucuating part of unsteady surface pressure	Pa
p_{grid}	Supply pressure to active grid	bar
p_{rms}	Short-time rms of unsteady surface pressure	Pa
Re	Reynolds number based on airfoil chord c	-
Re_λ	Micro-scale Reynolds number	-
Re_Λ	Macro-scale Reynolds number	-
Re_d	Reynolds number based on grid rod diameter d	-
Re_x	Transition Reynolds number based on laminar run	-

t	Time	s
T	Oscillation cycle period	s
	Temperature	$^{\circ}C$, $^{\circ}K$
$T_{inf.line}$	Transfer function, infinite line installation	-
Tu	Turbulence level	-
u, v, w	Velocity componenets in x, y and z direction	m/s
U_{∞}	Free-stream velocity	m/s
u_{ph}	Phase velocity	m/s
$u_{rms}, v_{rms}, w_{rms}$	RMS values of turbulence velocity components	m/s
$u_{tr,d}$	Velocity of downstream moving transition front	m/s
$u_{tr,u}$	Velocity of upstream moving transition front	m/s
v'	Gust amplitude	m/s
x, y, z	Cartesian coordinates, airfoil fixed	m
x_t, y_t, z_t	Cartesian coordinates, tunnel fixed	m
x_{tr}	Transition location	m
$x_{tr,mid,down}$	Mid-point of transition movement, downstr. moving	m
$x_{tr,mid,up}$	Mid-point of transition movement, upstr. moving	m
x_{ts}	x-coordinate, origin at the start of the test section	m

Subscripts

i	Imaginary part
i, j, n	Running indices
u, v, w	Velocity component
max	Maximum value
rms	Root mean square

Superscripts

s	Measured with single-wire hot-wire probe
x	Measured with x-wire hot-wire probe
*	Normalized quantity

Symbols

$^-$	Mean value
$'$	Perturbation

Abstract

Natural laminar flow (NLF) airfoils are key to the performance of sailplanes and wind turbines by providing a significant reduction of friction drag. The drag benefit is achieved by a long laminar run with delayed onset of transition to a turbulent boundary layer. However, the most commonly employed method for transition prediction in NLF airfoil design, the e^n method, has limited capabilities for taking typical operational conditions into account, including inflow turbulence.

The current work employs wind tunnel experiments to study how transition is affected by free-stream turbulence that is representative for the lower, convective part of the atmosphere. The atmospheric turbulence is separated into regions of length scales according to the mechanism by which it influences the transition. Small scales generate disturbances in the boundary layer, whereas large scales induce unsteady pressure distributions. In the wind tunnel, small-scale turbulence is generated by turbulence grids, and a gust generator induces inflow angle oscillations corresponding to large-scale turbulence. The impact of both regimes is explored separately, as well as in combination. As a prerequisite study, the turbulence generated by passive turbulence grids placed in the settling chamber is characterized in detail.

The response of the boundary layer on the pressure side of the MW-166-39-44-43 airfoil is investigated using hot-wire anemometry, infrared thermography and measurements of unsteady surface pressures. The Reynolds number $Re = 3.4 \cdot 10^6$ and airfoil pressure distribution is matched to cruise or dash flight of general aviation aircraft. The results are compared with direct numerical simulation, linear stability theory (LST) and flight measurements.

The influence of small-scale turbulence is studied in the range of longitudinal turbulence levels $0.01\% \leqslant Tu_u \leqslant 0.11\%$. In this range of Tu, free-stream turbulence enters the boundary layer through receptivity and acts as seeds for Tollmien-Schlichtung (TS-) modes. These modes are amplified until nonlinear interactions lead to breakdown to turbulence. With increasing Tu, a change is observed from quasi-uniform transition to structures showing isolated wave packets that grow into turbulent spots. This is likely caused by an interaction with Klebanoff modes. The critical n-factor $n_{crit}(Tu)$ of the MW-166-39-44-43 is nevertheless well predicted by the modified e^n method of Mack (1977). In contrast, the airfoils XIS40mod and NACA64-418 exhibit smaller, but still significant reductions of n_{crit} with increasing turbulence level. A simplified analysis indicates that the different sensitivity of the three

airfoils cannot be fully accounted for by presumed differences in the local receptivity coefficients only.

The effects of single-mode inflow angle oscillations are investigated in the range of reduced frequency $0.06 \leqslant \kappa \leqslant 1.7$. The inflow variations induce unsteady pressure distributions on the airfoil that, in turn, give rise to time-dependent mean boundary layer profiles and stability characteristics. As a result, the growth of the downstream travelling TS-modes deviates significantly from the steady case. The transition process changes from quasi-steady to clearly unsteady, but a fully convective transition mode is not formed. In this intermediate range of unsteady flow, trajectory-following LST captures the main features of the unsteady transition process.

In addition, the combined effects of inflow oscillations and increased turbulence level are explored. No significant interaction effects are observed in the investigated range of Tu and κ, indicating that the effects of the two types of unsteady inflow can be treated as essentially independent.

Kurzfassung

Durch die Verringerung des Reibungswiderstands tragen Laminarprofile wesentlich zur Leistungsfähigkeit von Segelflugzeugen und Windturbinen bei. Der Widerstandsvorteil ergibt sich aus einer langen laminaren Laufstrecke mit einem verzögerten Beginn der Transition hin zu einer turbulenten Grenzschicht. Die am häufigsten verwendete Methode zur Transitionsvorhersage beim Entwurf von Laminarprofilen, die e^n-Methode, kann jedoch die Turbulenz der Anströmung nur eingeschränkt berücksichtigen.

Die vorliegende Arbeit untersucht mit Hilfe von Windkanalmessungen, wie Freistromturbulenz, die für den unteren, konvektiven Teil der Atmosphäre repräsentativ ist, die Transition beeinflusst. Dazu wird die atmosphärische Turbulenz in unterschiedliche Längenskalen eingeteilt, anhand des Mechanismus, durch den sie auf die Transition wirkt. Kleine Skalen verursachen Störungen in der Grenzschicht, während große Skalen zu instationären Druckverteilungen führen. Im Windkanal wird kleinskalige Turbulenz mittels Turbulenzgitter erzeugt, wohingegen ein Böengenerator Anströmwinkelschwingungen erregt, die großskaliger Turbulenz entsprechen. Die Auswirkungen beider Regime werden sowohl einzeln als auch in Kombination untersucht. Dazu wird in einem ersten Schritt die Turbulenz, die von den in der Beruhigungskammer installierten passiven Turbulenzgittern erzeugt wird, genau charakterisiert.

Das Antwortverhalten der Grenzschicht auf der Druckseite des Profils MW-166-39-44-43 wird mittels Hitzdrahtanemometrie, Infrarot-Thermografie und dynamisch gemessenen Oberflächendrücken untersucht. Die Reynolds-Zahl $Re = 3,4 \cdot 10^6$ und die Druckverteilung auf dem Profil sind an den Reisebeziehungsweise Schnellflug von Flugzeugen der allgemeinen Luftfahrt angepasst. Die ermittelten Daten werden mit den Ergebnissen aus direkter numerischer Simulation, linearer Stabilitätstheorie (LST) und Flugmessungen verglichen.

Der Einfluss kleinskaliger Turbulenz wird im Bereich longitudinaler Turbulenzgrade von $0{,}01\% \leqslant Tu_u \leqslant 0{,}11\%$ untersucht. In diesem Tu-Bereich dringt die Freistrom-Turbulenz durch Rezeptivität in die Grenzschicht ein und verursacht Anfangsstörungen für Tollmien-Schlichtung (TS-) Moden. Diese Moden werden verstärkt, bis nichtlineare Wechselwirkungen zu Wirbelzerfall und turbulenter Grenzschicht führen. Mit zunehmendem Tu wird ein Übergang von einer nahezu gleichförmigen Transition zu Strukturen beobachtet, die aus isolierten Wellenpaketen bestehen und zu turbulenten Flecken anwach-

sen. Dies ist wahrscheinlich auf eine Wechselwirkung mit Klebanoff-Moden zurückzuführen. Der kritische n-Faktor $n_{crit}(Tu)$ des MW-166-39-44-43 wird dennoch durch die modifizierte e^n-Methode von Mack (1977) gut vorhergesagt. Im Gegensatz dazu zeigen die Profile XIS40mod und NACA64-418 eine geringere, aber immer noch signifikante Verringerung von n_{crit} mit zunehmendem Turbulenzniveau. Eine vereinfachte Analyse deutet darauf hin, dass die unterschiedliche Empfindlichkeit der drei Profile nicht allein durch anzunehmende Unterschiede in den lokalen Rezeptivitätskoeffizienten erklärt werden kann.

Die Wirkung von monomodalen Anströmwinkelschwingungen wird im Bereich reduzierter Frequenzen von $0{,}06 \leqslant \kappa \leqslant 1{,}7$ untersucht. Die Schwingung der Anströmrichtung führt zu wechselnden Oberflächen-Druckverteilungen, die wiederum zur Zeitabhängigkeit der phasen-gemittelten Grenzschichtprofile und der Stabilitätseigenschaften führen. Infolgedessen weicht die Anfachung der stromabwärts wandernden TS-Moden deutlich vom stationären Fall ab. Der Transitionsprozess ändert sich von quasistationär zu deutlich instationär, ein vollständig konvektiver Transitionsstyp wird jedoch nicht gebildet. In diesem Übergangsbereich instationärer Strömung werden die wesentlichen Merkmale des Transitionsprozesses durch trajektorienfolgende lineare Stabilitätstheorie (LST) gut wiedergegeben.

Zusätzlich wird der kombinierte Effekt von Anströmwinkelschwingung und erhöhtem Turbulenzniveau untersucht. In dem untersuchten Bereich von Tu und κ werden keine relevanten Wechselwirkungen beobachtet, was darauf hindeutet, dass die Effekte beider Arten instationärer Anströmung als im Wesentlichen voneinander unabhängig behandelt werden können.

1. Introduction

1.1. Motivation

Aircraft and wind turbines are two examples of machines for which viscous friction drag has a profound influence on the performance. Consequently, the reduction of friction drag is an important target in their design. The use of Natural Laminar Flow (NLF) airfoils provides a passive way to significantly decrease the friction drag through extended regions of laminar boundary layer flow. NLF airfoils are a well-established technology for glider aircraft (Boermans, 2006; Kubrynski, 2012) and wind turbine applications (Timmer & Van Rooij, 2003; Fuglsang & Bak, 2004). Pioneers in the use of NLF on commercial aircraft include the HondaJet (Fujino *et al.*, 2003) and the Piaggio P180 (Sollo, 2021), although the application to larger aircraft has been limited to the nacelle of the Boeing 787 and winglets for the Boeing 737Max, see for example (Crouch, 2015). Considerable efforts are being made to investigate a broader application of NLF airfoils to large transport aircraft, as exemplified by the full-scale flight tests with the BLADE demonstrator of the Clean Sky program, see Williams (2016).

The design of NLF airfoils heavily relies on fast and accurate prediction of the transition from laminar to turbulent boundary layer. The state of the art is the e^n method (Crouch, 2015) developed independently by Smith & Gamberoni (1956) and van Ingen (1956). In this method, linear stability theory (LST) is used to determine the amplification rates of Tollmien-Schlichting (TS-) waves and transition is predicted by a threshold value for the integral amplification, the critical n-factor or n_{crit}. This threshold is empirically adjusted to fit measured transition locations in low turbulence (i.e. "laminar") wind tunnels. Variable n-factor methods may be used to account for small-scale inflow turbulence (Mack, 1977; van Ingen, 1977) and/or receptivity properties (Crouch, 2008).

However, both general aviation aircraft and wind turbines operate in the lower part of the atmospheric boundary layer where the level of turbulence depends strongly on the amount of convection as well as on wind shear and terrain (Wyngaard, 1992). The turbulent energy is generated at very large scales that break up into progressively smaller and smaller eddies through the Richardson-Kolmogorov energy cascade, see Richardson (1922) and Kolmogorov (1941). This exposes airfoils to unsteady inflow with a wide range of length scales and amplitudes which, in general, should be accounted for in

the airfoil design process

The complexity and variability of the inflow turbulence contributes to the limited ability of current variable n-factor methods in covering the effects of inflow turbulence seen in flight. These methods are based on measurements in zero pressure gradient boundary layers, and in wind tunnel turbulence with more or less arbitrary spectral content. As demonstrated by Romblad *et al.* (2018), the transition development as function of the inflow turbulence depends on the base flow, and different airfoils exhibit different levels of sensitivity. A better physical understanding of the parameters influencing the laminar boundary layer response to low to moderate levels of freestream turbulence is needed to improve future transition models for NLF application.

1.2. State of the art

This section is divided in five parts that discuss literature relevant to the current thesis. First, the inflow experienced during flight in the convective part of the atmosphere is linked to the properties of the atmospheric turbulence. The different routes to transition in 2D boundary layers are then described, followed by a discussion of the response to turbulent inflow of the laminar boundary layer and the transition. Depending on the length scale of the turbulence, the mechanism by which it influences the boundary layer is different. Consequently, the response to small and large turbulence scales are discussed separately. Last, the combined effects of the two turbulence scales are addressed.

1.2.1. Atmospheric turbulence

The typical atmospheric turbulence has a characteristic spectrum that is well described by the energy cascade of the Kolmogorov hypothesis (Kolmogorov, 1941), where the turbulence can be separated into regions according to its length scale. Turbulence is created in the energy containing range in the form of large eddies. These eddies break up into progressively smaller ones in the inertial subrange, until finally transformed into heat by viscosity in the dissipative subrange (Pope, 2000). In the typical turbulence spectrum of the convective atmospheric layer, the wavelengths of the border region between the inertial subrange and the dissipative subrange approximately correspond to the most amplified frequencies in the boundary layer of a typical NLF airfoil.

The intensity and spectral distribution of the turbulence in the lower part of the atmosphere (the Ekman layer), that is influenced by convection, has been studied by researches from fields like meteorology, aircraft structures and wind energy. Li *et al.* (2014) published measurements in low wind conditions as well as strong winds (typhoon), Chougule *et al.* (2015) investigated the

difference between the turbulence over open terrain and forest while Bodini *et al.* (2018) used LIDAR to map the turbulence from the ground up to several hundred meters.

The characteristics of atmospheric turbulence have been investigated by measurements in flight since the 1950's, see e.g. Bunker (1955). The measurements of Bunker (1955) utilized the resulting vertical accelerations and changes of altitude of an aircraft flying through turbulence to deduce the rms velocities and the turbulent shear stress at altitudes up to 1460 m over the north Atlantic. An unusually wide range of length scales was covered by Sheih *et al.* (1971) through combining measurement on an aircraft with those from a meteorology mast. Otten *et al.* (1982) performed measurements of inflow turbulence in flight at altitudes between 3.7 and 12.5 km, finding turbulence levels (Tu) in the order of 0.02%. The very low levels are expected, since these measurements were conducted above the convective layer of the atmosphere. In the higher atmospheric layers, the turbulence intensity is typically small, often bordering to the resolution of the measurement equipment. In contrast, below the capping inversion, i.e. the cloud base, the turbulence is significantly stronger. Zanin (1985) used a glider to measure total turbulence levels $0.2\% \leqslant Tu \leqslant 0.6\%$ ($1 \leqslant f \leqslant 5000$ Hz) in clear air at altitudes from 100 m to 1200 m, the higher Tu-levels occurring close to the ground. Zanin (1985) also performed measurements inside clouds, recording $1.0\% \leqslant Tu \leqslant 1.4\%$. A compilation of measurements of atmospheric turbulence in a wide range of conditions can be found in Riedel & Sitzmann (1998), including both the lower atmosphere and altitudes up to 13716 m. One of the aircraft mentioned in Riedel & Sitzmann (1998), the G109B of the Technical University of Darmstadt, has seen continued use in a series of investigations. Several of those have focused on the atmospheric turbulence in the convective part of the atmosphere, and its influence on NLF airfoils, see Weismüller (2012), Reeh (2014) and Guissart *et al.* (2021). Weismüller (2012) and Reeh (2014) pointed at the influence of the large-scale turbulence on the boundary layer transition via unsteady fluctuations of the pressure distribution of the airfoil. Both Reeh (2014) and Guissart *et al.* (2021) also investigated the effect of small-scale turbulence on the boundary layer transition, and the results of Guissart *et al.* (2021) are used for detailed comparisons in this thesis. Even though stronger turbulence can be expected in the rising, convecting air of a thermal than in the surrounding air, few measurements distinguishing between these regions have been conducted. An exception is Greiner & Würz (2021), where extensive data collected during cross-country flights with a glider are presented and a detailed analysis is performed. The ranges of turbulence level as well as the frequency and amplitude of the inflow angle oscillations used in the present thesis are based on the measurements of Guissart *et al.* (2021) and Greiner & Würz (2021).

1.2.2. Boundary layer transition

The process of transition from laminar to turbulent boundary layer is strongly influenced by the level of forcing disturbances. Saric *et al.* (2002) give an overview of the many different paths to transition in the 2D boundary layers on straight or very slightly swept wings, and summarizes them as shown in Fig. 1.1. At low levels of forcing disturbances, the transition is driven by the exponential amplification of primary Tollmien-Schlichting modes, followed by secondary instabilities and finally breakdown to turbulence. This type of transition is sometimes referred to as "orderly" transition, see Durbin (2017). In contrast, the transition at high levels of forcing disturbances is dominated by spanwise modulated streaks, the so called Klebanoff modes or streaky structures that grow linearly and break down to turbulence without exhibiting the different stages of the "orderly" transition. This type of transition is often referred to as "bypass transition". At intermediate levels of forcing disturbances, the superposition of slightly damped, non-orthogonal modes (mainly TS- and Squire modes) result in growth that tend to be local in space and time, the so-called transient growth (Reshotko, 2001). The high disturbance amplitudes caused by transient growth can, in turn, cause transition via different routes, again depending on the level of external disturbances, see Fig. 1.1. The current thesis focuses on the effect of free-stream turbulence (vorticity) on the transition rather than excitation through e.g. acoustic waves or surface vibrations. In this context, the amplitude of the forcing disturbances in Fig. 1.1 is equivalent to the free-stream turbulence level.

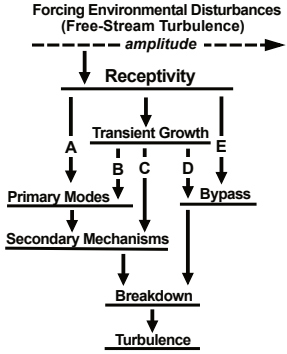

Figure 1.1.: A summary of the different paths from receptivity to boundary layer transition. After Saric *et al.* (2002).

In the case of low turbulence levels and TS-driven transition in 2D boundary

layers, the fluctuations of the free-stream turbulence enter the boundary layer through receptivity (Morkovin, 1969). Regions with high receptivity on NLF airfoils are areas with high surface curvature, rapid boundary layer change or with surface roughness (Saric *et al.*, 2002). The disturbances that enter the boundary layer serve as seeds for TS-modes that undergo a frequency dependent amplification and grow exponentially as they are convected downstream in the boundary layer. In this low range of turbulence levels, variations in Tu change the initial disturbance level, but do not change the stability characteristics of the boundary layer.

At higher turbulence levels, Klebanoff modes, also called streaky structures, appear that are a response to external excitation from the free-stream turbulence (Durbin, 2017). They are linked to significantly larger external length scales than the TS-waves. The receptivity relevant to Klebanoff modes is complex and includes different mechanisms depending on the velocity component of the turbulence, see Schrader *et al.* (2010). The dominant receptivity is with respect to the axial (streamwise) vorticity vector. Vertical vorticity contributes in an indirect way, by being stretched and tilted into more or less axial vortices when encountering the airfoil leading edge. Consequently, the leading edge radius has an influence on the receptivity to the vertical vortices, but not on the receptivity to the axial ones. Klebanoff modes can lead to transition either by locally modifying the stability characteristics of the boundary layer, thereby promoting the growth of TS-modes, or by breakdown without substantial contribution from TS-waves. However, the mechanism of the latter is still not fully clarified (Fransson & Shahinfar, 2020).

As described, the transition in 2D boundary layers tends to be dominated by amplification of TS-modes at low turbulence levels and by the effects of Klebanoff modes at high levels. However, there are no sharp borders between the Tu-regions of the different types of transition. Kendall (1990) used a large amount of wind tunnel measurements to demonstrate how TS-waves are the dominant mechanism of transition for streamwise turbulence levels $0.1\% \leqslant Tu_u \leqslant 0.2\%$. Arnal & Juillen (1978)[1] measured TS-waves at $Tu_u = 0.1\%$ that were barely observable at $Tu_u = 0.3\%$ and bypass transition was observed at $Tu_u = 1.0\%$. Similar results are reported by Suder *et al.* (1988), who measured "classic" or "orderly", TS-driven transition at $Tu_u = 0.3\%$ and bypass transition already at $Tu_u = 0.65\%$. Crouch (2008) refers to experiments by Kosorygin showing that TS-waves are active in the transition process up to $Tu \approx 0.6\%$. In summary, the driving mode of transition in flat plate boundary layers are TS-waves for $Tu \lesssim 0.2\%$ and Klebanoff modes for $Tu \gtrsim 1\%$. In the intermediate range, where the two coexist and interact, there is a gradual shift from TS-waves to Klebanoff modes as the dominating

[1] The work by Arnal & Juillen (1978) is not available in the public domain, but the results are presented and discussed in many other publications, including Kendall (1985, 1998), Matsubara & Alfredsson (2001) and Fransson (2017).

mechanism for transition.

When comparing those integral turbulence levels in wind tunnels to the conditions in flight, it is essential to take the spectral content of the turbulence into account. The energy in the low frequency part of the spectrum tends to be much more dominant in the atmospheric turbulence than in wind tunnel turbulence. A correspondence between wind tunnels and flight for TS-driven transition can be found by matching the spectral energy levels in a frequency range representative for TS-amplification on NLF airfoils on general aviation aircraft and wind turbines, $500 \lesssim f \lesssim 3000$ Hz. Using this method, typical atmospheric turbulence measured in flight (Weismüller, 2012) and at altitudes relevant for wind turbines (Li *et al.*, 2014) corresponds to longitudinal turbulence in the wind tunnel Tu_u (integrated for $10 \leqslant f \leqslant 5000$ Hz), of $Tu_u \lesssim 0.2\%$ and $Tu_u \lesssim 0.5\%$ respectively. The measurements of Weismüller (2012) and Li *et al.* (2014) represent some of the stronger levels of turbulence found in a larger body of literature, and indicate approximate upper limits. The levels for normal operating conditions are typically lower, see e.g. Greiner & Würz (2022). Consequently, flight through the turbulence reported by Weismüller (2012) and Li *et al.* (2014) corresponds to wind tunnel conditions well below the $Tu \approx 1.0\%$ above which Klebanoff modes tend to dominate the transition. Therefore, it can be assumed that the transition on NLF airfoils operating in the convective part of the atmosphere is driven by TS-instabilities. This assumption is supported by several flight measurements, including those of Zanin (1985, 2020), Seitz & Horstmann (2006), Peltzer (2008), Reeh (2014) and Guissart *et al.* (2021).

Several attempts have been made to model the impact of free-stream turbulence in the classic e^n method for transition prediction. The level of the n-factor criterion for transition n_{crit} depends on the disturbance environment as well as the receptivity characteristics of the boundary layer. However, the conventional method of adjusting n_{crit} to fit wind tunnel measurements does not provide a reliable way of translating the results to different disturbance environments, e.g. other test facilities or to flight conditions (Atkin, 2009). As a remedy, methods have been proposed that link n_{crit} to parameters including the free-stream turbulence level, boundary layer receptivity and surface imperfections. These methods are often referred to as variable n-factor methods or linear amplitude correlation methods.

Variable n-factor methods were pioneered by Mack (1977) and van Ingen (1977), who established an empirical correlation between n_{crit} and the free-stream turbulence level using a collection of experiments on flat plates boundary layers. More recent work has focused on the cross-flow instability on swept wings, incorporating the effect on n_{crit} from free-stream turbulence, receptivity and surface imperfections, i.e. roughness and steps, see e.g. Crouch & Ng (2000), Crouch (2008) and Borodulin *et al.* (2014). Still, the method of Mack (1977) seen in Fig. 1.2 appears to be the most commonly applied

model for taking the effect of free-steam turbulence level into account in e^n transition predictions.

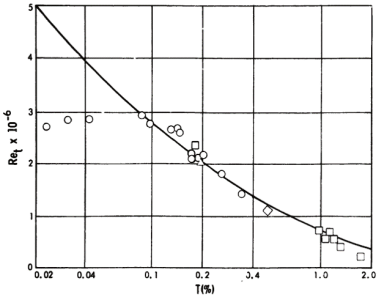

Figure 1.2.: Transition Reynolds number as function of turbulence level. The curve represents the modified e^n method (Mack, 1977). From Mack (1977)[2].

It should be noted that in the range $Tu \lesssim 0.2\%$, the method of Mack (1977) relies on the measurements by Schubauer & Skramstad (1947). In these measurements, the transition location varies with Tu down to $Tu \approx 0.1\%$. Below this level, the measured transition location (expressed as the transition Reynolds number, Re_x), and thereby n_{crit}, is essentially constant, independent of the free-stream turbulence level. This phenomenon is further discussed below.

The very wide range of turbulence scales makes it difficult to access its impact on transition on the theoretical, numerical as well as the experimental side. Therefore, Reeh (2014) proposed a separation of the length scales in the turbulent inflow in "small" and "large" scales, depending on the mechanism by which they affect the boundary layer. The large-scale turbulence acts as variations of the inflow angle, creating unsteady fluctuations of the pressure distribution on the airfoil, to which the boundary layer responds. For the small-scale free-stream turbulence, receptivity (Morkovin, 1969) provides a path into the boundary layer for external disturbances, as well as a wavelength adaptation. Once transformed to eigenmodes in the boundary layer, these disturbances act as seeds for TS-modes that are amplified and lead to transition. Reeh's separation of inflow turbulence according to length scale is adopted in this thesis. However, the proposed separation with respect to turbulent length scales is a significant simplification. It can be argued that by separating the large and small turbulence scales, the interaction between travelling high-frequency TS waves and Klebanoff modes (described by e.g. Fasel (2002)) may not be fully captured. Nevertheless, this approach can be

[2]Work of the US Gov. Public use permitted.

regarded as acceptable for NLF airfoils, for which an underlying assumption is that the transition is dominated by TS-modes.

1.2.3. Small-scale turbulence and transition

The classic experiment on transition in low levels of free-stream turbulence is the one of Schubauer & Skramstad (1947). They conducted measurements in flat plate boundary layers with zero pressure gradient in a range of Tu and presented comparisons with linear stability theory. The base turbulence level of $Tu = 0.27\%$ was gradually reduced to 0.02% by installing additional turbulence damping screens in the settling chamber. In addition, a grid was used to raise the turbulence level to $Tu = 0.34\%$. As already described in the section about variable n-factor methods, the dependency of the transition Reynolds number Re_x, on Tu decreased sharply below $Tu \approx 0.1\%$. The reason is most likely that the transition was dominated by acoustic disturbances below $Tu \approx 0.1\%$, thus masking the influence of the free-stream turbulence (Loehrke *et al.*, 1975). A similar experiment, albeit with lower acoustic disturbance levels, was conducted by Wells (1967). At $Tu \approx 0.3\%$, the results are similar to those of Schubauer & Skramstad (1947) but for lower Tu the measurements of Wells (1967) show a higher transition Reynolds number. At $Tu \approx 0.1\%$, Schubauer & Skramstad (1947) measured $Re_x = 2.8 \cdot 10^6$ and Wells (1967) $Re_x = 4.9 \cdot 10^6$, a difference typically attributed to a lower level of acoustic noise in Wells (1967). However, in both the measurements of Schubauer & Skramstad (1947) and in those of Wells (1967), Re_x levels off at $Tu \approx 0.1\%$, below which it is essentially constant. Up to now, the trend of $Re_x(Tu)$ or $n_{crit}(Tu)$ for $Tu < 0.1\%$ has not been studied in more quiet tunnels.

The progressive change from a flow with quasi-uniform TS waves to one with isolated wave packets was first observed by Kendall (1990) who investigated the range $0.11\% < Tu_u < 0.22\%$. Kendall noted that the wave amplitudes were not linearly related to the Tu and that the packets typically evolved into turbulent spots.

As described above, Klebanoff modes, or streaky structures, tend to dominate the transition process for $Tu \gtrsim 1\%$. However, at lower turbulence levels, TS-waves and Klebanoff modes interact, see e.g. Wu & Choudhari (2001) and Fasel (2002). Consequently, Klebanoff modes are relevant also at the levels of turbulence measured in flight in the convective part of the atmosphere.

The Klebanoff modes, or streaky structures, are attributed to Klebanoff (1971) who described a slowly varying velocity fluctuation in the boundary layer, the "breathing mode". The phenomena was further described by Arnal & Juillen (1978) who observed disturbance growth in the u-direction 2.5 times further away from the wall than the first maximum of the normal TS-eigenfunction. The measured disturbances reached up to several percent of

the free-stream velocity U_∞, before turbulent breakdown, significantly higher than reported for TS-transition. In the measurements of Kendall (1985), streaky structures were observed down to Tu of only 0.16%. An extensive series of investigations on streaky structures has been conducted at the Royal Institute of Technology, KTH, Stockholm, mainly at $Tu > 1.0\%$ and the research is still ongoing. Similar to Arnal & Juillen (1978), Westin *et al.* (1994) reported disturbance levels in the order of 5-10% of U_∞ before breakdown to turbulence occurs. The growth of the longitudinal structures was initially algebraic, but decayed in the streamwise direction unless the initial forcing was stronger than a certain threshold level. The combined measurements and flow visualizations of Matsubara & Alfredsson (2001) provided additional details about the streaky nature of the flow structures of Klebanoff modes, and they found the spanwise scale of the structures to be of the same order as the boundary layer thickness.

Although not the dominating mechanism for transition in the range of turbulence levels measured in the convective part of the atmospheric boundary layer, Klebanoff modes can interact with TS-waves and thus influence the transition process. Most publications agree on the main interaction mechanism, the local and temporal modification of the boundary layer stability, but the details seem less clear.

Kendall (1998) introduced a small vortex in the boundary layer, representing a single Klebanoff-streak, and observed that it limited the spanwise spreading of artificially generated TS wave-packets. Still, the same wave packets exhibited the normal spreading behavior in a boundary layer with Klebanoff modes generated by free-stream turbulence. In experiments with a weaker vortex than Kendall (1998), Watmuff (1997) observed that the distortion of TS-waves by weak streamwise vorticity appeared to be largely linear. The local increase in amplification was found to cause earlier transition. Westin *et al.* (1994) observed that the streaky structures cause a distortion to the mean boundary layer profiles that resembles the effect of an adverse pressure gradient. It should be noted that this differs from Kendall (1998) where a decrease in velocity was observed in the outer region of the boundary layer and an increase in the inner region. In a follow-up paper to Westin *et al.* (1994), Boiko *et al.* (1994) measured lower growth rates of artificially introduced TS-waves at high turbulence level than at low Tu. The lower growth rate was caused by the loss of coherence at high Tu. However, local regions of high amplification resulted in the formation of turbulent spots. Wu & Choudhari (2001) developed a simplified mathematical model that to some degree captures how the Klebanoff modes change the local stability, causing local variations in the growth of the TS-waves. The general mechanism of the interaction between TS-waves and Klebanoff modes was verified by the direct numerical simulations of Fasel (2002). The simulations of Fasel (2002) include the receptivity at the leading edge that transforms vortices in the

free-stream turbulence into the streaky structures of Klebanoff modes.

Measurements of the boundary layer transition at free flight conditions are less common than in wind tunnels. Early boundary layer investigations were conducted by Zanin (e.g. Zanin (1985)) and a summary of the work has been published recently (Zanin, 2020). Wave packets leading to transition were observed in both calm air and in the more turbulent conditions inside clouds. Seitz & Horstmann (2006) used arrays of hot-film sensors to investigate TS-waves in flight, observing stochastically occurring wave packets. In measurements on a glider, Peltzer (2008) recorded 2D TS-waves at the early, linear stage of the transition. Oblique waves were identified further upstream in the flight measurement than in corresponding wind tunnel measurements, an effect attributed to the differences in turbulence characteristics. Experiments with forced disturbances from point sources on the airfoil surface showed that a combination of multiple frequencies was closer to the case with natural transition than single frequency excitation. The influence of atmospheric turbulence on the performance of gliders was investigated by Weismüller (2012) using an extensively instrumented wing-glove mounted on a motorized glider. Weismüller (2012) showed that the unsteady inflow angles induced by the large turbulence scales can cause additional drag, if the airfoil is operated close to the corners of the laminar bucket. The work of Weismüller (2012) was continued by Reeh (2014), who used hot-film sensors to measure the boundary layer development at different levels of atmospheric turbulence. Taking the work of Weismüller (2012) and Reeh (2014) further, Guissart *et al.* (2020, 2021) conducted flight measurements on the pressure side of the same airfoil in a range of turbulence levels. The investigations of Guissart *et al.* (2020, 2021) were coordinated with numerical simulations by Ohno (2023) and the wind tunnel measurements of the current thesis. Comparisons with these flight measurements are found in 5.8.

1.2.4. Oscillating inflow and transition

A large part of the research on airfoils with oscillating inflow- or pitch angle has been focused on separated or transonic flow, see McCroskey (1981). In particular, the dynamic stall phenomenon has received much attention. Carr *et al.* (1977) performed one of the classic experiments on pitching airfoils, investigating the influence of Re, the reduced frequency κ and oscillation amplitude in the presence of a laminar separation bubble. A more current study by Choudhry *et al.* (2014) uses a collective of data from various researchers and breaks down the lift curve into stages that are analyzed separately. Many studies of the boundary layer and transition related to oscillating flow on airfoils have been performed at low Re, where transition takes place in laminar separation bubbles. One example is Lee & Gerontakos (2004), who's experiments covered attached flow, light stall and deep stall on a NACA0012 at

$Re = 1 \cdot 10^5$.

However, the current work focuses on the boundary layer transition on the pressure side of NLF airfoils, at conditions relevant for cruise or dash flight through atmospheric turbulence. For these cases, the laminar boundary layer is attached to the wall, the transition is TS-driven and the amplitudes of the inflow angle oscillations are small (Greiner & Würz, 2021) compared to most investigations of dynamic stall. For this kind of flow, the body of literature is significantly smaller than for dynamic stall.

Early experimental work on boundary layer transition in oscillating flow was performed by Miller & Fejer (1964) and by Obremski & Fejer (1967), conducting hot wire measurements on a flat plate with oscillating free-stream velocity. Miller & Fejer (1964) found turbulent spots forming periodically in contrast to the random occurrence in non-oscillating flows. Obremski & Fejer (1967) investigated cases with zero pressure gradient as well as both favorable and adverse ones. They described the development of turbulent spots in an initial "creative" phase where spots appear and develop rapidly, followed by a later "convective" phase where the spots travel with close to constant leading- and trailing edge velocities. Loehrke *et al.* (1975) points out shortcomings in the experiments of both Miller & Fejer (1964) and of Obremski & Fejer (1967), in particular related to the transition Reynolds number and its dependency on the free-stream turbulence level[3]. Studer *et al.* (2006) performed investigations on a NACA0015 airfoil at oscillating inflow angle and used wavelet transform to extract time dependent frequency spectra. This work allows a detailed comparison of experimental and theoretical amplification rates.

On the numerical side, Obremski & Morkovin (1969) as well as Studer *et al.* (2006) used LST-based methods for transition prediction, in which the integration of the TS amplitudes are performed along the trajectories of the TS-modes, rather than for a single instance in time. A similar approach was used by Reeh (2014) who solved the Orr-Sommerfeld equation locally for a full period of the inflow oscillation and tracked the TS amplification rates for each mode using their phase velocity. The trajectory-following LST method of Ohno *et al.* (2022) was extended with an improved gust model and applied together with DNS to unsteady transition within a laminar separation bubble in Ohno *et al.* (2023). This extended method is used for comparisons in the current thesis. Related DNS investigations can be found in Ohno (2023).

Negi *et al.* (2021) conducted large-eddy simulations to investigate the transition on a NLF airfoil undergoing small amplitude pitch oscillations. Unfortunately, their case includes a small region of turbulent separation close

[3]The shortcomings pointed out by Loehrke *et al.* (1975) may have influenced primarily the level of the transition Reynolds numbers determined in Miller & Fejer (1964) as well as by Obremski & Fejer (1967). In this thesis, the velocity of the transition fronts and the overall phenomenology from Obremski & Fejer (1967) are used for comparisons rather than the transition Reynolds number.

to the trailing edge. In general, trailing edge separations tend to influence the pressure distribution over the entire airfoil, to which the boundary layer responds. Consequently, it is difficult to separate the unsteady behavior of the boundary layer transition and of the flow separation from each other.

1.2.5. Transition in combined small-scale turbulence and oscillating inflow

During flight through the turbulent atmosphere, both small and large turbulence scales are present simultaneously, and interactions seem plausible. Still, little research exists on boundary layer transition under the combined influence of inflow angle variations and free-stream turbulence. In the wind energy community, somewhat related studies have been conducted on how the dynamic stall is influenced by elevated levels of free-stream turbulence. One example is Amandolese & Széchényi (2004) who conducted wind tunnel measurements on a NACA 64_4-421 airfoil oscillating in pitch at $Tu = 1.2\%$, 4.5% and 7.5%. The measurements comprised surface pressure distributions during pitch angle oscillations, with focus on dynamic stall. From the pressure distributions, the integrated lift and drag coefficients were extracted, as well as the location of the turbulent trailing edge separation. However, no information on the boundary layer transition is available.

1.3. Objectives and outline

Aircraft and wind turbines operating in the convective part of the atmosphere encounters turbulent inflow that leads to unsteady pressure distributions and influences the boundary layer transition. The location of the transition has a direct effect on the performance of the NLF airfoils. For gliders, certain types of aircraft are reported to suffer a larger loss of performance in turbulent conditions than others (Weismüller, 2012), indicating that the airfoil shape and pressure distribution has a significant influence on the response to free-stream turbulence.

The majority of literature on the influence of small-scale turbulence on transition in 2D boundary layers is focused on $Tu \gtrsim 0.5\%$, at which the transition is mainly driven by Klebanoff modes rather than by TS-waves. This is in contrast to the levels of turbulence encountered in the convective part of the atmosphere. Within the literature covering $Tu \lesssim 0.5\%$, the classic results used to establish a relationship between turbulence level and transition Reynoldsnumber are questionable for $Tu < 0.1\%$. In addition, none include leading edge geometries or pressure gradients representative for NLF airfoils.

The situation is somewhat similar for available research on the influence of the inflow angle oscillations that represent the effect of large-scale turbulence.

There is a large body of research on dynamic stall, encompassing large amplitudes of inflow angle oscillations at relatively low reduced frequencies. The focus is on flow cases including separated flow, often at low Reynolds numbers at which laminar separation bubbles dominate the transition process. However, boundary layer transition at small amplitudes of inflow oscillations and at Reynolds numbers characteristic for general aviation aircraft or wind turbine application are not addressed. Similar to small-scale turbulence, some relevant work is available for flat plates, but none with leading edge geometries and pressure gradients typical for NLF airfoils. In addition, there is a large gap with respect to transition influenced by the combination of small-scale turbulence and inflow angle oscillations. Without further knowledge in these areas, the design of NLF airfoils for turbulent inflow conditions is associated with large uncertainties.

In order to assess these open questions, detailed investigations of the boundary layer on the pressure side of an non-swept NLF airfoil are conducted at flight Reynolds numbers. The chosen operating point is close to the lower corner of the laminar bucket, representative for cruise or dash flight. The investigation is focused on the following three areas.

First, the response of boundary layer transition to low levels of small-scale free-stream turbulence is examined. Detailed boundary layer measurements are conducted on an NLF airfoil at free-stream turbulence in the range $0.01\% \leqslant Tu_u \leqslant 0.1\%$ in the Laminar Wind Tunnel (LWT) at IAG, Stuttgart University. The range is chosen to adress the Tu-range in which the transition prediction method of Mack (1977) is not fully supported by experimental data. To highlight the influence of the airfoil geometry, and associated base flow, significantly different airfoils are included in the measurements of the transition location. The increased levels of turbulence are generated using a grid in the settling chamber of the wind tunnel.

Second, the influence of inflow angle oscillations, representing large-scale turbulence, on the boundary layer is investigated. The range of inflow angle oscillations cover reduced frequencies $0.06 \leqslant \kappa \leqslant 1.7$ ($0.5 \leqslant f \leqslant 15$ Hz) at an equivalent zero-to-peak amplitude of $\alpha_{inflow} \sim 0.5°$. The inflow angle oscillations are generated using a special gust generator installed upstream of the model. Unsteady surface pressures on the main airfoil are analyzed to gain information about the boundary layer development.

Third, the combined influence of small-scale turbulence and inflow angle oscillations is explored by combining passive grids in the settling chamber of the tunnel with the gust generator.

The wind tunnel investigations are complemented by flight measurements conducted at the Technical University of Darmstadt and numerical simulations performed at the IAG. Together, these different investigations provide a unique dataset for interpreting the transition phenomenon at unsteady inflow condition.

The current thesis is structured as follows. Chapter 2 describes the experimental setup and the data analysis methods employed. The grids for generating the small-scale turbulence and the gust generator producing the inflow angle are depicted in detail. The measurement equipment used for the hot-wire anemometry and the surface pressure measurements are documented, as well as the methods used for calibration and data processing. The chapter describes the analysis methodologies, including the linear stability analysis, model turbulence spectrum and the transition criterion for the unsteady measurements. In Chapter 3, the inflow conditions in terms of both small-scale turbulence and inflow angle oscillations are characterized. Particular attention is given to quantifying the performance of the newly developed passive turbulence grids and the gust generator. The detailed measurements of the free-stream turbulence generated by four different passive grids are reported and discussed in App. B. For the gust generator, both the isolated performance and the steady influence on the transition on the main airfoil are assessed. The base flow of the steady reference case is described in Chapter 4, including the pressure distribution, the mean boundary layer parameters and the disturbance development in the boundary layer. The steady reference case depicted in Chapter 4 serves as baseline for the measurements with unsteady inflow in Chapters 5, 6 and 7. The influence of small-scale turbulence on transition is presented and discussed in Chapter 5. A detailed description is given of how increased levels of free-stream turbulence change the structure of the transition process. The presence of both Klebanoff modes and distributed receptivity are shown. The relation between the critical n-factor and the free-stream turbulence level is determined for three different airfoils and compared to the method of Mack (1977). Comparisons are also made to flight measurements performed at TU Darmstadt. Chapter 6 describes the influence of inflow angle oscillations on the transition by analyzing measurements of unsteady surface pressures on the airfoil. The cyclic variations of the surface pressure fluctuations as well as the transition location are analyzed in detail. The temporal development of the amplification rate is discussed and comparisons are made to both unsteady linear stability analysis and to direct numerical simulations. In Chapter 7, the measurements with oscillating inflow angle are conducted at $Tu_u = 0.02\%$, 0.06% and 0.13%, addressing the possible interactions between the two types of unsteady inflow. Finally, Chapter 8 provides brief conclusions of the investigations.

2. Experimental setup and data analysis methods

2.1. Wind tunnel facility

The wind tunnel measurements were conducted in the Laminar Wind Tunnel (LWT) of the Institute of Aerodynamics and Gas Dynamics at the University of Stuttgart (Wortmann & Althaus, 1964). The inlet section employs two filters and four screens (Fig. 2.1) that, combined with an effective contraction ratio of 20, results in an unseparated (Reshotko *et al.*, 1997) longitudinal turbulence level of $Tu_u \leqslant 0.02\%$ over the frequency range of $10 \leqslant f \leqslant 5000$ Hz at a free-stream velocity of $U_\infty = 40$ m/s.

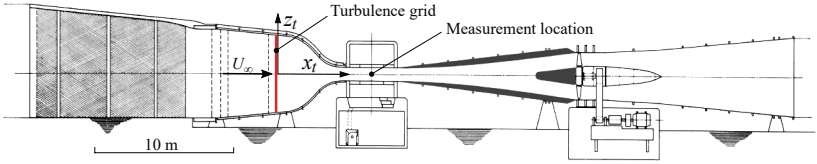

Figure 2.1.: The Laminar Wind Tunnel (LWT) at the University of Stuttgart. The dashed lines in the settling chamber represent turbulence suppressing screens.[1]

The rectangular 0.73×2.73 m^2 test section with a length of 3.15 m is enclosed in a chamber where the static pressure is adjusted to a level slightly below the static pressure in the test section. This prevents air from entering the test section through leakages. The diffuser between the test section and the fan is equipped with sound absorbing lining that reduces the noise level in the test section to 76 dBA at 40 m/s (Plogmann & Würz, 2013). Two-point cross-correlation measurements in the transverse plane using hot-wire probes have shown the dominance of acoustic disturbances for frequencies below 200 Hz. These results are supported by a comparison to measurements with an in-flow microphone. Toward higher frequencies, the energy spectrum rolls off monotonically until it drops below the electronic noise.

[1] Copyright the Institute of Aerodynamics and Gas Dynamics, University of Stuttgart. Used with permission.

The excellent flow quality with respect to the level of vortical and acoustical disturbance ensures that the energy of the background disturbances for frequencies $f \geqslant 100$ Hz is lower than the grid generated turbulence by a factor of eight or more. Consequently, the spectral shape of the grid turbulence is not influenced by the background disturbances of the wind tunnel.

Two-dimensional airfoil models with a span of 0.73 m are mounted vertically between rotating turntables in the floor and ceiling. The gaps between the model and the turntables are carefully sealed. Due to the open return construction of the tunnel, the temperature, humidity, density and viscosity in the test section vary slightly with the atmospheric conditions. In order to keep the variation of the reduced frequency $\kappa = \frac{\pi f c}{U_\infty}$ and the non-dimensional frequency $F = \frac{2\pi f \nu}{U_\infty^2}$ small, the free-stream velocity rather than the Reynolds number was kept constant in the current measurements. The main measurements on the MW-166-39-44-43 airfoil were performed at $U_\infty = 38$ m/s.

2.2. Generation of small-scale turbulence

Active or passive grids can be used to generate nearly isotropic small-scale turbulence in wind tunnels. Early examples are the experiments of Simmons & Salter (1934), whose study includes the flow homogeneity as a function of downstream distance, and the extensive investigations of turbulence characteristics by Batchelor & Townsend (1948). Various aspects of grid turbulence continue to be active research areas, for instance the effects of grid geometry on the turbulence decay characteristics and the influence of the strain induced by a contraction, for example, see e.g. Nagata *et al.* (2017) and Panda *et al.* (2018). An evolution of the classic, passive grid are active grids, where either moving vanes are employed (e.g. Makita (1991), Knebel *et al.* (2011) and the overview in Mydlarski (2017)) or jets of air (e.g. Mathieu & Alcaraz (1965) and Kendall (1990)) are used to provide additional control of the generated turbulence. Vane type active grids allow shaping of the turbulence spectrum and can extend the inertial subrange to lower frequencies compared to passive grids. However, they cannot achieve low enough integral turbulence levels Tu to satisfy the current design requirements (Larssen & Devenport, 2011; Hearst & Lavoie, 2015). Jet type grids give precise control of the turbulence level, but unpublished measurements in the LWT show that the efficiency drops with increasing free-stream velocity. Covering the desired design envelope up to $Tu_u = 0.5\%$ at a free-stream velocity of $U_\infty = 80$ m/s in the LWT with a jet type grid is not feasible. In the current work, an active, jet type grid is used to explore the lower end of the velocity- and Tu-range of interest.

Roach (1987) and Kurian & Fransson (2009) provide excellent overviews of nearly isotropic grid turbulence, both based on a large amount of wind tunnel experiments with a wide variety of grids. Roach (1987) as well as Kurian &

Fransson (2009) analyzed turbulence generated by grids mounted in the test section. To further improve the isotropy of the turbulence, a slight contraction can be introduced downstream of the grid. The contraction induces a strain in the flow that alters the longitudinal and transverse turbulence components differently. Several researches have made use of this effect, including Comte-Bellot & Corrsin (1966) who employed a 1.26:1 contraction to equalize the initial anisotropy of the turbulence.

Uberoi (1956) and Tan-atichat *et al.* (1980) used wind tunnels with interchangeable contractions to make systematic measurements on the streamwise development of the mean flow parameters and the turbulence through the contraction and test section. Uberoi (1956) investigated contractions with ratios of 4:1, 9:1 and 16:1 with square cross-sections. Tan-atichat *et al.* (1980) used axisymmetric contractions ranging from 1:1 to 36:1 and included different length to diameter ratios, contraction contours and six variants of turbulence generating grids. The higher contraction ratios used by Uberoi (1956) and Tan-atichat *et al.* (1980), compared to the one studied by Comte-Bellot & Corrsin (1966), result in a lower level of turbulence in the longitudinal direction than in the transverse direction.

As observed by Uberoi (1956), the related anisotropy tends to slowly decrease once past the contraction. This process is referred to as the return to isotropy and has been studied with the purpose of improving the Reynolds stress modelling of turbulence in numerical simulations by e.g. Sjögren & Johansson (1998), Choi & Lumley (2001) and Ayyalasomayajula & Warhaft (2006). The rate of the return to isotropy is influenced by the characteristics of the turbulence itself, as shown by Nagata *et al.* (2017). The measurements of Nagata *et al.* (2017) include various types of grids, some of which were rectangular and other of the fractal type.

Wind tunnels designed for aeronautical testing at low turbulence level often have short test sections to reduce the thickness of the wall boundary layers and to minimize frictional losses in the tunnel circuit, see Barlow *et al.* (1999). However, the short test section causes problems when using grids to generate additional turbulence. Grid turbulence requires a certain streamwise distance to attain homogenous conditions and the turbulence decays exponentially with the distance from the grid. These characteristics make it difficult to achieve homogenous, isotropic turbulence with small streamwise gradients in an aeronautical wind tunnel, when placing a turbulence grid at the beginning of the test section. Placing the grid further upstream, in the settling chamber (as done by e.g. Kendall 1990), can reduce both streamwise and transverse gradients, but the downsides include the introduction of scale dependent anisotropy, see App. B.

Many of the published measurements on grid turbulence and its influence on the boundary layer transition have been conducted at $Tu \gtrsim 1\%$. Some examples of investigations on grid turbulence are Uberoi (1956), Ayyalaso-

mayajula & Warhaft (2006) as well as Kurian & Fransson (2009). Notable work on the response of laminar boundary layers to free-stream turbulence include Westin *et al.* (1994), Matsubara & Alfredsson (2001) and Brandt *et al.* (2004), all performed at $Tu \gtrsim 1\%$.

However, glider aircraft and wind turbines operate in the lower part of the atmospheric boundary layer, also called the convective layer if unstably stratified. In this layer, the dissipation rate ε of the turbulence is typically $\lesssim 0.02$ to 0.2 m^2/s^3, see Weismüller (2012) and Li *et al.* (2014) respectively. Even though the route to transition becomes more complex with increasing turbulence level (Saric *et al.*, 2002), a 2D base flow and TS-driven transition can be assumed for gliders and wind turbines. For these applications, the TS-amplification tends to occur in the range $500 \lesssim f \lesssim 3000$ Hz, corresponding to a non-dimensional viscous frequency of $40 \cdot 10^{-6} \lesssim F \lesssim 90 \cdot 10^{-6}$. Across this range of frequencies, the spectrum of the turbulence generated in the wind tunnel should be comparable to atmospheric turbulence, and if possible, across an even wider range. By matching the spectral levels in the range of TS-amplification, the typical dissipation rates in the convective atmosphere translates to a longitudinal turbulence level $Tu_u \lesssim 0.2$ to 0.5% ($10 \leqslant f \leqslant 5000$ Hz) in the wind tunnel, for comparable U_∞.

The current investigation employs passive or active turbulence grids placed in the settling chamber of the wind tunnel, the type of grid depending on the desired Tu level. The passive and the active grids are described in Sect. 2.2.1 and 2.2.2 respectively, and the properties of the generated turbulence are examined in Sect. 3.1 and App. B.

2.2.1. Passive grids

In the current work, passive grids are used when higher levels of turbulence are required. The main requirements for the design of the passive grids include the generation of turbulence with a longitudinal turbulence level Tu_u, up to $\approx 0.5\%$ for free-stream velocities $20 \leqslant U_\infty \leqslant 80$. The turbulence level in u-direction is expressed as

$$Tu_u = \frac{1}{U_\infty}\sqrt{\overline{u'^2}} \tag{2.1}$$

and correspondingly in the v and w-directions. The total turbulence level is determined as

$$Tu = \frac{1}{U_\infty}\sqrt{\frac{1}{3}\left(\overline{u'^2} + \overline{v'^2} + \overline{w'^2}\right)} \tag{2.2}$$

In this thesis, the notation Tu_u^s and Tu_u^x is used to distinguish between measurements of the turbulence level of the u-component conducted with a single- and an x-wire probe respectively.

A good mapping of the atmospheric turbulence spectrum is required for $500 \leqslant f \leqslant 3000$ Hz, which covers the frequencies of the amplified TS-modes for the airfoils and operating conditions of interest.

The current work describes an installation of grids in a wind tunnel with a short test section, which is typical for many aeronautical tunnels. The distance between the start of the test section and the center of the turntable with the airfoil model is only 1.8 m, a limitation that has a strong influence on the layout of the grid installation.

The conventional position for a turbulence generating grid is at, or slightly upstream of, the start of the test section. This type of grid installation can provide nearly isotropic turbulence and predictable turbulence characteristics in the test section. However, the short distance between the grid and the airfoil model means the turbulence is still decaying significantly at the position of the model. Using the relations presented by Roach (1987) and Kurian & Fransson (2009), it can be shown that the turbulence generated by a grid at the start of the LWT test section would decay ∼28% along a typical 0.6 m chord airfoil model, a marked departure from the conditions in flight.

An alternative solution is to place the turbulence grid in the settling chamber. The main drawback of this approach is the anisotropy induced by the contraction between the grid and the test section, which is discussed in Sect. 3.1.1 and App. B. However, the current measurements show that the Tu decay in the streamwise direction is significantly reduced. In the current setup, Tu_u changes 8% along the airfoil chord and the change of total Tu is less than 2%. In addition, the pressure loss of a turbulence grid in the settling chamber is practically negligible, as opposed to a grid at the start of the test section. The latter would reduce the maximum attainable Reynolds number in the tunnel by ∼25%, a critical point for investigations of airfoils at high speeds.

The position of the turbulence grid also influences the turbulence spectrum. At the same turbulence level, turbulence generated by coarser grids placed further upstream tend to have spectra with a more pronounced inertial subrange, which is often desirable. Placing the grid in the settling chamber allows for a longer distance to the grid, although with the mentioned anisotropy as side effect (see Sect. 3.1 and App. B).

The pros and cons of the different grid positions need to be assessed with regard to the limitations of each specific wind tunnel facility and the requirements posed by the measurements to be performed. For the present study, grids placed in the settling chamber were chosen, bearing in mind that the resulting turbulence would be anisotropic. Four different grids were designed, each characterized by the diameter of the grid members d and the spacing between the centerlines of the members (mesh width M), see Table 2.1. The design of the grids is based on the experimental data provided by Roach (1987) and Kurian & Fransson (2009) combined with the influence of con-

tractions described by Uberoi (1956), Tan-atichat *et al.* (1980) and Sjögren & Johansson (1998). It should be noted that Roach (1987) uses the grid diameter d in his empirical equation for $Tu(x_t)$, whereas Kurian & Fransson (2009) uses the mesh width M. These approaches work well within the relatively small range of d/M of the two studies. For more general grid geometries, the generated $Tu(x_t)$ depends on both d and M.

The grid position 0.6 m downstream of the last flow-conditioning screen results in a geometric distance between the grid and the measurement location in the test section of 6.7 m, or $22 \leqslant x_t/M \leqslant 161$ depending on the grid. This is large enough to 1) allow homogenous conditions across the test section to be established and 2) significantly reduce gradients along the test airfoils. Different recommended minimum distances for homogenous turbulence are found in the literature, including $x_t/M \leqslant 10$, 20 and 30 in Roach (1987), Batchelor & Townsend (1948) and Jayesh & Warhaft (1991) respectively. As demonstrated later, these recommendations can be misleading because the grid diameter d is an important parameter for the development of the wake behind each grid member.

The choice of the grid type was influenced by practical aspects, including weight, availability and ease of installation. For the lowest levels of turbulence, a safety-net with $d = 5.8$ mm (rounded to 6 mm hereafter) and $M = 42$ mm in both horizontal and vertical direction is used. The cross section of the net material is close to square with a multitude of "bumps", resulting from its braided structure. The three coarser grids consist of plain rods with a diameter of $d = 16$, 32 and 50 mm respectively. Based on preliminary measurements, only vertical rods were selected for the three coarser grids. Horizontal rods were not added because the mixing turned out to be adequate, with the flow being homogeneous in a plane perpendicular to the free-stream. The members of both the net and the coarser grids are hereafter referred to as "rods". All four grids have a porosity β close to 0.8, which is higher than for the grids used by Roach (1987) ($0.11 \leqslant \beta \leqslant 0.75$) and Kurian & Fransson (2009) ($0.56 \leqslant \beta \leqslant 0.64$). The porosity of grids with rods in one direction is defined as

$$\beta = 1 - \frac{d}{M} \tag{2.3}$$

and for grids with rods in two directions (here, the $d6M42$ net)

$$\beta = \left(1 - \frac{d}{M}\right)^2 \tag{2.4}$$

The contraction ratios from the grid position to the test section are 2.4:1 and 6.1:1 in v (horizontal, y-direction) and w (vertical, z-direction) direction respectively, resulting in 14.7:1 based on the tunnel cross section area.

Grid designation	Diameter d [mm]	Mesh width M [mm]	Type	Porosity β [-]	Distance x_t/M [-]
$d6M42$	5.8	42	Net	0.740	161
$d16M100$	16	100	Vert. rods	0.840	67
$d32M200$	32	200	Vert. rods	0.840	33
$d50M300$	50	300	Vert. rods	0.833	22

Table 2.1.: Grid configurations.

Grid designation	$Re_{\Lambda u}$	$Re_{\Lambda v,w}$	$Re_{\lambda u}$	$Re_{\lambda v,w}$
$d6M42$	38-64	189-1245	25-45	136-422
$d16M100$	38-102	323-2208	29-72	183-470
$d32M200$	61-179	640-4568	44-116	211-442
$d50M300$	103-272	1316-7468	65-150	229-512

Table 2.2.: Grid operating conditions.

2.2.2. Active grid

An active, pneumatic grid was used in the lower range of turbulence levels, $0.03\% \leqslant Tu_u^s \leqslant 0.11\%$. The design is based on the grid described by Kendall (1990) and uses a multitude of tiny jets of air blowing against the free-stream to produce the desired turbulence. The grid is placed in the settling chamber of the wind tunnel, at the same position as the passive grids (Fig. 2.2). It consists of horizontal tubes with a diameter of 2 mm in which nozzles in the form of 0.2 mm diameter holes are drilled. The vertical spacing between the tubes, as well as the spacing of the nozzles along the tubes, is 50 mm. The tubes form a 2 × 2 m grid, where vertical metal wires with 0.1 mm diameter at three spanwise locations maintain the vertical spacing between the tubes. Compressed air is supplied through feeder pipes on each side of the grid, each with its own precision pressure regulator. The intensity of the resulting turbulence can be varied by changing the supply pressure to the grid. At a test section velocity U_∞ of 38 m/s, the active grid can generate $0.03\% \leqslant Tu_u^s \leqslant 0.11\%$. More information about the active grid can be found in Ritter (2016).

2.3. Generation of large-scale turbulence

Flight through large-scale turbulence results in unsteady variations of inflow angle in pitch as well as yaw. In the current work, the primary influence of large-scale turbulence are considered to be the unsteady variations of the

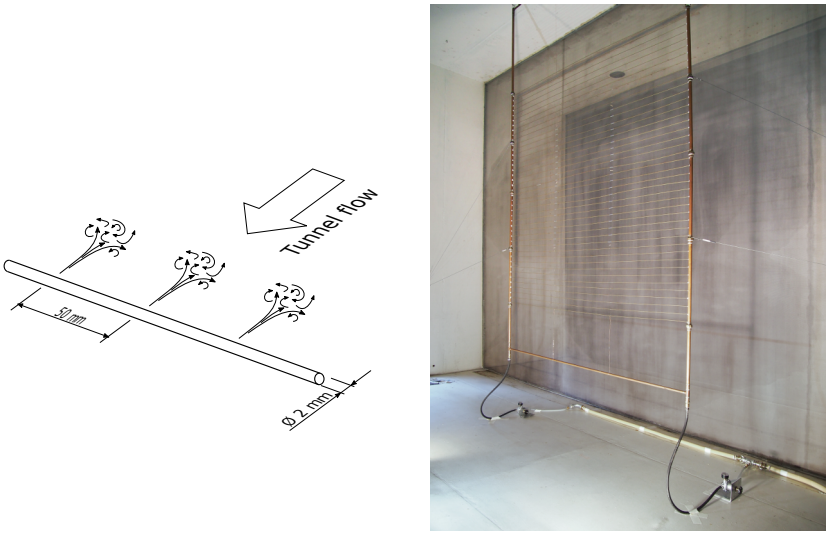

(a) Principle of operation.

(b) Installation in the settling chamber.

Figure 2.2.: The active turbulence grid. Note flow from right to left in both images.

pressure distribution of the airfoil. Only 2D variations of the inflow angle in the pitch-plane are investigated, because the effects on the pressure distribution resulting from inflow angle variations in the yaw-plane are regarded as small.

Established methods for studying the effect of 2D inflow angle fluctuations (gusts) in wind tunnels include oscillating the pitch angle of the test object, translating it in heave (Carta, 1979), as well as by varying the inflow angle. However, the flow situations resulting from the three different approaches are not identical (Leung *et al.* 2018, Zhu & Wang 2018) and varying the inflow angle is the closest equivalent to flight through turbulent air. Two of the more common ways of varying the inflow angle are by additional airfoils (e.g. Wilder & Telionis 1998 and Lancelot *et al.* 2017) or rotating vanes downstream of the model, e.g. Studer *et al.* (2006).

The solution chosen for the present work is depicted in Fig. 2.3 and 2.4. The inflow angle of the main airfoil is changed by an additional airfoil, which induces an up- or downflow depending on its angle of attack, α_{gen}. The additional airfoil is referred to as the gust generator. Using a gust generator instead of oscillating the main airfoil in pitch greatly simplifies the internal instrumentation of the main airfoil and eliminates any secondary influence from accelerations on the pressure measurement.

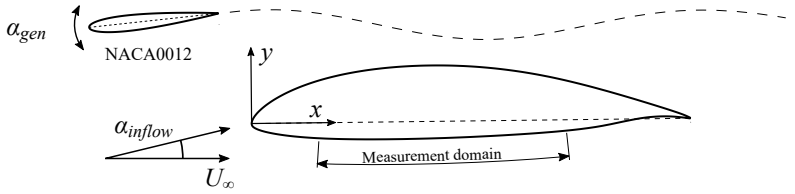

Figure 2.3.: Gust generator arrangement.

The gust generator airfoil is a very light weight 0.4 m chord NACA0012 spanning the test section height. Its leading edge is offset from the main airfoil leading edge by -0.5 m and 0.3 m in x and y-direction respectively. The gust generator airfoil pivots around an axle at $x/c_{gen} = 0.4$ and is driven by a Stöber 1.2 kW AC servo motor series ED401 with a series P 12:1 planetary gearbox. A MC6D21ST motion controller drives the motor via a SD6A16 motor controller, both supplied by Stöber. The geometric gust generator angle α_{gen} is positive for rotations moving its leading edge in positive y-direction (up in Fig. 2.3). The current investigation uses quasi-sinusoidal α_{gen} trajectories and a trigger signal is sent to the data acquisition card at the beginning of each period (cycle time T). The measurements were conducted at frequencies $0.5 \leqslant f \leqslant 15$ Hz, which corresponds to reduced frequency

$\kappa = \frac{\pi f c}{U_\infty} \approx 0.06$ to 1.7, based on the main airfoil chord. The effective zero-to-peak amplitude of the inflow angle oscillations is $\sim 0.5°$, as deduced from the movement of the transition location.

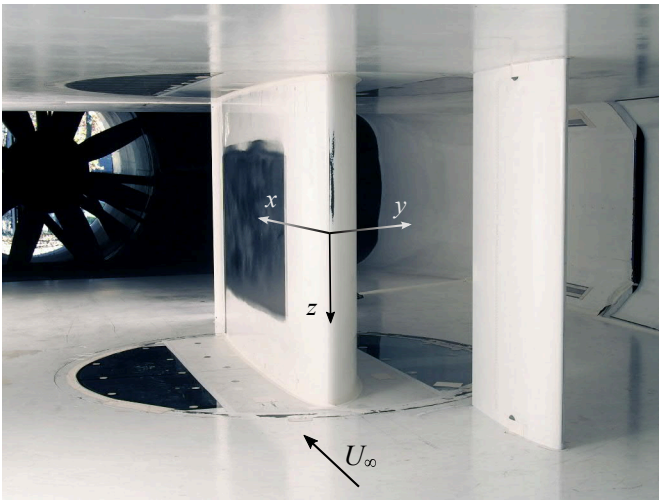

Figure 2.4.: Installation in test section seen from the test section inlet. From right to left; gust generator, main airfoil and wind tunnel fan. Flow from right to left.

2.4. Wind tunnel models

The main part of the investigations was conducted on the MW-166-39-44-43 airfoil. This 16.6% thick airfoil is a significantly modified DU84-158, which in turn is used on the ASW24 glider. The performance of the ASW24 is reported to suffer in turbulent conditions, as described by Weismüller (2012). The airfoil modifications were introduced by Weismüller (2012) for flight measurement using a wing glove. The resulting airfoil matches the lift force of the original wing of the test aircraft at $c_l = 0.75$ and provides flow conditions on the pressure side that approximates a flat plate, see Weismüller (2012).

The 1.35 m chord wind tunnel model was built in the same negative molds as the wing-glove used in the flight measurements at TU Darmstadt. This allows direct matching of flow parameters between the wind tunnel and flight, see the introduction to Chap. 4. The surface of the model is polished, resulting in an rms roughness height $\leqslant 1$ μm. The model does not incorporate

hatches for access but the top and bottom shells can be separated from each other, allowing full access to the internal structure and instrumentation.

In order to facilitate detailed boundary layer investigations, the model was equipped with a "universal disturbance source" (Borodulin *et al.* 2002*a*, De Paula *et al.* 2013) at $x/c = 0.15$ on the pressure side. This chordwise location corresponds to the upstream edge of the measurement domain. However, despite positive experience in previous experiments at lower flow speeds (e.g. Würz *et al.* 2012*b*), the slit of the disturbance source had a significant influence on the boundary layer transition, even when the disturbance source was not in operation. Hence, the slit of the disturbance source was covered with a 40-50 μm thick, 12 mm wide adhesive tape during most of the investigations with small-scale turbulence. Later, the slit was permanently closed using an elastic filler sanded flush with the model surface, and remained in this condition throughout the measurements with IR thermography and subsequent investigations using the gust generator.

A turbulator consisting of a 0.4 mm high 60° zigzag tape placed at $x/c = 0.35$ on the suction side of the airfoil was used throughout the measurements to eliminate any secondary effects from a laminar separation bubble on the suction side. For the same reasons, a similar turbulator was located at $x/c = 0.75$ on the pressure side, just upstream of the main pressure recovery region.

The investigation of the effect of small-scale turbulence on the critical n-factor (Sect. 5.7) included two additional models with the XIS40mod and the NACA64$_3$-418 airfoils, see Würz (1995) and Abbott *et al.* (1945) respectively. Both these models have a chord of 0.6 m. The NACA64$_3$-418 model is equipped with a flap at 70% chord that was fixed at 0° deflection throughout the measurement. The NACA64$_3$-418 airfoil is hereafter referred to as the NACA64-418.

2.5. Measurement techniques

The measurement techniques employed in the current work include flow velocity, surface pressures and surface temperature. Hot-wire anemometry is used to characterize both the free-stream turbulence and the boundary layer on the airfoil model. Steady surface pressures provide information about the base flow, while unsteady surface pressures are used to analyze the transition process. Infrared thermography is employed to detect the location of the boundary layer transition.

2.5.1. Hot-wire anemometry

Constant temperature hot-wire anemometry (CTA) was used both for detailed measurements of the free-stream turbulence and for boundary layer

investigations. Although the fundamental principle is the same, the experimental setup is somewhat different in the two types of measurement.

Measurement equipment

Several measurement campaigns were performed to characterize the free-stream turbulence in the test section. Both a straight, single wire probe (Dantec P11) and an x-wire probe (Dantec P61) were used. The probes are equipped with 2.5 μm diameter wires with a length of 1.0 mm and 1.4 mm for the single wire probe and the x-wire probe respectively. The x-wire probe was rotated between horizontal and vertical orientation to measure all three velocity components. A steel sting with staggered diameters and a length of 0.54 m decouples the probe support from downstream influences. For traverses in the y-direction, the sting was mounted to the standard traversing system of the tunnel, allowing computer controlled positioning (accuracy $\leqslant 0.5$ mm) in a plane perpendicular to the free-stream, 1.8 m downstream the entrance of the test section. The measurements performed at different streamwise positions along the centerline of the tunnel employed a probe holder mounted to the tunnel floor. Great care was taken to streamline all supports in order to avoid any flow separation that can lead to probe vibrations.

Two DISA 55M10 CTA hot-wire bridges were used and the signals were split in an AC and a DC part. Each of the two identical signal chains for the AC part included an Analog Modules Inc. 321A-3-50-NI amplifier with a gain of 300 or 100 depending on the signal level. Prior to amplification, the signals were AC-coupled with a corner frequency of 100 Hz by the internal high pass filter of the 321A-3-50-NI amplifier. First order 16 kHz RC low pass filters provided an initial anti-aliasing and the signals were acquired with a 24 bit RME Hammerfall Multiface II AD-converter sampling all channels simultaneously at 44.1 kHz. The $\Sigma\Delta$ principle of this converter provides excellent aliasing suppression above the corresponding Nyquist frequency. A total of 180 seconds of continuous data were recorded at each measurement point.

The DC parts of the hot-wire signals were low pass filtered at 10 Hz and acquired with an 18 bit National Instruments USB-6289 AD-converter. The same AD-converter was used to measure the position of the probe traverse and the dynamic pressure in the test section, the former was low pass filtered at 1 Hz and the latter at 10 Hz.

The boundary layer measurements were performed using a boundary layer probe (Dantec P15) with a 1.2 mm long, 5 μm diameter wire. The probe was positioned by a traversing system with a resolution of 5 μm in wall normal direction (Würz, 1995). The setup is depicted in Fig. 2.5. Similar to the measurements on free-stream turbulence, a DISA 55M10 bridge was used and the signal was separated in an AC and a DC part and. The AC

part was high pass filtered at 50 Hz and amplified by an AMI 351A-1-50-NC amplifier. Depending on the signal level, a gain of 1, 12 or 120 was used. After anti-aliasing filtering with a first order low pass RC filter with a corner frequency of 6 kHz, the signal was acquired by a 16 bit National Instruments USB-6255 AD-converter sampling at 15625 Hz. The input range of the AD-converter was automatically matched to the signal level for each measurement point. The measured boundary layer profiles typically include 45 points in wall normal direction each at which 2^{16} samples of the AC signal were taken.

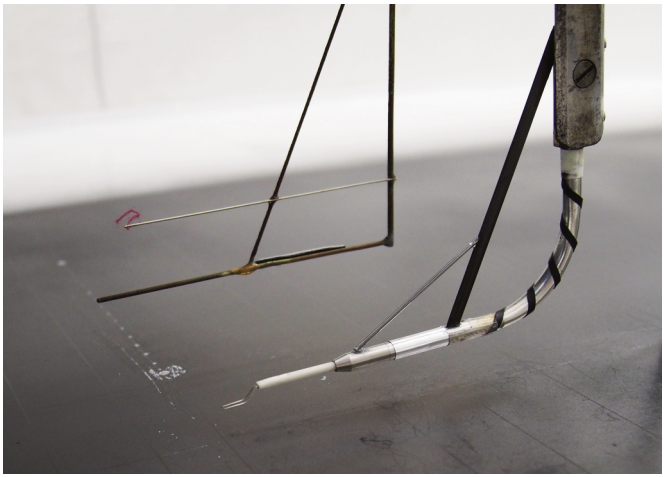

Figure 2.5.: Setup for boundary layer hot-wire measurements. Upper left, the static pressure probe (with tuft probe) and lower right, the hot-wire probe. To the left the spanwise row of pressure taps can be seen.

The same aliasing filter, AD-converter and sample rate were used for the DC part of the signal. The DC signal was not amplified and a fixed input level range was used for the AD-converter.

To reduce the mechanical vibrations of the boundary layer hot-wire probe, the traverse employs a support strut resting on the airfoil surface 100 mm downstream of the probe position. The zero-position of the hot-wire probe in wall-normal direction was obtained with the help of an electrically conductive paint on the model surface. The probe was moved toward the model surface until electrical contact between the probe and model was detected. The probe was then slowly moved away from the surface and measurements begun at the point where no more contact between probe and model was detected. This procedure has proven highly repeatable and removes any inaccuracies linked to probe bending or mechanical backlash. In the streamwise direction the

probe was positioned manually using markings on the model as guide.

The aerodynamic influence of the hot-wire traverse caused a small change to the global flow around the airfoil. This influence was compensated by adding a $0.01 \cdot c$ high, triangular Gurney flap on the suction side of the airfoil when the hot-wire traverer was present in the tunnel.

2.5.2. Hot-wire probe calibration

The hot-wire probes were calibrated according to King's law (King 1914, Bruun 1995)

$$E^2 = A + B \cdot u^n \tag{2.5}$$

where E is the bridge voltage and A, B and n are calibration constants determined by least square fitting to measured calibration points.

The overheat ratio b was adjusted to $b = 1.8$ at the start of each series of measurement. During the boundary layer measurements, the overheat ration was readjusted if the temperature in the test section changed more than 1° C. During the free-stream turbulence measurements, a compensation for the variation in temperature within each series of measurements is performed using the expression from Kanevče & Oka (1973)

$$E_n^2 = E^2 \cdot \left(\frac{T_w - T_n}{T_w - T} \right) \tag{2.6}$$

where E_n and T_n are the bridge voltage and air temperature when the overheat ratio was set, T_w is the wire temperature and T is the air temperature during the measurement. The temperature difference $T_w - T_n$ can be expressed as

$$T_w - T_n = \frac{b-1}{\alpha_{20}} \tag{2.7}$$

in which the temperature coefficient of the Wolfram wire $\alpha_{20} = 0.0036\ \Omega/K$.

Typical temperature drift across a complete sweep of U_∞ or y-position in the free-stream turbulence measurements was 1.9 °C, corresponding to a 3% correction of rms(u). The cut-off frequency of the hot-wire system was determined by a standard square wave test and found to be ∼150 kHz. The x-wire probe was calibrated with respect to the inflow angle in a separate calibration tunnel. The analysis of the x-wire signals follows the effective velocity method of Bradshaw (1971), employing the more detailed description of Bruun (1995). The procedure was modified to allow the probe to be aligned with the flow during the velocity calibration, rather than aligning each wire perpendicular to the flow during its respective calibration.

2.5.3. Hot-wire signal processing

The AC part of each hot-wire signal is corrected for the frequency characteristics of the amplifier high-pass filter and the subsequent anti-aliasing filter. In addition, for the free-stream turbulence measurements, the frequency characteristics of the AC coupling of the AD-converter is taken into account. A compensation is made for the frequency dependent impact of the 10 Ω output impedance of the hot-wire bridge and the 50 Ω input impedance of the internal RC high-pass filter at the input line of the amplifier.

Different schemes have been proposed to correct the measured turbulence spectrum for the loss of spatial resolution of the hot-wire at very small turbulence length scales (McKeon *et al.*, 2007), e.g. the method of Wyngaard (1968), which was extended by Zhu & Antonia (1996). Here, the original Wyngaard (1968) method is employed to correct the measured data. Typical levels of correction in the current measurements are 0.3% on Tu and 5% on the dissipation rate. The integral, Taylor and Kolmogorov length scales are typically corrected by 0.9%, 1.7% and 1.5% respectively.

At the high-frequency end of the turbulence spectrum, the measurements are limited by the electronic noise of the CTA bridges, which increases as f^2, see Freymuth & Fingerson (1997). However, grids $d32M200$ at $U_\infty \geqslant 75$ m/s and $d50M300$ at $U_\infty \geqslant 70$ m/s form exceptions as their spectra are limited by the Nyquist frequency. This may influence the accuracy of the calculated dissipation rate and characteristic length scales. Consequently, the listed cases are excluded from the discussion in the corresponding sections. In the part of the spectrum where the turbulence signal is below the electronic noise floor, a low pass filter is applied in the frequency domain. The necessary cut-off frequency of the filter is individually determined for each spectrum. The range of the Kolmogorov frequency $f_\eta = U_\infty/(2\pi\eta)$ in the measurements is 340 Hz $\leqslant f_\eta \leqslant$ 45 kHz. The highest f_η is approximately twice the cut-off frequency indicated by the electronic noise floor. The high ratio of f_η to the cut-off frequency means that the dissipative subrange is not optimally resolved, due to electronic noise. This is particularly the case for the coarser grids at high U_∞.

2.5.4. Surface pressures

Both steady and unsteady surface pressures on the airfoil surface were measured using pressure taps of 0.4 mm diameter placed in two groups, one row in streamwise direction and one row in spanwise direction. The 42 taps of the streamwise row start at $x/c = 0.011$ on the suction side of the airfoil, continues around the leading edge and end at $x/c = 0.727$ on the pressure side. Upstream $x/c = 0.050$, the line of the taps is offset by 20° in the spanwise direction to reduce any disturbances from one tap to the next. The spanwise

row of pressure taps is located at $x/c = 0.311$ on the pressure side of the airfoil.

Measurement equipment

For the investigations in Chap. 4 and 5, every second tap in the streamwise row was equipped with a SensorTechnics HCL0050 pressure sensor for measuring unsteady pressures. During the measurement with gust generator in Chap. 6 and 7, the HCL sensors were redistributed to cover each pressure tap from $x/c = 0.166$ to $x/c = 0.727$ on the pressure side.

The spanwise row consists of 14 pressure taps with HCL sensors. In addition, two flush mounted Kulite XCQ-062 sensor are included, one at the beginning and one at the end of the row. The spanwise spacing is 7.0 mm, which allows resolving spanwise wavenumbers up to $k_z = 449\ \mathrm{m}^{-1}$, according to the Nyquist-Shannon theorem.

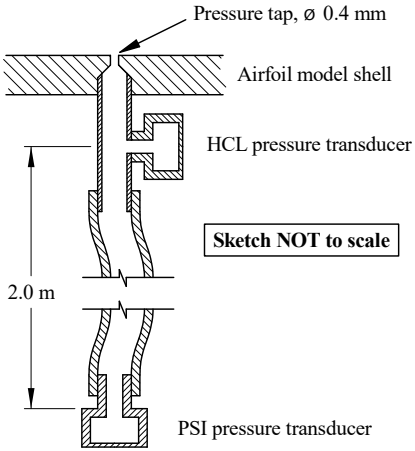

Figure 2.6.: The infinite line sensor installation for measurements of both steady and unsteady surface pressures.

The HCL sensors were modified to reduce the internal dead volume and are connected according to the "infinite line" principle (Samuelson, 1967), see Fig. 2.6. The standing waves associated with a conventional pressure sensor installation are reduced by connecting the pressure tap to a long, thin tube where reflections are attenuated by viscous damping. The pressure sensor is connected as a side branch on the main, "infinite" line. In the current implementation, this "infinite" line is connected to the PSI pressure scanner (ESP64HD, 50 hPa full scale), a connection that serves as the damping tube,

while also enabling simultaneous measurements of both steady and unsteady pressures.

Low noise Cosytec BRVST2 bridge amplifiers were used for conditioning the signals from the HCL and Kulite sensors. The output signal from each sensor is split into separate AC and DC paths. The AC path is high-pass filtered with corner frequency 150 Hz and amplified with a gain of 60 dB. The DC path is low-pass filtered at 1000 Hz and has a gain of 40 dB. The outputs were low-pass filtered by a first order RC filter at 6 kHz and sampled at 15625 Hz by a NI USB 6255 AD-converter. Records of 300 seconds length were captured to provide sufficient data for block- and cycle averaging.

2.5.5. Pressure calibration and signal processing

The steady sensitivity of the HCL sensors was calibrated against the MKS Baratron 120AD reference pressure transducers of the tunnel.

The frequency characteristics of the "infinite line" installation was determined using the spanwise row of pressure sensors. The boundary layer was tripped upstream the sensors, which generates a broadband pressure excitation. The two surface mount Kulite sensors with linear frequency response $\geqslant$ 100 kHz are used as reference sensors and a transfer function is determined from the spectra calculated for each sensor in the spanwise row

$$T_{inf.line}(f) = \frac{\overline{p_{Kulite}(f)}}{\overline{p_{HCL}(f)}} \tag{2.8}$$

In the range $f < 2500$ Hz, the Fourier coefficients of p_{HCL} exhibit a mean standard deviation $< 4\%$ across the sensors in the spanwise row. For the current measurements, this variation is regarded small enough to apply the same transfer function to all HCL sensors in the model. The measured transfer function is shown in Fig. 2.7, compared with a simulation using the model of Nyland (1971). The general tendency of the measured transfer function is captured rather well by the model, despite the strong simplifications of the geometric description.

The measured voltage time series are corrected for the frequency dependent influence of the electronic low- and high-pass filters as well as for the "infinite line" pressure sensor installation, by performing a Fast Fourier Transform (FFT) on the complete time signals. Then the corresponding filter attenuation, gain and pressure tap transfer function ($T_{inf.line}$) is taken into account, after which an inverse FFT reconstructs the corrected time signals. To reduce the impact of electrical disturbances in the measurements with oscillating inflow, the unsteady pressure signals for these cases are not corrected for the influence of the electronic low- and high-pass filters.

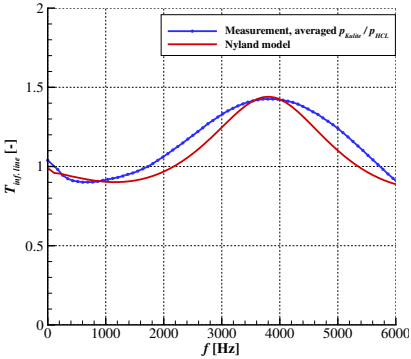

Figure 2.7.: Measured transfer function $T_{inf.line}$ for the pressure sensor installation compared to the Nyland model.

2.5.6. Infrared thermography

According to the Reynolds analogy, the heat transfer between the air and the model surface is related to the skin friction. This allows detection of the boundary layer state by means of infrared thermography, see Quast (2006) and Kowalewski *et al.* (2007). A small temperature difference in the order of 2-3 °K between the air and the model is sufficient to provide the initial condition.

In the current investigations, a FLIR X6540sc infrared (IR) thermography camera has been employed for transition detection on preheated airfoil models. Fig. 2.8a shows a typical thermography image. The maximum gradient of the airfoil surface temperature is used as transition criteria (Joseph *et al.*, 2014; Ikami *et al.*, 2021), a method which has proven robust enough for automated post processing of the IR images (Fig. 2.8b). The temperature readings from the camera were acquired as AD-converter bits. Since no calibration from AD-bits to temperture was available, no scale is shown on the y-axis in Fig. 2.8b. This method detects a rather late stage in the transition process, which results in higher values of n_{crit} compared to other methods, for example the M-TERA intermittency method described in Chap. 2.6.4.

2.6. Data analysis methods

2.6.1. Linear stability theory

At low levels of inflow turbulence, the linear stage of the transition from laminar to turbulent of a 2D boundary layer is driven by the growth of small ampli-

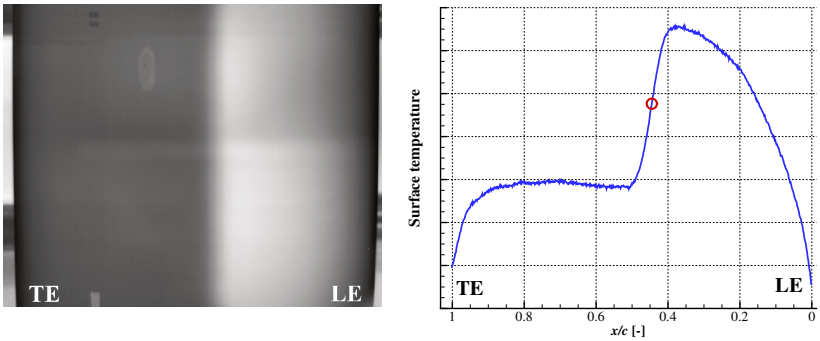

(a) The image from the IR camera.

(b) The surface temperature as function of x/c. The red circle indicates the maximum gradient, where transition is detected.

Figure 2.8.: An example of how infrared thermography is used for transition detection. Note that flow is from right to left. The leading edge is marked with LE and the trailing edge with TE.

tude, wave-like disturbances in the boundary layer, the Tollmien-Schlichting (TS) modes. Tollmien (1928) and Schlichting (1933) were the first to solve the Orr-Sommerfeld equation that is the basis for the linear stability theory (LST). It provides a mathematical description of the spatial and temporal development of TS-waves, see also Mack (1984) as well as Schlichting & Gersten (2016). The classic LST formulation assumes a steady, incompressible, parallel two-dimensional base flow where the velocity u is perturbed by u'. The perturbation can be written as a complex amplitude function, describing the shape of the perturbation in the wall normal direction

$$u'(x, y, z, t) = \hat{u}(y)e^{i(\alpha x+\beta z-\omega t)} \tag{2.9}$$

where x, y and z are coordinated in streamwise, wall normal and spanwise directions respectively, and t denotes time. The complex wavenumbers in streamwise and spanwise direction are expressed as $\alpha = \alpha_r + i \cdot \alpha_i$ and $\beta = \beta_r + i \cdot \beta_i$ respectively. The complex angular frequency is defined as $\omega = \omega_r + i \cdot \omega_i$. Substituting this wave formulation into the Navier-Stokes equations and linearizing the equations about the mean velocity $\bar{u}$ turns the linear stability problem into an eigenvalue problem with eigenvector $\hat{u}$. Based on the assumptions above, the problem can be rewritten into the well-known Orr-Sommerfeld equation, which describes the development of the Tollmien-Schlichting waves. If real-valued wave numbers α are used and ω is complex,

the amplitude will change in time and the analysis is performed in a temporal frame. In the spatial formulation, α is complex and ω is a real-valued parameter, $\omega = 2\pi f$. This causes the amplitude of the disturbance to vary with a local growth rate α_i in x-direction. Disturbances with $\alpha_i > 0$ are damped while $\alpha_i < 0$ means amplification. For $\alpha_i = 0$ the amplitude remains constant.

In the work presented here, only spatial stability analysis for 2D flow is used. For this case, the amplification in terms of amplitude ratio n of a mode with the frequency f can be written as the integral of the amplification rate α_i along the trajectory of the wave, expressed in the surface coordinate s.

$$n(f,s) = \int_{s_0}^{s} -\alpha_i(f,s)ds = ln\left(\frac{A}{A_0}\right) \tag{2.10}$$

The lower bound of the integral, $s_0(f)$ is the first station where $\alpha_i(f) < 0$ and is denoted the primary instability point. The amplitude ratio n represents the amplitude A in relation to an initial amplitude A_0, as shown in 2.10. The maximum amplitude ratio for each location s, across all frequencies, is referred to as the N-factor. This factor, which forms the envelope of the n-factors, is the key parameter in the e^n transition prediction method of Smith & Gamberoni (1956) and van Ingen (1956).

In this thesis, LST analysis is used for comparisons with the experimental results and to deduce various parameters, including the critical n-factor in the experiments. The calculations follow a three-step procedure where:

1. Viscid pressure distributions are calculated with XFOIL V6.96 (Drela, 1989)

2. Highly resolved boundary layer profiles are determined using a finite difference scheme according to Cebeci *et al.* (1974)

3. A shooting method (Conte, 1966) is used to solve the Orr-Sommerfeld equation

Using experimentally obtained pressure distributions in LST analysis is often challenging. The method applied here (see Sect. 4.1 for details) is based on a fit of the calculated pressure distribution to the experimentally obtained pressure gradient and a 2.8% over-speed correction related to the wind tunnel blockage.

2.6.2. Trajectory-following LST

The linear stability analysis described in 2.6.1 is a steady analysis. An extension is required to treat the unsteady inflow angle situations investigated in

Chap. 6 and 7 that lead to an oscillating base flow with time dependent variations of the stability characteristics. Therefore, the growth of a convected mode depends on local amplification rates which vary in time as the mode propagates downstream. Examples of trajectory-following LST methods have been described in the literature, see e.g. Obremski & Morkovin (1969), Studer *et al.* (2006) and Reeh (2014). Here, a trajectory-following LST approach according to Ohno *et al.* (2022) is adopted in combination with an extension to simulate unsteady airfoil boundary layers, see Ohno *et al.* (2023). The method comprises two main steps:

1. The unsteady base flow is determined using two-dimensional, unsteady Reynolds averaged Navier-Stokes simulation (URANS), where the variation of inflow angle is modelled by the disturbance velocity approach (DVA). The DVA approach is described in Heinrich & Reimer (2013). The implementation used in this thesis is covered in detail in Ohno (2023).

2. The time dependent base flow is used as input to the LST analysis. The LST equations used are in principle steady, but the integration of the n-factors is performed along the spatial-temporal trajectories of the TS waves, rather than only in the spatial direction, as in conventional LST.

The combination of URANS and the DVA approach enables the simulation of unsteady variations of the pressure gradients on the airfoil, including the viscous delay of the boundary layer. The DVA approach models the influence of the gust on the flow around the airfoil, but the distortion of the gust by the airfoil itself is neglected. In the present methodology, the location of the neutral stability point, from which the n-factors are integrated, depends on both the TS frequency and the phase of the inflow oscillation. This provides a good representation of a case with natural transition. The trajectory-following LST results shown in this thesis were kindly provided by Duncan Ohno.

2.6.3. Model turbulence spectrum

Model spectra describe the distribution of turbulent energy across a range of frequencies or length scales. Many are based on the break-up of eddies into smaller and smaller scales, the Kolmogorov energy cascade (Kolmogorov, 1941). In the current work, model spectra are used for direct comparison with experimentally obtained spectra as well as to determine the dissipation rate of the turbulence, ε. For the former, the model spectrum of Pope (2000) is employed. This models isotropic turbulence under the assumption of the Kolmogorov hypothesis and equilibrium conditions. Pope expresses the total energy spectrum as

$$E(\kappa) = C\varepsilon^{2/3}\kappa^{-5/3} f_L(\kappa L) f_\eta(\kappa\eta) \tag{2.11}$$

where ε is the dissipation rate, κ is the wavenumber, η is the Kolmogorov length scale and C is a constant = 1.5. L is a length scale characterizing the largest eddies

$$L = \frac{\left(\frac{1}{2}(\bar{u}\cdot\bar{u})\right)^{3/2}}{\varepsilon} \tag{2.12}$$

Flight measurements of atmospheric turbulence indicate an integral length scale $\Lambda \approx 100$ m (Houbolt, 1973), and consequently $L = 100$ m is used in this thesis. The term $f_L(\kappa L)$ describes the shape of the spectrum in the energy containing range and $f_\eta(\kappa\eta)$ determines the shape of the spectrum in the dissipative subrange. Both f_L and f_η are ≈ 1 in the inertial subrange. The two are defined as

$$f_L(\kappa L) = \left(\frac{\kappa L}{[(\kappa L)^2 + c_L]^{1/2}}\right)^{5/3+p_0} \tag{2.13}$$

and

$$f_\eta(\kappa\eta) = e^{-\beta\left\{\left[(\kappa\eta)^4 + c_\eta^4\right]^{1/4} - c_\eta\right\}} \tag{2.14}$$

with $c_L = 6.87$, $p_0 = 2$, $\beta = 5.2$ and $c_\eta = 0.4$

For determining the dissipation rate of the free-stream turbulence, the method of Djenidi & Antonia (2012) is used. For a more detailed description of the method, see App. B.3. This method employs a modified version of the Pope spectrum model, where the constants of the model have been empirically adjusted to $p_0 = 0.5$, $\beta = 7.2$ and $c_\eta = 0.15$. As the energy containing range does not need to be modeled to determine the dissipation rate, the term f_L is set to unity, see Djenidi & Antonia (2012) for further details.

2.6.4. Short time rms and M-TERA transition criteria

In order to capture the temporal development of the unsteady surface pressures in the measurements with periodic inflow angle oscillations, rms values are calculated for a window that is moved along the pressure time series. The width of the window is set to $\pm 10^\circ$ of the inflow oscillation cycle. For each time step, the rms value across the window is calculated.

For transition detection based on the unsteady surface pressures, an implementation of the M-TERA intermittency method of Zhang *et al.* (1996) is adapted. The method is originally developed for fluctuating velocities. Here, the velocities of the original formulation are substitute for the unsteady surface pressure and the mean velocity term $\bar{u}$ is left out.

$$\overline{\left| p' \frac{\partial p'}{\partial t} \right|} \geqslant C_3 \left[\frac{\left(\frac{\partial p'}{\partial t} \right)_{rms}}{\left(p' \frac{\partial p'}{\partial t} \right)_{rms}} \right] \tag{2.15}$$

For the present surface pressure signals, an empirical threshold of $C_3 = 1 \cdot 10^5$ is used. This threshold results in a robust transition detection for the entire range of inflow oscillation frequencies, allowing automated processing of the data. The threshold level is relatively low and results in an earlier detection of transition compared to IR thermography or the stethoscope method.

Both the short time rms values and the C_3 parameter are subsequently cycle-averaged based on the inflow oscillation cycles.

2.6.5. Fast Fourier Transform and Continuous Wavelet Transform

To analyze the measured velocities and pressures in the frequency plane, ensemble-averaged Fast Fourier Transform, FFT is employed (Nobach *et al.*, 2007). The time series are divided into blocks of equal number of samples and frequency spectra are calculated for each block. For each Fourier coefficient, the energy is averaged over the number of blocks. In the free-stream turbulence measurements, blocks of 2^{15} samples are used, typically resulting in 242 blocks per measurement point. For the hot-wire measurements in the boundary layer, 2^{10} samples per block and 64 blocks per point are used for the analysis of eigenvalues and amplification rate. For the spectra of u' as function of wall normal distance, 2^{12} samples per block and 16 blocks per point are used to increase the frequency resolution. The steady surface pressure measurement employs 2^{12} samples per block with typically 1100 blocks per point. No overlap or windowing is used for processing the blocks.

In order to compare the measurement results to LST and to calculate n-factors, the amplitudes of the fluctuating pressures measured at the wall are transformed to velocity fluctuations at the maximum of the wall-normal eigenfunction, u'_{max}. The transformation is based on LST calculations and takes both x/c and frequency into account, see Steiner (2019). In general, the transformation is also a function of the spanwise wavenumber, which is taken into account in the frequency-wavenumber spectra shown in Chap. 4 and 5. The trends of the transformation with both frequency and spanwise wavenumber are similar to those published by Kendall (1990).

The spanwise row of pressure taps is used to calculate frequency-wavenumber spectra. First, each time series is split into blocks as described above. Second, for each block, a FFT is performed in time. In the third step, a FFT is made in space, with each individual sensor position treated as sample, thus providing spectral information in the wave number dimension. The process is repeated for all blocks, and finally the energy for each frequency

and wavenumber is averaged across the blocks.

The FFT analysis is well suited for the steady cases in the current investigations. However, in order to analyze spectral variations over cycles of inflow angle variations, the spectral analysis of a small window in time is needed. The power of the continuous wavelet transform (CWT) for determining time dependent frequency spectra in oscillating flow has been demonstrated by Studer *et al.* (2006) and Reeh (2014). The CWT can be seen as a Fourier transform with an adaptive window, where the width of the window is adapted to the analyzed frequency. The type of wavelet function needs to be matched to the type of signal being analyzed. The wavelet function employed in this work is the Morlet wavelet, as implemented in the function "cwtft" of the MATLAB Wavelet Toolbox V4.15. The Morlet wavelet provides a slightly better resolution in time but a lower resolution in frequency compared to e.g. the Bump wavelet. This results in smoother frequency spectra that are well suited for analysis of peak amplification frequencies and amplification rates. If finer details of the spectrum are of interest, the Bump wavelet could be a better alternative. Unless otherwise noted, the CWT results presented here use the so-called L^2 normalization, by which the wavelet coefficients correspond to an energy spectrum (Farge, 1992). In the current analysis, wavelet coefficients are calculated for each time step of the 300 s long data sets and subsequently cycle-averaged.

3. Characterization of the test conditions

A fundamental part of the current work is the targeted conditioning of the inflow to the airfoil. The level of broadband, small-scale turbulence is increased by introducing turbulence grids, and a gust generator induces inflow angle variations. The following section characterizes the flow conditions in the empty test section with and without the turbulence grids as well as the inflow induced by the gust generator.

3.1. Small-scale turbulence

As described in Sect. 2.2, additional small-scale turbulence is generated in the LWT by the use of grids. Both passive and active grids have been used in the current investigations. The grids are placed in the settling chamber of the wind tunnel, something that has a characteristic influence on the resulting turbulence. The turbulence from the passive grids is described in detail in section 3.1.1 and App. B. The performance of the active grid has been characterized by Ritter (2016) and is briefly discussed in section 3.1.2.

3.1.1. Passive grids

Passive grids offer a simple and reliable tool for generating turbulence in wind tunnels. The grids used in the current work are described in detail in Sect. 2.2.1 and the measurement techniques employed for characterizing the generated turbulence can be found in Sect. 2.5. This section presents a summary of the turbulence characteristics. The detailed characterization can be found in App. B and in Romblad *et al.* (2022*a*).

The spectrum of the turbulence generated by the passive grids corresponds well with the atmospheric turbulence in the frequency range of TS-amplification on NFL airfoils, $500 \lesssim f \lesssim 3000$ Hz, see Fig. 3.1a. The flight measurement data from Guissart *et al.* (2021) and Greiner & Würz (2021) were performed at flight speeds close to 40 m/s. The results have been recalculated to $U_\infty = 40$ m/s from the wavenumber spectra, employing the frozen turbulence assumption of Taylor (1938). Below $f \approx 400$ Hz, the spectra of the turbulence in the wind tunnel show progressively lower energy toward lower frequencies than the spectra measured in flight. One part of the differences in the spectral content is linked to the turbulence generation. The grids do not generate turbulence at the very large length scales seen in the atmosphere

and no further turbulence energy is fed to the flow downstream the grid. Another contributing factor is that the contraction between the grids and the test section attenuates the large scales of the turbulence in the u-direction, introducing an anisotropy to the turbulence. The anisotropy occurs primarily at frequencies lower than the range of TS-amplification. However, care should be taken when extrapolating wind tunnel results to flight conditions, as the effect of the scale dependent anisotropy on the transition on NLF airfoils is not fully clarified.

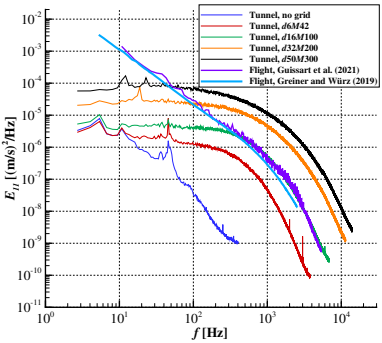

(a) Turbulence spectra in tunnel and flight at $U_\infty = 40$ m/s, u-component. From Romblad *et al.* (2022*a*)[1]

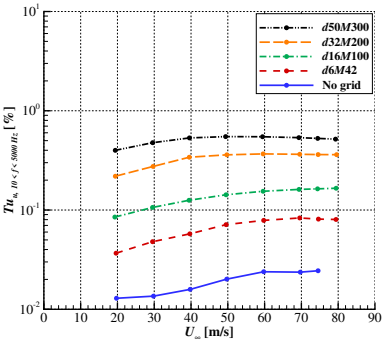

(b) Tu_u^x for the passive grids as function of U_∞. After Romblad *et al.* (2022*a*).

Figure 3.1.: Characteristics of turbulence generated by the passive grids, measured at $x_{ts} = 1.8$ m.

As depicted in Fig. 3.1b, the grids generate longitudinal turbulence levels Tu_u^x covering a range corresponding to the turbulence in the convective part of the atmosphere, see Sect. 2.2. As a result of the grids being located in the settling chamber of the tunnel, the variation of the turbulence level along the test section is small. Tu_u^x change 8% along a typical $c = 0.6$ m chord airfoil and the total Tu changes less than 2%.

3.1.2. Active, pneumatic grid

The characteristics of the turbulence generated by the active grid used in the present measurements was mapped in detail by Ritter (2016). The investigations of Ritter (2016) include turbulence uniformity across the test section as

[1] Used under Creative Commons Attribution 4.0 International License, http://creativecommons.org/licenses/by/4.0/

well as measurements of the turbulence in u, v and w direction at $U_\infty = 20$ m/s. The effect of the contraction on the turbulence is similar to what is seen for the passive grids, including the marked anisotropy in the test section. In the current work, the test conditions utilizing the active grid are verified for the u-component at $U_\infty = 38$ m/s, see Fig. 3.2. The results agree well with Ritter (2016). In general, a higher free-stream velocity requires a significantly higher supply pressure to the grid p_{grid}, to achieve the same Tu. Vice versa, for a given supply pressure, the Tu achieved by pneumatic grids decreases with increasing free-stream velocity, i.e. $Tu \cong 1/U_\infty^n$ with approx. $0.7 \leqslant n \leqslant 1.1$. This characteristic is a strong limitation when using the pneumatic grid in the LWT, where the required free-stream velocity often varies with a factor $\geqslant 4$ from one investigation to another.

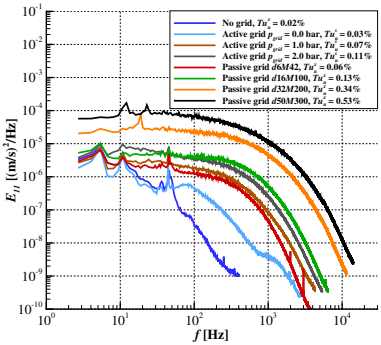

Figure 3.2.: u'-spectra for active and passive grids. Active grid spectra measured at $U_\infty = 38$ m/s with a single-wire probe, passive grid spectra at $U_\infty = 40$ m/s measured with an x-wire probe.

At $p_{grid} = 2.0$ bar, the spectral energy distribution of the u component for the active grid is close to that of the passive grid $d16M100$. The level of the spectrum generated by the active grid is slightly higher than the passive grid in the range $6 < f < 60$ Hz and somewhat lower for $f > 60$ Hz. At $p_{grid} = 1.0$ bar, the spectrum is comparable to that of the $d6M42$ passive grid, with the active grid generating slightly higher energy levels up to $f = 1000$ Hz. For increasing frequencies in the dissipative subrange, above $f = 1000$ Hz, the turbulence energy generated by the active grid does not fall quite as quickly as for the grid $d16M100$. With $p_{grid} = 0.0$ bar, the spectrum is not as smooth as with $p_{grid} > 0.0$ bar and regions with higher energy levels can be seen, centered around $f = 80$ Hz and $f = 1200$ Hz. It is interesting to note that those regions do not correspond to the frequency $f \cong 240$ Hz expected from von Kármán vortex shedding at the $d = 2.0$ mm tubes of the grid.

3.2. Large-scale turbulence

In the current work, the influence of large-scale turbulence on the boundary layer transition is represented by 2D, vertical gusts, as described in Sect. 2.3. The gusts are repeated periodically, resulting in quasi-sinusoidal oscillations of inflow angle. The following sections characterize the performance of the gust generator that is used in the transition investigations.

3.2.1. The isolated gust generator

The first step in the characterization of the gust generator is to determine the performance of the isolated gust generator. Without the main airfoil in the tunnel, the induced flow angle was measured with an x-type hot-wire probe. The probe was placed at the same position as the leading edge of the main airfoil and the gust generator was driven in sinusoidal α_{gen} oscillations.

The induced flow angle measured by the x-wire probe closely follows a sinusoidal, as exemplified by the two cases with $\alpha_{gen} = \pm 6^\circ$ (zero-to-peak amplitude 6°), $f = 9$ Hz and 15 Hz seen in Fig. 3.3. The cycle averaged measurement of the inflow angle at $f = 9$ Hz is almost perfectly sinusoidal and at 15 Hz only slight deviations can be seen after the minimum and maximum of the inflow angle.

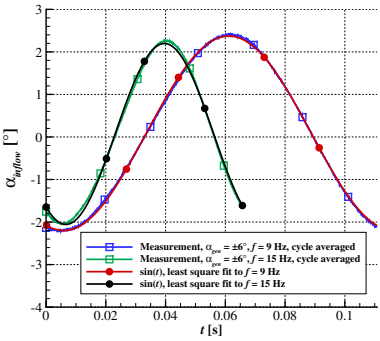

Figure 3.3.: Measured inflow angle time-traces compared to true sinus shapes. $\alpha_{gen} = \pm 6^\circ$, $f = 9$ and 15 Hz. The measurements show cycle averages over 10 seconds. The frequency, amplitude and phase shift of the sinus functions are fitted to the respective measurements using least-squares.

Figure 3.4 shows the zero-to-peak amplitude of the induced flow angle α_{inflow}, for α_{gen} oscillating at amplitudes of ±6°, ±8° and ±10°. For the $\alpha_{gen} = \pm 6^\circ$ case, the amplitude of the induced flow angle increase from 1.8°

at $f = 0.5$ Hz to 2.3° at $f = 6$ Hz, above which it decreases to 2.2° at 15 Hz. The 8° and 10° cases show a similar behavior, with the induced flow angle scaling well with α_{gen}. The reason for the increase of α_{inflow} with increased frequency for $0.5 \leqslant f \leqslant 6$ Hz is not clear. Wester *et al.* (2022) show a similar, but stronger trend for a gust generator consisting of several NACA0009 airfoils. They attribute the increase in induced flow angle with frequency to a reduction of flow separation at higher frequencies (private communication). However, if separation would be the cause in the current measurements, the linear scaling of the behaviour with α_{gen} would not be expected. Theodorsen's theory (Theodorsen, 1935) predicts a reduction of total lift of an airfoil undergoing pitch oscillations for $0 \leqslant \kappa \leqslant 0.2$, above which the lift increases again. However, a reduction in lift should mean a reduction in the induced flow angle, i.e. the opposite trend to the current measurements. Despite an extensive search, no conclusive explanation to the phenomena has been found in the literature.

For reference, the transition investigations with operating gust generator were performed at α_{gen} amplitudes of ±3.5° and ±5.0°.

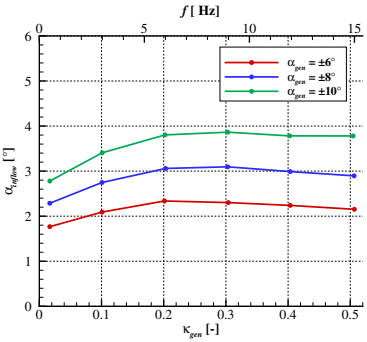

Figure 3.4.: Induced flow angle from the gust generator, zero-to-peak amplitude, $U_\infty = 38$ m/s.

3.2.2. Gust generator with main airfoil, steady conditions

In steady conditions, the inflow angle and the angle of attack of the main airfoil α_{main}, are identical. The steady gust generator should mimic the different α_{main}, i.e. reproduce the steady pressure distribution of the isolated airfoil. Figure 3.5 shows the surface pressure distributions for the steady case with and without gust generator. The three cases plotted correspond to the extremes and the midpoint of the inflow angle cycle, see Fig. 3.6a. The change

in the level of the pressure coefficient c_p, is smaller with the gust generator than with the isolated airfoil, in particular for deflections toward negative α_{gen}. However, the gust generator reproduces the pressures gradients and the transition location of the isolated airfoil very well. The pressure gradients are of prime importance for the development of the boundary layer and the close match seen in Fig. 3.5 is a prerequisite for comparable boundary layer conditions with and without the gust generator.

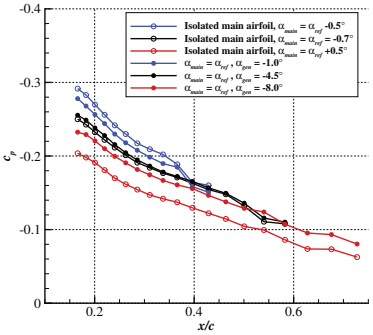

Figure 3.5.: Pressure coefficient distribution of the isolated main airfoil as well as with the gust generator.

The steady influence of α_{gen} on the transition location, x_{tr} closely maps the influence of α_{main} on the isolated main airfoil, as seen in Fig. 3.6. This also holds for different levels of inflow turbulence, which is important for the combined cases of small scale turbulence and inflow angle oscillations treated in Chap. 7. For the same x_{tr}, both the pressure distributions (see Fig. 3.5) and the spectra of the unsteady surface pressures compare well (the spectra are not shown here). This indicates that the small deviations seen at the very extremes of the α_{gen}-range in Fig. 3.6 are linked to a reduction in efficiency of the gust generator rather than differences in the boundary layer on the main airfoil. The α_{main} and α_{gen} used in the current investigation are listed in Table 3.1. These ranges correspond approximately to a zero-to-peak inflow angle amplitude for the isolated airfoil of $\alpha_{inflow} \sim 0.5°$. This matches well with the flight measurements of Greiner & Würz (2021), where the mean amplitude for reduced frequencies of $\kappa = 0.5$, 1.0 and 2.0 were measured at 0.54°, 0.44° and 0.37° respectively. For reference, the current measurements were conducted in the range $0.06 \leqslant \kappa \leqslant 1.67$.

The angles of attack of the isolated main airfoil α_{main} that corresponds to the highest and lowest gust generator angle α_{gen}, are denoted α_{min} and α_{max} respectively. As seen in the 2D stability chart for α_{ref} in Fig. 3.7a, the

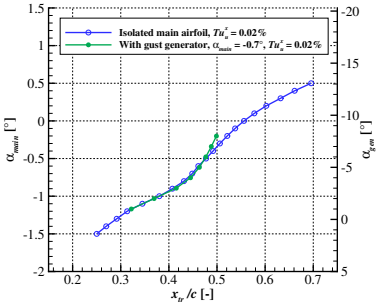

(a) $\alpha_{main} = \alpha_{ref}$, $Tu_u^x = 0.02\%$.

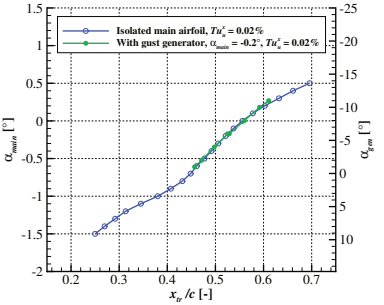

(b) $\alpha_{main} = \alpha_{ref} + 0.5°$, $Tu_u^x = 0.02\%$.

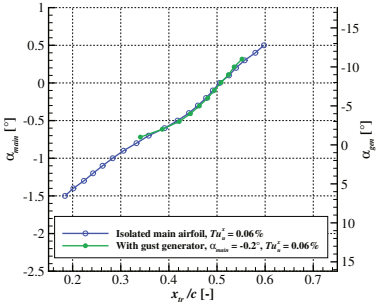

(c) $\alpha_{main} = \alpha_{ref} + 0.5°$, $Tu_u^x = 0.06\%$.

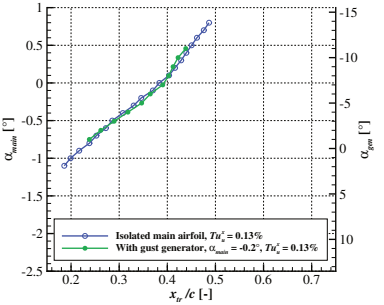

(d) $\alpha_{main} = \alpha_{ref} + 0.5°$, $Tu_u^x = 0.13\%$.

Figure 3.6.: Transition location as function of α_{main} (for isolated main airfoil) and of α_{gen} (with gust generator).

α_{main}	min(α_{gen})	max(α_{gen})	
-0.7° (α_{ref})	-8°	-1°	Chap. 5 and 6
-0.2°	-11°	-1°	Chap. 7

Table 3.1.: Ranges of α_{gen} used for the investigations.

frequencies of the most amplified TS-waves at this angle of attack fall in the range 500 Hz $\lesssim f \lesssim$ 900 Hz. Note that $\alpha_{ref} =$ -1.4° in the flight measurements and the numerical analyses corresponds to -0.7° in the wind tunnel, see the discussion in Sect. 4.1. The steady amplification rates at α_{ref} with and without gust generator are practically identical as seen in Fig. 3.7b. The measured n-factor curves show slightly lower gradients compared to LST. This appears to be an inherent characteristic of n-factors calculated from the measured surface pressures using the method discussed in Sect. 2.6.2. One possible reason is the 3D-nature of the boundary layer disturbances. The surface pressures are a combination of "footprints" from modes with a wide range of propagation angles related to the uncontrolled background disturbance level. In contrast, the present LST is a pure 2D calculation that, according to the Squire theorem, shows the highest amplification rates. This hypothesis is supported by the amplification rates based on the first wall-near maximum of the eigenfunctions from the hot-wire measurements. The hot-wire measurements show a better agreement with the 2D LST (Fig. 4.5), a result of the dominance of 2D modes in the the first wall-near maximum.

The n-factors of the surface pressure measurements in Fig. 3.7b are based on u'_{max} (see 2.6.5 for the transformation) and calculated using values for A_0 that matches the n-factors of the LST at $x/c = 0.429$. The constant level of the most upstream points on the n-factor curves in Fig. 3.7b represents the electronic noise floor of the measurement equipment.

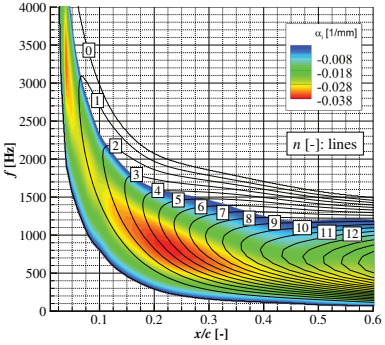

(a) Stability diagram for main airfoil at α_{ref}, after Romblad *et al.* (2022*b*).

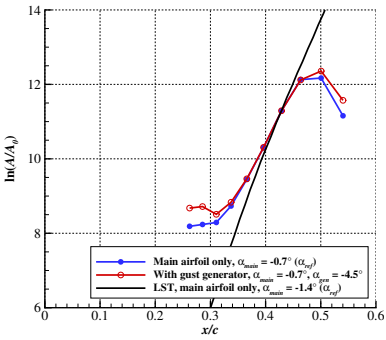

(b) n-factor development with and without gust generator for $567 < f < 626$ Hz, compared with LST at $f = 596$ Hz.

Figure 3.7.: Stability characteristics and amplification rate.

The broadband ($\sim 100 - 5000$ Hz) rms of the unsteady surface pressures

in Fig. 3.8 confirm that the amplification with and without gust generator is very similar. The C_3 parameter of the M-TERA transition detection method shown in Fig. 3.8 closely resembles the rms curves and the level used as transition criteria in the present thesis is indicated. Similar to the n-factor curves in Fig. 3.7b, the most upstream points of the curves in Fig. 3.8 indicate the electronic noise floor of the pressure measuring system.

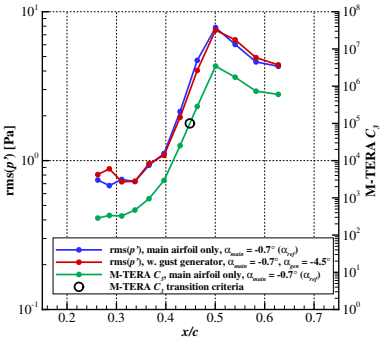

Figure 3.8.: Broadband rms of the unsteady surface pressures without gust generator (blue) and with gust generator (red). The C_3 parameter from the M-TERA transition detection method is plotted in green. After Romblad *et al.* (2020).

In conclusion, the results at steady conditions show that the gust generator provides a fair mapping of the boundary layer of the isolated main airfoil in the range of α_{main} and α_{gen} of the current study.

3.2.3. Gust generator with main airfoil, unsteady conditions

To generate unsteady inflow angle variations, the gust generator airfoil is driven in sinusoidal angle-of-attack oscillations. This induced periodical changes of the inflow angle to the main airfoil, which in turn causes cyclic variations on the pressure distribution.

The amplitude of the surface pressure variations over the gust generator oscillation cycle ($\Delta c_p = c_p(x/c,\alpha_{min}) - c_p(x/c,\alpha_{max})$) increases with increasing frequency. An increase is expected, linked to the frequency-dependent amplitude of the inflow angle oscillations induced by the gust generator (Fig. 3.4). Surprisingly, the measured Δc_p increases more linearly with frequency than the inflow angle. However, the pressure gradient over the part of the airfoil with TS amplification remains essentially constant (standard deviation $<$ 1.5%) in the range of $0.06 \leqslant \kappa \leqslant 1.7$ of the current study. Figure 3.9 shows

the pressure gradient determined as a linear fit to the pressure distribution in the range $0.16 \leqslant x/c \leqslant 0.24$ at α_{min} and α_{max}. With the pressure gradient being primary driver for the boundary layer development, the gust generator setup is considered suitable for the current investigations of the influence of inflow angle oscillations.

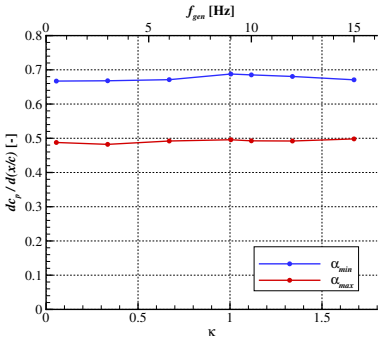

Figure 3.9.: Pressure gradient as function of κ for $\alpha_{main} = \alpha_{ref}$, $Tu_u^x = 0.02\%$.

4. Steady flow baseline, MW-166-39-44-43 airfoil

The main part of the investigations in this thesis are performed on the MW-166-39-44-43 airfoil described in Sect. 2.4. The flight condition of interest is "cruise" or "dash" flight close to the lower corner of the laminar bucket. At this operating condition, a large portion of the boundary layer on the pressure side of the airfoil is laminar and natural transition occurs in the attached shear flow, upstream of the main pressure recovery region on the airfoil that begins at $x/c = 0.77$. Consequently, inflow turbulence can be expected to influence the transition location and therefore the performance of the aircraft. Both previous flight measurements with the same airfoil (Reeh & Tropea, 2015), and XFOIL calculations indicate the lower corner of the laminar bucket at $\alpha = -1.4°$.

At this angle of attack, the flight test aircraft at TU Darmstadt (Guissart *et al.*, 2021) would perform a steady state glide at $U = 38$ m/s. Together with a reference chord of c =1.35 m, this results in $Re = 3.4 \cdot 10^6$. A dynamic viscocity $\mu = 1.77 \cdot 10^{-5}$ Pa·s was selected as a compromise between expected conditions in flight at 1000 m altitude and in the LWT. Shifting ambient conditions during the different test campaigns in the LWT caused the dynamic viscosity to vary in the range $1.73 \cdot 10^{-5} \leqslant \mu \leqslant 1.84 \cdot 10^{-5}$ Pa·s. The reference case is summarized in Table 4.1. The turbulence level for steady flow baseline presented in Chap. 4 is $Tu_u^s = 0.01\%$.

The stability chart in Fig. 3.7a shows the most amplified 2D TS-waves in the range $500 \leqslant f \leqslant 900$ Hz. If a critical n-factor (n_{crit}) of 11 is assumed, the transition is expected to occur at $x/c \approx 0.43$. This matches well with the $x/c = 0.45$ measured on the smooth airfoil at $Tu_u^s = 0.01\%$ and determined by the M-TERA intermittency method, see Fig. 3.6a. With the measurement setup used, $Tu_u^s = 0.01\% = Tu_u^x = 0.02\%$, see Sect. B.3.

The numerical simulations used for comparisons in the following sections were kindly provided by Duncan Ohno.

α	Re	$\mu\ [Pa \cdot s]$
$-1.4°$	$3.4 \cdot 10^6$	$1.77 \cdot 10^{-5}$

Table 4.1.: Reference condition for the MW-166-39-44-43 airfoil.

4.1. Pressure distribution

Although the reference case calls for the geometric angle of attack in flight of $\alpha = \text{-}1.4^\circ$, this AoA in the wind tunnel does not reproduce the flow condition of the reference condition. The presence of the wind tunnel walls influences the flow around the airfoil. The main effects in the current setup are the solid blockage and streamline curvature effects, see Barlow *et al.* (1999) for more details. To compensate for the influence of the walls, the geometric angle of attack of the airfoil model was adjusted to match the pressure gradient, as computed by XFOIL for the free flight reference condition. The matching was performed in the range $0.05 < x/c < 0.40$, which covers the main region of TS-wave amplification. Hereafter, α_{ref} is used to denote the reference condition $\alpha = \text{-}1.4^\circ$ in flight and in simulations as well as the corresponding geometric angle of attack of -0.7° in the wind tunnel.

The pressure taps in the region $0.05 < x/c < 0.12$ were found to have a slight influence on the boundary layer transition, and were closed during the initial transition investigations using a 40-50 μm thick adhesive tape. For the test campaigns with a) IR transition measurements and b) with oscillating inflow angle, all taps upstream of $x/c = 0.166$ were permanently closed. Steady pressure distributions presented in this thesis, e.g. Fig. 4.1, are therefore a combination of two measurement, one for $0.0 < x/c < 0.150$ and a separate one for $0.166 \leqslant x/c \leqslant 0.727$ where the taps at $0.0 \leqslant x/c \leqslant 0.134$ on the pressure side were closed.

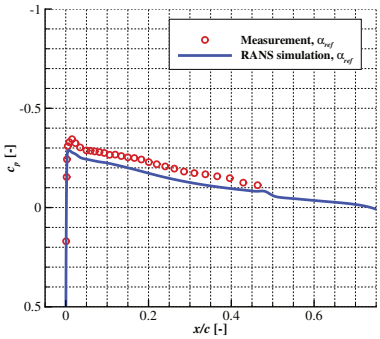

Figure 4.1.: Pressure distribution from measurement and RANS simulation. After Romblad *et al.* (2018).

Figure 4.1 shows a comparison between the measured pressure distribution and RANS simulations. The shape of the pressure distribution is close to linear with a nearly constant pressure gradient. There is good agreement

between the experiment and the simulation in the shape of the suction peak and the pressure gradient, two characteristics that are very important for the boundary layer development. As described, the higher absolute level of the measured pressure coefficient is due to the local over-speed at the model location, caused by the solid blockage in the wind tunnel. The effect of the over-speed on the boundary layer development of the current case is regarded as small. However, even though small, the effects of the over-speed on the boundary layer development as well as the physical frequencies of the most unstable TS-modes are complex, and the data in the following figures are therefore not corrected for the increased flow velocity.

4.2. Mean boundary layer parameters

The mean boundary layer parameters displacement thickness, the momentum thickness and the shape factor (δ_1, δ_2 and H_{12} respectively) provide a good, basic description of the boundary layer development. In the laminar part of the boundary layer, the mean boundary layer parameters of the hot-wire measurement compare well with 2D DNS results, as seen in Fig. 4.2. The measured displacement thicknesses and shape factors are slightly lower than the simulations, while the momentum thickness matches very well. The drop in H_{12} that indicates the transition location occurs earlier in the measurement than in the simulation. The earlier transition in the measurements presented in Fig. 4.2 is caused by a) additional disturbances from the tape covering the pressure taps and the universal disturbance source (see Sect. 2.4) and b) the presence of the hot-wire traversing mechanism.

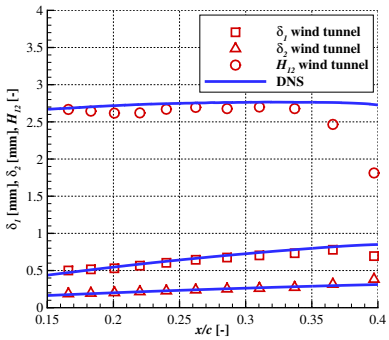

Figure 4.2.: Mean boundary layer parameters from measurements and DNS. After Romblad *et al.* (2018).

The normalized boundary layer profiles in the laminar region $0.166 \leqslant x/c \leqslant$

0.337 are shown in Fig. 4.3. The high level of similarity between the boundary layer profiles agrees with the near-constant shape factor. The measured velocity profile at $x/c = 0.166$ matches well with the one from the 2D DNS.

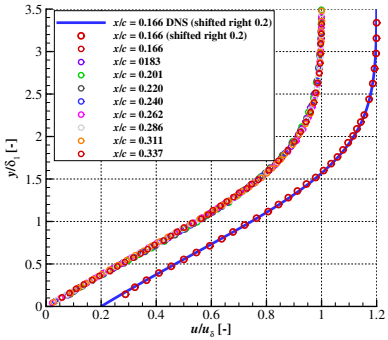

Figure 4.3.: Measured boundary layer velocity profiles. Shifted to the right is a comparison between measurement and 2D DNS for $x/c = 0.166$. After Romblad *et al.* (2018).

4.3. Eigenfunctions and amplification rates

The measured boundary layer eigenfunctions are exemplified by the station $x/c = 0.262$ and a frequency range of $863 \leqslant f \leqslant 953$ Hz shown in Fig. 4.4 together with 2D DNS results at $f = 908$ Hz. The main characteristics compare well, despite the mix of 2D and 3D modes present in the experiment. The main difference being an overshoot at the first wall-near maximum that is likely an effect of scatter in the measurement.

The amplification rates in Fig. 4.5 show a good agreement between the hot-wire measurements, linear stability theory and DNS in the most amplified range of frequencies. The good correspondence means that the small influence on the boundary layer resulting from adhesive tapes on the model surface (see Sect. 2.4) and the presence of the hot-wire traversing unit can be seen as an increased initial disturbance level A_0 due to local receptivity, and that the stability characteristics of the boundary layer are not altered.

4.4. Wall pressure fluctuations

Figure 4.6 depicts spectra of fluctuating wall pressure. Upstream of $x/c = 0.286$ the disturbances in the boundary layer are below the electronic noise

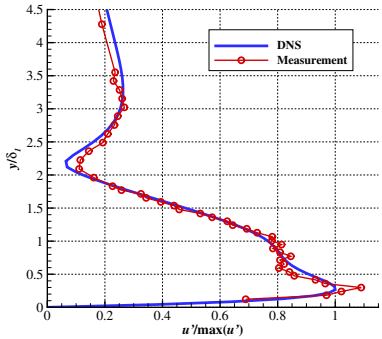

Figure 4.4.: Eigenfunctions at $x/c = 0.262$, hot-wire measurement for $863 \leqslant f \leqslant 953$ Hz and DNS for $f = 908$ Hz. 2D waves used in the simulation. After Romblad *et al.* (2018).

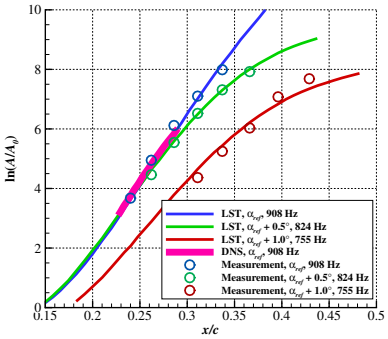

Figure 4.5.: Comparison of measured amplification rates with 2D LST and DNS. After Romblad *et al.* (2022*b*).

floor of the measurement equipment. At $x/c = 0.286$ a region of amplified TS waves with a center frequency of $f \approx 1000$ Hz can be discerned. Moving downstream, the TS waves are amplified further and the frequency of the most amplified disturbances is shifted toward lower frequencies. At $x/c = 0.396$, higher harmonics and amplification of some lower frequencies appear. Further downstream, at $x/c = 0.464$, strong non-linear effects manifest themselves by a fill-up of the spectrum both above and below the most amplified frequency. For $x/c \geqslant 0.540$ the flow is evidently turbulent, as seen from the typical wideband spectrum.

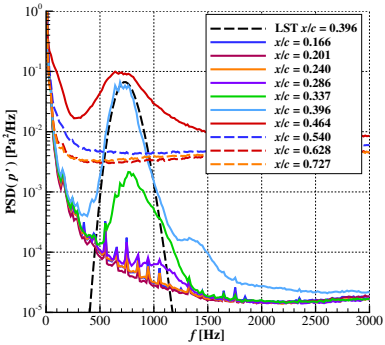

Figure 4.6.: Spectra of unsteady surface pressures compared with 2D LST at $x/c = 0.396$. The LST results are transformed from u'_{max} to p'. After Romblad *et al.* (2022*b*).

The combination of 2D and 3D waves in the boundary layer makes a direct comparison with linear stability theory difficult. Figure 4.6 includes a spectrum based on 2D LST, transformed to p' as described in Sect. 2.6.5. The comparison shows a good match in both center frequency and width of the amplified region of TS frequencies. This LST spectrum is based on a flat distribution of initial disturbances A_0 and the initial amplitude has been adjusted to match the peak amplitude of the experiment. In summary, the spectra describes the characteristic disturbance growth that is typical for a classic, TS-dominated transition process at low turbulence levels and a moderate adverse pressure gradient, see Wubben *et al.* (1990), Kachanov (1994) and Boiko *et al.* (2011).

4.5. Spectra of u' as function of wall normal distance

The frequency spectra of the u' component as function of wall normal distance were measured with hot-wire at $x/c = 0.262$, 0.311 and 0.337 are shown in

Fig. 4.7a-c. As the flow moves downstream from Fig. 4.7a through c, the growth of TS-waves in the range $500 \leqslant f \leqslant 1100$ Hz is seen. The typical TS-eigenmodes, as exemplified by Fig. 4.4, are clearly seen in the y-direction. The already mentioned fill-up of the spectrum outside the TS-range that is typical for the non-linear stage of the transition is well captured in Fig. 4.7c. The surface pressure spectra in Fig. 4.6 show the same behavior for increasing x/c.

4.6. Spanwise wavenumber spectrum

Using the unsteady pressures in the spanwise row of pressure taps at $x/c = 0.311$, the spanwise wavenumber spectrum can be deduced, as depicted in Fig. 4.8a. Compared to the energy spectrum from linear stability theory in Fig. 4.8b, there is a good agreement in the region of highest amplification but the measurement does not contain as much energy at larger wavenumbers. The main characteristics of the wavenumber spectrum in Fig. 4.8a agrees well with the flight measurements on the same airfoil by Guissart *et al.* (2021), and by Reeh & Tropea (2015). A comparison with Guissart *et al.* (2021) is presented in Fig. 5.11.

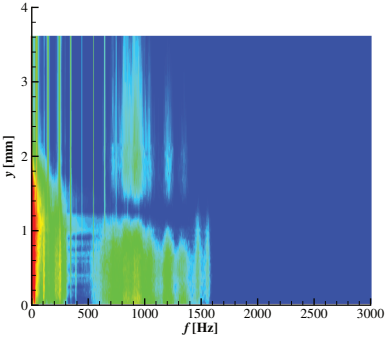

(a) $x/c = 0.262$.

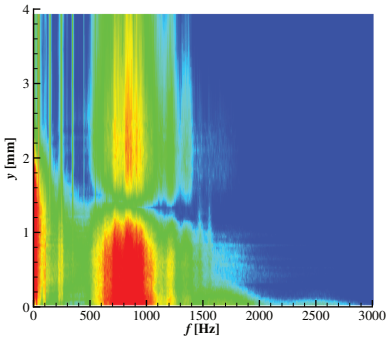

(b) $x/c = 0.311$.

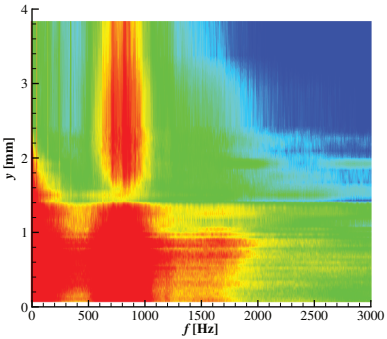

(c) $x/c = 0.337$.

Figure 4.7.: Frequency spectra of the u' component as function of wall normal distance. After Romblad *et al.* (2018).

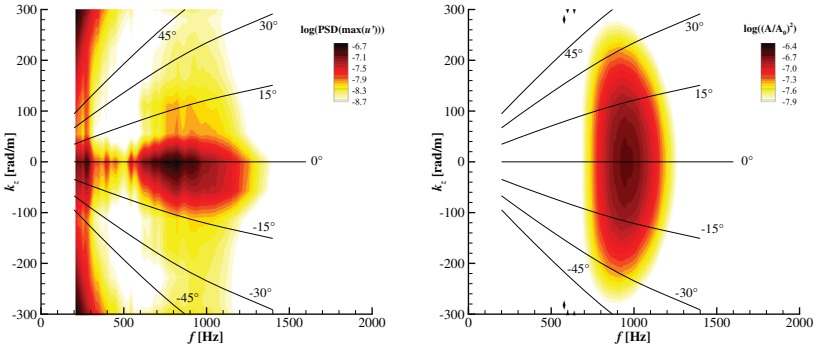

(a) From measured wall pressure fluctuations.

(b) From 2D LST. After Romblad *et al.* (2018)

Figure 4.8.: Frequency wavenumber spectra at $x/c = 0.311$ and α_{ref}.

5. The influence of small-scale turbulence on transition

The influence of small-scale turbulence in the range $0.01\% \leqslant Tu_u^s \leqslant 0.11\%$ on the boundary layer transition was investigated using the active grid described in Sect. 2.2.2. This range of low turbulence levels corresponds to calm weather conditions or flight at high altitudes at which $4.3 \cdot 10^{-8} \leqslant \varepsilon \leqslant 3.1 \cdot 10^{-3}$ m^2/s^3. The low Tu-range is particularly interesting since the trend of $n_{crit}(Tu)$ established by Mack (1977) and van Ingen (1977) points at an increased sensitivity of n_{crit} with diminishing Tu. However, both Mack (1977) and van Ingen (1977) use the classical flat plate measurements by Schubauer & Skramstad (1947) for their models. These measurements exhibit a leveling out of $n_{crit}(Tu)$ below $Tu \approx 0.1\%$. Loehrke *et al.* (1975) attributed this behavior to acoustic disturbances in the experiment. Unfortunately, similar and conclusive measurements at more quiet conditions are not available. In response to the lack of appropriate measurements for $Tu < 0.1\%$, Mack defines the applicable range of his modified e^n method as $Tu > 0.1\%$. This excludes a significant range of atmospheric conditions relevant for airfoil boundary layers. To fill this gap, the range $0.01\% \leqslant Tu_u^s \leqslant 0.11\%$ is investigated in the following section, see also Romblad *et al.* (2022*b*).

5.1. Mean boundary layer parameters

In the current work, it is assumed that the small-scale free-stream turbulence only influences the boundary layer by feeding it with disturbances via the path of receptivity. If this is the case, the base flow over the airfoil is unaffected by the turbulence in the region where the disturbance growth is linear. This assumption is verified by the mean boundary layer parameters shown in Fig. 5.1. Up to the point of transition, the parameters δ_1, δ_2 and H_{12} are essentially unchanged across the range $0.01\% \leqslant Tu_u^s \leqslant 0.11\%$. However, the transition location moves significantly, which is clearly seen by the drop in H_{12}. Note that no measurements past the transition point were made for $Tu_u^s = 0.05\%$ and 0.07%. Consequently, no drop in H_{12} is seen for those Tu in Fig. 5.1.

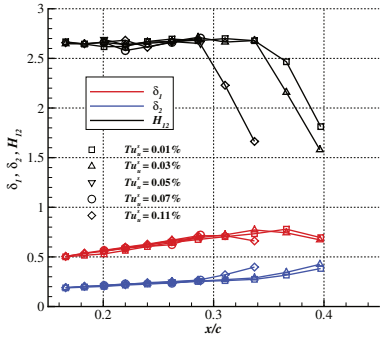

Figure 5.1.: Mean boundary layer parameters obtained for $0.01\% \leqslant Tu_u^s \leqslant 0.11\%$.

5.2. Wall pressure fluctuations

The spectra of the fluctuating wall pressures at α_{ref} for $Tu_u^s = 0.01\%$, 0.05% and 0.11% clearly show the upstream transition movement with increasing Tu, see Fig. 5.2. With increasing Tu the TS peak broadens significantly and the peak amplitude is reduced. The frequency of the peak is shifted toward higher frequencies, an effect that, at least partly, can be attributed to linear stability characteristics emphasizing disturbances with higher frequencies further upstream.

Figure 5.3 shows a comparison between surface pressure spectra from the measurements with $Tu_u^s = 0.07\%$ and direct numerical simulations (DNS). For details of the DNS setup, see "Case 1" in Ohno *et al.* (2020), which is identical to the one in Fig. 5.3b except for the latter having the energy of the free-stream turbulence spectrum increased by a factor of 10. The level of the turbulence spectrum of "Case 1" in Ohno *et al.* (2020) is matched to the spectrum in the tunnel at $Tu_u^s = 0.01\%$. As seen in Fig. 5.3, there is a good match of both the range of the amplified frequencies and the increase in amplitude in the streamwise direction. In the wind tunnel measurements the electronic noise masks the amplified TS-regions upstream of $x/c = 0.2$. The trend of decreasing disturbance levels downstream the transition seen in the experiment is not fully captured in the simulation.

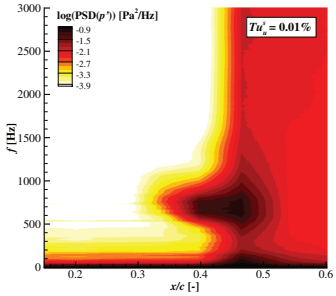

(a) $Tu_u^s = 0.01\%$.

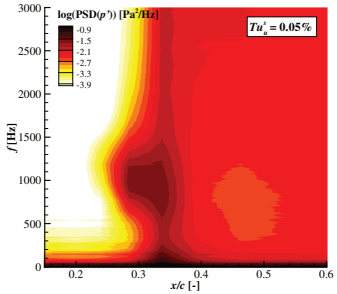

(b) $Tu_u^s = 0.05\%$.

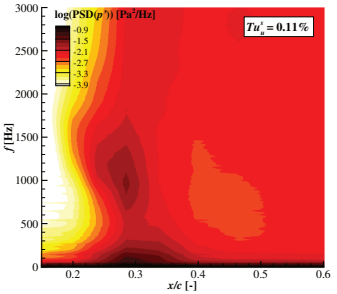

(c) $Tu_u^s = 0.11\%$.

Figure 5.2.: PSD of wall pressure fluctuations at increased turbulence level. After Romblad *et al.* (2022*b*).

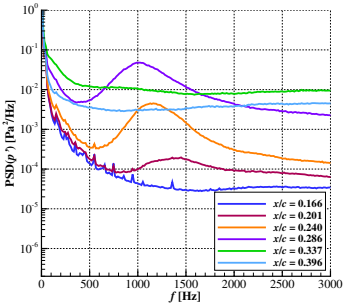

(a) Wind tunnel at $Tu_u^s = 0.07\%$.

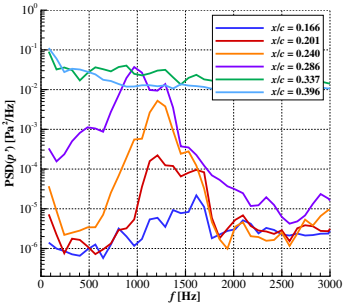

(b) 3D DNS, corresp. to "Case 1" in Ohno *et al.* (2020) with a factor 10 more turbulence energy.

Figure 5.3.: Spectra of fluctuating surface pressures at α_{ref}.

5.3. Spanwise wavenumber spectrum

The spanwise wavenumber spectra of Fig. 5.4 reveals how the increased Tu_u^s influences the distribution between straight (wavenumber $k_z = 0$) and oblique TS waves. The spectra are deduced from the spanwise row of unsteady surface pressures measured at $x/c = 0.311$. Since the increased Tu_u^s moves the transition upstream, the angle of attack of the two cases have been selected to position a similar stage of the transition process at the x/c of the spanwise row pressure taps. This method of adjusting the transition location is somewhat coarse, but still provides qualitative information about the influence of increased levels of Tu_u^s. As seen in Fig. 5.4, the increase in turbulence level from 0.01% to 0.07% reduces the TS-peaks slightly and increases the energy at more oblique waves (higher wavenumbers). The local receptivity properties of the two cases should be close, and the spectral wavenumber content of the free-stream disturbances are expected to be similar. Consequently, the differences seen in Fig. 5.4 are most probably linked to the disturbance development in the boundary layer.

5.4. Temporal development of the unsteady surface pressures

The increase of turbulence leads to a change in the structure of the transition process, which can be seen in the time traces of the unsteady surface pressures. By plotting the time traces of the different pressure taps side by side it is possible to track how disturbances grow as they travel downstream, see Fig. 5.5. With increasing Tu the quasi-uniform nature of the transition at

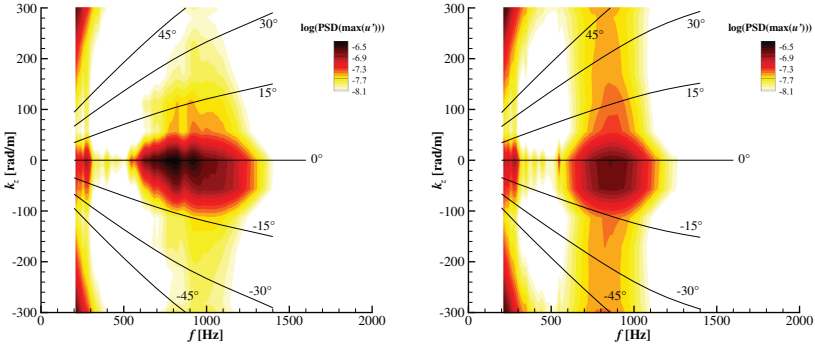

(a) $Tu_u^s = 0.02\%$, $\alpha_{ref} - 0.2°$. (b) $Tu_u^s = 0.07\%$, $\alpha_{ref} + 1.0°$.

Figure 5.4.: Frequency wavenumber spectra of u'_{max}, calculated from the measured p' at $x/c = 0.311$. After Romblad *et al.* (2022*b*).

$Tu_u^s = 0.01\%$ (Fig. 5.5a) is gradually replaced by a structure where isolated wave packets form (Fig. 5.5b). These wave packets grow in both length and amplitude, finally turning into turbulent spots. Clearly visible in Fig. 5.5b are the "calmed regions" downstream the turbulent spots. Similar time traces are have been recorded by e.g. Gostelow *et al.* (1997). The low level of surface pressure fluctuations in these regions are a result of the more stable boundary layer caused by the relaxation after the passing of the turbulent spot.

Kendall (1990) reports wave packets similar to those in Fig. 5.5b appearing in the boundary layer on a flat plate when Tu_u is increased from 0.03% to $Tu_u \leqslant 0.1\%$. In flight measurements, Seitz & Horstmann (2006) observed wave packets at $Tu \geqslant 0.05\%$ and Peltzer (2008) mentions local disturbances in measurements in calm air that, based on the description, may have been wave packets.

The creation of wave packets in the boundary layer is probably linked to an interaction between TS-waves and streamwise structures with "streaky", low frequency characteristics, the so called Klebanoff modes (Klebanoff, 1971). According to Wu & Choudhari (2001) as well as Fasel (2002), the Klebanoff modes cause local and temporal variations of the stability characteristics of the boundary layer. These variations can lead to a significantly faster amplification of disturbances than in the undisturbed boundary layer, thus creating local wave packets.

If the presence of wave packets is coupled to an interaction between TS-waves and Klebanoff modes, care should be taken when extrapolating results obtained in wind tunnels to flight conditions. Even if the spectral levels in

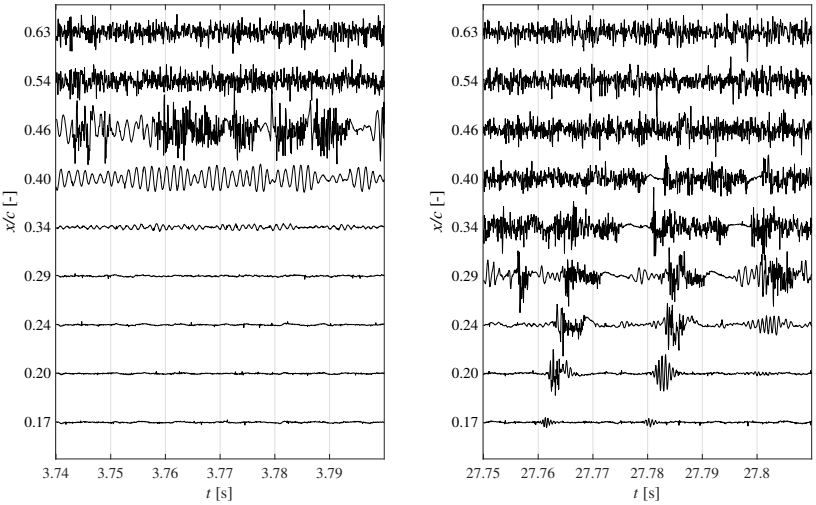

(a) $Tu_u^s = 0.01\%$. (b) $Tu_u^s = 0.11\%$.

Figure 5.5.: Time traces of the unsteady surface pressures at α_{ref}.

the TS range match well between turbulence in the atmosphere and the wind tunnel, the energy levels at low frequencies are very different. The atmospheric turbulence contains significantly more energy at the low frequencies than seen in the wind tunnel. Figure 3.1a highlights this phenomenon. As the Klebanoff modes are linked to low frequencies and the TS-waves to high frequencies, different ratios between the energy in the two frequency ranges may influence the interaction effects described by Wu & Choudhari (2001) and Fasel (2002). This in turn may have an effect on the occurrence of wave packets and the final breakdown to a turbulent boundary layer.

5.5. The presence of Klebanoff modes at low Tu

Many of the investigations of Klebanoff modes found in the literature have been conducted at $Tu \gtrsim 1.0\%$, for example Matsubara & Alfredsson (2001) and Brandt *et al.* (2004). At these high levels of Tu the Klebanoff modes tend to be responsible for so-called bypass transition, as described by e.g. Fransson *et al.* (2005). However, Klebanoff modes also exist at lower Tu (Arnal & Juillen, 1978; Kendall, 1985), although the literature on the subject is sparse. Even though the current experiments were not designed to measure Klebanoff modes directly, their presence can be seen in the boundary layer hot-wire

measurements. The frequency spectra of the u' component as function of wall normal distance at $x/c = 0.166$ in Fig. 5.6 reveals a progressive increase of low frequency energy in the boundary layer with increasing Tu. At this streamwise station the TS wave amplitude is below the electronic noise floor. The bands in Fig. 5.6 extending up to $y/\delta_1 = 6$ are electronic disturbances, and the bands around 700, 830, 1400 and 1530 Hz are likely an effect of probe vibrations.

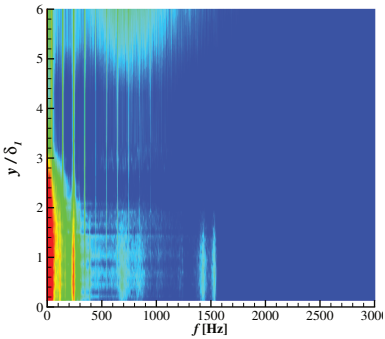

(a) $Tu_u^s = 0.01\%$.

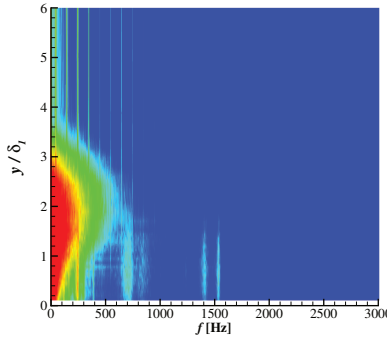

(b) $Tu_u^s = 0.03\%$.

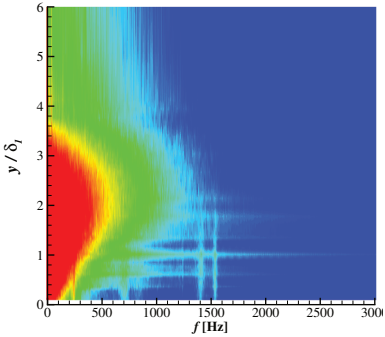

(c) $Tu_u^s = 0.11\%$.

Figure 5.6.: Frequency spectra of the u' component as function of wall normal distance at $x/c = 0.166$.

The broadband eigenfunction at $x/c = 0.166$ at $Tu_u^s = 0.11\%$ in Fig. 5.7a exhibits the characteristic shape seen in boundary layer flows where Klebanoff modes are present. Figure 5.7b depicts eigenfunctions from the literature (compiled by Boiko *et al.* (2002)). The similarity between the present mea-

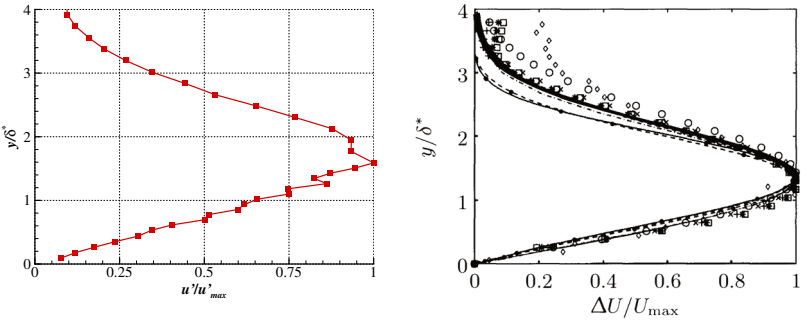

(a) Hot-wire measurements at $x/c = 0.166$ and $Tu_u^s = 0.11\%$.

(b) A compilation of literature data from Boiko *et al.* (2002)[1], p. 153.

Figure 5.7.: Broadband eigenfunctions.

surement and the literature data is striking, and confirms the presence of Klebanoff modes in the current measurements. The slightly larger extension in the y-direction of the current measurement is probably linked to a scatter in δ^* used for the normalization.

The presence of Klebanoff modes in the boundary layer supports the hypothesis that the wave packets seen in the time traces of the surface pressures (Fig. 5.5) are a result of an interaction between the Klebanoff modes and the TS waves.

5.6. Distributed receptivity

The path for free-stream disturbances into the boundary layer is via receptivity, see Morkovin (1969) and the overview by Saric *et al.* (2002). Very simplified, strong local receptivity to both sound and vorticity can be expected in regions with a high surface curvature, surface non-uniformities or strong boundary layer growth. However, an additional mechanism allows free-stream disturbances to enter the boundary layer along the airfoil surface, the so called distributed receptivity (Westin *et al.*, 1994; Kendall, 1998). Characteristic for the distributed receptivity is that the disturbances feed into the boundary layer at an approximately constant ratio along the airfoil chord. As a result, disturbances grow also where the TS amplification is unity. This type of disturbance growth is often referred to as linear or algebraic growth, as opposed to the exponential growth of the TS waves.

[1] Reproduced with permission from Springer Nature

The algebraic growth of disturbances can be observed in the current measurements by examining the combinations of x/c and f for which no TS amplification occurs, i.e. $\alpha_i = 0$. Figure 5.8 shows the growth rate of disturbances in the boundary layer at $\alpha = \alpha_{ref} + 0.4°$. TS waves, as calculated by LST in the most amplified frequency range, are clearly seen to grow exponentially. However, the measured disturbance growth where $\alpha_i = 0$ (at $Tu_u^x = 0.13\%$, grid $d16M100$) behaves completely different. Apart from $x/c = 0.286$ and 0.311, the rate of increase seen in the surface pressure disturbances is close to constant. This is the result of the continuous feed of disturbance energy into the boundary layer, as described above. The low values of the two most upstream points of the measurement can probably be attributed to a poor signal to noise ratio.

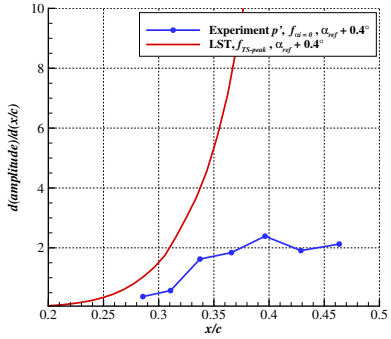

Figure 5.8.: An example of the exponential growth of the TS waves and the linear growth caused by the distributed receptivity, $\alpha = \alpha_{ref} + 0.4°$ and $Tu_u^x = 0.13\%$ (grid $d16M100$).

5.7. The Tu-dependency of the transition location

In the design of NLF airfoils for turbulent conditions, modeling the changes in transition location with turbulence level is important. As already mentioned, Mack (1977) proposed a modification to the e^9 (or e^n) method derived from measurements of the transition in flat plate boundary layers. In Mack's modified e^n method, the critical n-factor is expressed as a function of Tu.

$$n_{crit} = -8.43 - 2.4 \cdot ln(Tu) \tag{5.1}$$

In the present work, the turbulence level in the u-direction Tu_u, is used in Eq. 5.1 rather than the total Tu as in Mack (1977). The reason is the

Airfoil	Re	α (geometric) [°]	Side
MW-166-39-44-43	$3.4 \cdot 10^6$	-0.7	Pressure
XIS40mod	$1.5 \cdot 10^6$	2.0	Suction
NACA64-418	$1.5 \cdot 10^6$	6.2	Suction

Table 5.1.: The airfoils and corresponding test conditions for the transition location investigation using IR thermography.

differences in the turbulence spectra of the current measurements and the ones by Schubauer & Skramstad (1947) that were used by Mack (1977).

At the $U_\infty = 38$ m/s of the current measurements, the spectra of the u, v and w components are approximately similar in the TS-range $500 \lesssim f \lesssim 3000$ Hz, as exemplified by Fig. B.3. However, for frequencies $f \lesssim 400$ Hz, the spectra of the v and w components contain more energy than the u component. The differences in the low-frequency part of the spectra are caused by the contraction in the wind tunnel that attenuates the large length scales of the streamwise turbulence, see Sect. 3.1.1 and App. B. This anisotropy of the turbulence at low frequencies was also observed by Schubauer & Skramstad (1947). In contrast to the current measurements, the anisotropy observed by Schubauer & Skramstad (1947) diminished with decreasing Tu, and it appears their turbulence was approximately isotropic in the Tu-range of interest here. The spectrum of the u-component at $Tu_u = 0.033\%$ shown in Schubauer & Skramstad (1947) flattens out for $f \lesssim 200$ Hz, which is comparable to the u-spectrum in the current measurements.

The higher turbulence energy in the v and w direction for $f \lesssim 400$ Hz observed in the current measurements means that, if the total Tu is used in the modified e^n method of Mack (1977), the energy in the TS-range is overestimated. However, the u-spectra in the current measurements and in those of Schubauer & Skramstad (1947) have similar energy distributions, and the turbulence in the latter is approximately isotropic, meaning $Tu \approx Tu_u$. Thus, using the Tu_u of the current measurement in Mack's modified e^n method provides a representative level of turbulence in the TS-range.

In order to investigate how applicable the modified e^n method of Mack (1977) is for cases with different base flow, IR thermography was used to determine the transition location for three different airfoils over a range of Tu. The airfoils used are the MW-166-39-44-43, XIS40mod and NACA64-418. They were selected in order to cover a range of significantly different base flows. Table 5.1 lists the cases investigated and Fig. 5.9a shows the c_p distributions of the three airfoils.

The response of the three airfoils to increased turbulence, expressed in $n_{crit}(Tu_u)$, can be seen in Fig. 5.9b. The transition on the pressure side of the MW-166-39-44-43 follows the modified e^n method of Mack (1977) well,

whereas the two other airfoils show significantly smaller variations of n_{crit} for the same range of Tu_u. The the good agreement with the method of Mack (1977) on the pressure side of the MW-166-39-44-43 airfoil is probably linked to the pressure distribution being similar to the one of a flat plate with a slight adverse pressure gradient. The the modified e^n is based on data for flat plates at zero pressure gradient.

For all three airfoils, the observed variation of n_{crit} over the investigated range of Tu_u is in the order of $\Delta n \geqslant 2$, which is significant in the context of NLF airfoil design. The differences in the gradient of $n_{crit}(Tu_u)$ between the three airfoils show that the modified e^n method of Mack needs to be used with caution, if applied to other cases than flat plates at zero pressure gradient. Still, in the current measurements, the errors in n_{crit} from Mack's method due to the differences in the $n_{crit}(Tu_u)$ gradients are of the same order as the inherent limitations of the e^n method itself, as exemplified by the differences in n_{crit} between the NACA64-418 and the XIS40mod, see Fig. 5.9b.

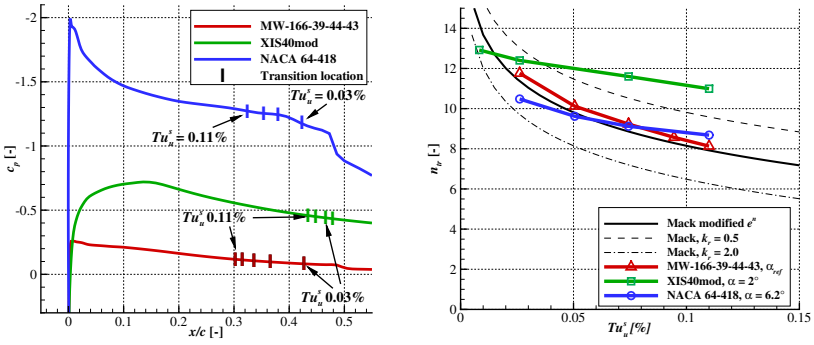

(a) Steady pressure distributions.

(b) n_{crit} as function of Tu_u^s.

Figure 5.9.: The influence on the transition from the turbulence level, all three airfoils. After Romblad *et al.* (2022*b*).

The question arises, whether the difference seen between the three airfoils is linked to differences in their local receptivity properties. The receptivity is dependent on various parameters including the local surface curvatures, the non-dimensional frequency and the boundary layer parameters close to branch I (Saric *et al.*, 2002).

The receptivity coefficient G, can be expressed as the ratio between the external disturbance and the resulting TS wave amplitude at branch I A_0, as described for free-stream sound by Reed *et al.* (2015). Using the definition of Reed *et al.* (2015) for free-stream turbulence gives $A_0 = Tu \cdot G$. This means

that variations in Tu and G have the same effect on the TS amplitudes in the boundary layer, and thereby the transition.

Equation 5.1 already includes the effect of receptivity in the flat plate experiments employed by Mack (1977). The level of the receptivity coefficient in these measurements is not known, but by introducing the receptivity ratio k_r, the effect of variations in the receptivity ratio can be studied.

$$k_r = \frac{G_{Mack}}{G_{Current}} \tag{5.2}$$

where G_{Mack} and $G_{Current}$ are the receptivity coefficients in the measurements used by Mack and in the current experiments respectively. This is a strong simplification as differences in the non-linear regime of transition are also included in this ratio, as well as G being a function of frequency. With these limitations in mind, introducing the receptivity ratio in Eq. 5.1 leads to

$$n_{crit} = -8.43 - 2.4 \cdot ln(k_r \cdot Tu) \tag{5.3}$$

As expected from Eq. 5.3, variations in k_r cause a vertical shift in the n_{crit} curves of Fig. 5.9b, but the gradient does not change. Consequently, the lower sensitivity of the transition location to variations in Tu_u observed for the XIS40mod and NACA64-418 compared to the MW-166-39-44-43 cannot be captured by a change in local receptivity coefficient alone. By the same reasoning, the higher n_{crit} levels exhibited by the XIS40mod compared to the NACA64-418 is probably connected to differences in receptivity.

Notably, in the investigated range of turbulence, none of the airfoils exhibits a lower limit of Tu below which the transition location no longer change. This contradicts the results of Schubauer & Skramstad (1947) and of Wells (1967), but is expected from available research on receptivity, including Morkovin (1969), Kendall (1998), Kachanov (2000) and Saric *et al.* (2002). The current results are also in line with the description of Loehrke *et al.* (1975), who attributed the nearly constant $n_{crit}(Tu)$ for $Tu < 0.1\%$ in earlier measurements to the acoustic disturbances in the test section and not the actual response of the boundary layer to free-stream turbulence. Loehrke *et al.* (1975) points at some specific datasets exhibiting this phenomenon, including the measurements by Schubauer & Skramstad (1947). The results of Schubauer & Skramstad (1947) were part of the data used by Mack (1977) to derive the modified e^n method.

5.8. Comparison with flight measurements

Flight measurements at flow conditions comparable to the wind tunnel investigations have been conducted at TU Darmstadt using an extensively instrumented “wing glove” with the same MW-166-39-44-43 airfoil (Sect. 2.4), see

Guissart *et al.* (2020) and Guissart *et al.* (2021). The following section compares results from the unsteady pressure measurements in the wind tunnel and in flight.

The main features of the spectra from the individual pressure taps are recognizable in both the tunnel and in flight, see Fig. 5.10. The TS peak at $x/c \approx 0.34$ is amplified and develops higher harmonics at $x/c \approx 0.4$. At $x/c \approx 0.45$ the spectrum is filled up both above and below the TS peak. For $x/c \geqslant 0.55$ the spectrum attains the broadband shape that is characteristic for a turbulent boundary layer. The most amplified frequencies in the wind tunnel measurements are $f_{TS} \approx 700$ Hz, and in flight $f_{TS} \approx 1100$ Hz. This discrepancy is related to slight differences in the conditions in U_∞ and ν. If the non-dimensional frequency F is used, both the wind tunnel spectra and those from the flight measurements show peak amplification at $F \approx 5000$, as seen in Fig. 5.10.

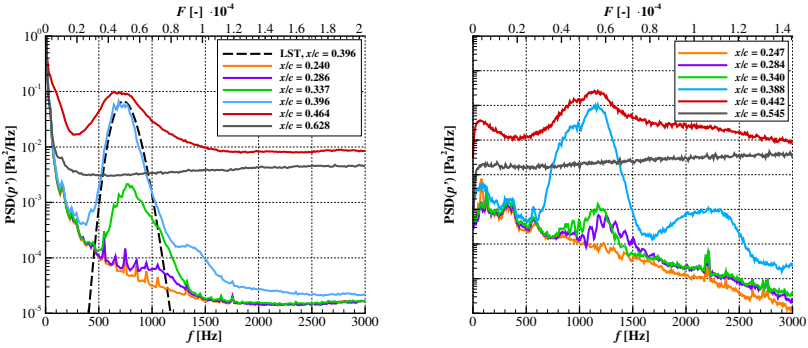

(a) Wind tunnel at $Tu_u^s = 0.01\%$, $\varepsilon^s = 4.3 \cdot 10^{-8}$ m^2/s^3.

(b) Flight measurement at $\varepsilon^x = 4.8 \cdot 10^{-7}$ m^2/s^3.

Figure 5.10.: Spectra of fluctuating surface pressures at α_{ref}.

The frequency wavenumber spectra in Fig. 5.11 show a reasonable correspondence between the wind tunnel and flight at $x/c = 0.311$ and $x/c = 0.34$ respectively. There are distinct energy maxima for waves with small wavenumbers and the energy level decreases rapidly for increasingly oblique waves. The spectrum in flight shows more energy in straight waves with frequencies below the TS peak than seen in the wind tunnel. This could be caused by the flight measurement showing a slightly later stage in the transition process than in the wind tunnel measurement. Both spectra in Fig. 5.11 correspond qualitatively to the flight measurements on the same airfoil of Reeh & Tropea (2015) at $\alpha = 0.92°$ and $x/c = 0.428$.

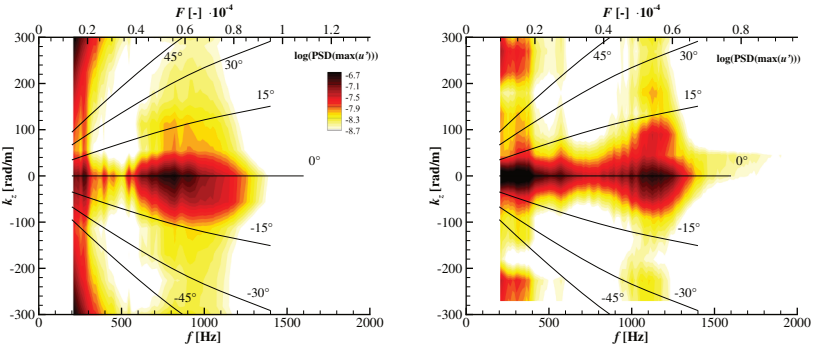

(a) $x/c = 0.311$ in the wind tunnel with $Tu_u^s = 0.01\%$, $\varepsilon^s = 4.3 \cdot 10^{-8}$ m^2/s^3.

(b) $x/c = 0.34$ in flight with $\varepsilon^x = 4.8 \cdot 10^{-7}$ m^2/s^3.

Figure 5.11.: Frequency wavenumber spectra of u'_{max}, calculated from the measured p' at α_{ref}.

Even if there is a qualitative correspondence between wind tunnel and flight measurement in the unsteady surface pressures at the reference condition, significant difference arise when the angle of attack is changed.

As seen in Fig. 5.12, the rms(p')-curves from the wind tunnel measurement shift gradually downstream as the angle of attack increases, as expected from LST (not shown here).

With increasing alpha in the flight measurements, the rms peak moves downstream similar to the wind tunnel measurements between $\alpha = \alpha_{ref} - 0.85°$ and $\alpha_{ref} - 0.55°$. For higher AoA, the movement is much smaller than in the wind tunnel and the growth rate of the disturbances is significantly higher. In the range $\alpha_{ref} - 0.55° \leqslant \alpha \leqslant \alpha_{ref} + 0.50°$ the peak only moves $\Delta x/c = 0.08$ in the flight measurements whereas in the the wind tunnel the movement is $\Delta x/c = 0.18$ for the slighty smaller range $\alpha_{ref} - 0.50° \leqslant \alpha \leqslant \alpha_{ref} + 0.50°$. At $\alpha = \alpha_{ref} - 0.55°$ and $\alpha_{ref} - 0.30°$ the flight measurements exhibit two peaks in the rms(p')-curves, a trend present neither in the wind tunnel, nor in the LST. Differences in the airfoil shape between the wind tunnel model and the glove used in the flight measurements could generate this kind of behavior. However, it has not been possible to determine the actual shape of the wing-glove under flight loads.

The unexpected boundary layer development in the flight measurement makes further comparisons difficult, as exemplified by the response to Tu seen in Fig. 5.13. In the wind tunnel measurement, the broadband disturbance growth and transition location moves gradually upstream as Tu_u^s increase

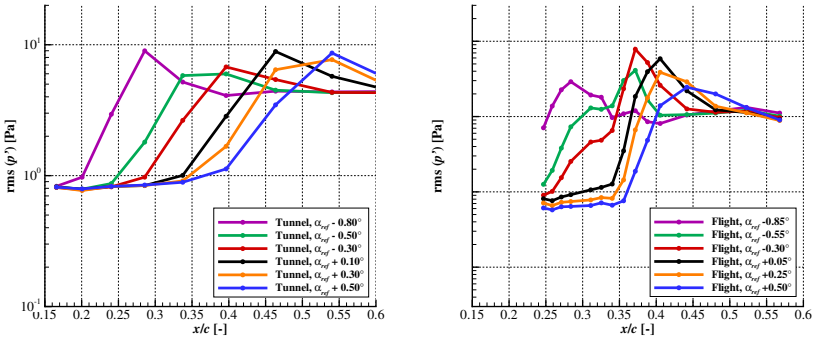

(a) In the wind tunnel with $Tu_u^s = 0.01\%$, $\varepsilon^s = 4.3 \cdot 10^{-8}$ m^2/s^3.

(b) In flight with $\varepsilon^x < 4 \cdot 10^{-7}$ m^2/s^3.

Figure 5.12.: Broadband rms of the surface pressures as function of angle of attack.

from 0.01% to 0.07%. In contrast, the rms curves measured in flight hardly change at all in the corresponding range of ε.

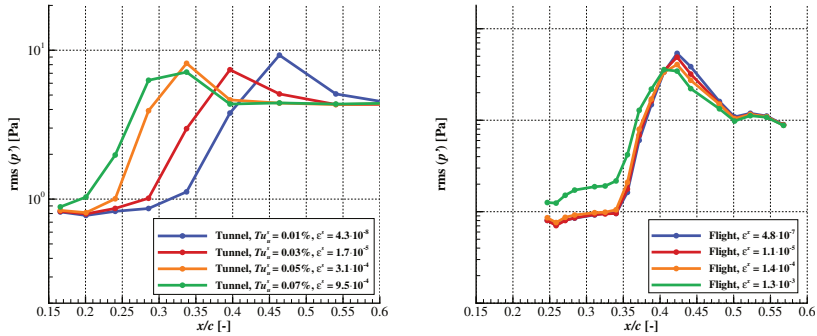

(a) In the wind tunnel.

(b) In flight.

Figure 5.13.: Broadband rms of the surface pressures as function of ε at α_{ref}.

5.9. Conclusions - the influence of small-scale turbulence

The response of the laminar boundary layer and transition to free-stream turbulence was investigated in a series of wind tunnel measurements on the pressure side of the NLF aifoil MW-166-39-44-43 in the range $0.01\% \leqslant Tu_u^s \leqslant 0.11\%$. The spectral distribution of the turbulence in the frequency range of the most amplified TS-waves was matched to those measured in free-flight.

Even though the base flow does not change when increasing the Tu_u^s from 0.01% to 0.11%, the transition on the airfoil moves upstream. The TS peak broadens and shifts to higher frequencies. As the free-stream disturbances enter the boundary layer through receptivity, the increased Tu cause higher levels of initial disturbances A_0 at branch I. The disturbances in the boundary layer undergo TS amplification and the higher A_0 result in an earlier transition. Even if the leading edge and surface non-uniformities tend to be areas with high receptivity, the current measurements also show distributed receptivity, with its characteristic linear disturbance growth.

With increasing Tu, the current measurements show a flow structure with isolated wave packets gradually replacing the quasi-uniform nature of the transition at low Tu, and more energy is found at high spanwise wave numbers. The likely cause of the appearance of wave packets is an interaction between TS-waves and Klebanoff modes. Klebanoff modes are typically associated with higher Tu, but the frequency spectra of the u' component as function of wall normal distance as well as the broadband eigenfunctions indicate their presence in the current measurements at Tu_u^s as low as 0.01%.

Comparisons with flight measurements at α_{ref} and low Tu show that the main characteristics of the surface pressure spectra are similar when plotted over non-dimensional frequency. The frequency wavenumber spectra exhibit a good agreement in the distribution between straight and oblique waves. The flight measurements show an unexpected disturbance development in the boundary layer with angle of attack and Tu, which makes further comparisons difficult.

For the MW-166-39-44-43 airfoil, the Tu-dependency of the critical n-factor is close to the modified e^n method of Mack (1977) in the investigated range $0.03\% \leqslant Tu_u^s \leqslant 0.11\%$. This contradicts classic measurements of Schubauer & Skramstad (1947) and Wells (1967), which indicated a lower limit for the applicability of the modified e^n method at $Tu = 0.1\%$. The two airfoils XIS40mod and the NACA64-418 both show a lower sensitivity of n_{crit} to Tu compared to the MW-166-39-44-43. However, the variation in the investigated range of Tu is still in the order of $\Delta n \geqslant 2$, which is significant when considering NLF airfoil design. The pressure distribution on the pressure side of the MW-166-39-44-43 airfoil shows large similarities with the one of a flat plate with a slight adverse pressure gradient. These similarities probably explain the good match between the airfoil and Mack's method, the latter

being based on data for flat plates. A simplified evaluation indicates that presumed differences in the level of the local receptivity coefficients are not sufficient to explain the lower sensitivity of n_{crit} to Tu for the XIS40mod and NACA64-418 airfoils.

The results indicate that the modified e^n method of Mack (1977) is applicable in the range $0.01\% \leqslant Tu_u^s \leqslant 0.11\%$, but also that the method should be used with care since it does not model differences between airfoils or baseflows.

6. The influence of large-scale turbulence on transition

The effect of large-scale turbulence on the boundary layer transition is fundamentally different to the impact of small-scale turbulence described in Chap. 5. Flight through large-scale turbulent eddies causes fast variations of the inflow angle, resulting in fluctuations of the airfoil pressure distribution, to which the boundary layer responds, see Reeh (2014). In this section, the response of the boundary layer transition to large-scale turbulence is investigated through wind tunnel measurements. In the wind tunnel, the large-scale turbulence is approximated by 2D, single-mode oscillations of the inflow angle in pitch-direction. The inflow angle oscillations are generated by the gust generator described in Sect. 2.3 and characterized in Sect. 3.2. In the measurements of Chap. 6, the inflow oscillates around the reference case α_{main} = α_{ref} = -0.7° with an equivalent zero-to-peak amplitude of $\alpha_{inflow} \sim 0.5°$. The free-stream turbulence level of the investigation is the base $Tu_u^x = 0.02\%$ level.

The results of the current measurements are compared to data of Obremski & Fejer (1967) as well as to Studer *et al.* (2006). However, it should be pointed out that the three experiments represent different levels of unsteadiness. The nature of the unsteady transition can be separated in a "creative" and a "convective" mode, as described by Obremski & Fejer (1967). In the "creative" mode, the transition is governed by the growth of instability waves with subsequent breakdown to turbulence, similar to the steady case. The transition location depends on the initial disturbance level and the integrated amplification along the trajectories of the instability waves. This is in stark contrast to the "convective" transition mode, in which the transition location moves downstream with a constant velocity similar to the edge velocities of a turbulent spot. Instability waves have little or no influence on the transition location in the "convective" transition mode.

The measurements of Obremski & Fejer (1967) include cases with isolated turbulent spots and a "convective" transition mode in which the downstream moving transition fronts are very similar to the edges of a turbulent spot. In comparison, the most unsteady case studied by Studer *et al.* (2006) does not exhibit the isolated turbulent spots of Obremski & Fejer (1967), but the convective transition mode is present. As will be seen later in this section, the current measurements exhibit a clearly unsteady boundary layer behavior,

but not a convective transition mode.

Ohno *et al.* (2022) suggest assessing the level of unsteadiness quantitatively by using a modified reduced frequency

$$\kappa_{trans} = \frac{2\pi \cdot f_{osc} \cdot \Delta L_{tr}}{U_\infty} \tag{6.1}$$

where the range of movement of the transition location during the oscillation, ΔL_{tr} is used as reference length, rather than the chord length in the original definition of κ. Ohno *et al.* (2020) used the range of transition movement in the corresponding quasi-steady case as reference length, which is not available in Obremski & Fejer (1967) or Studer *et al.* (2006). Note that for numerical reasons, 2π is used in the definition of κ_{trans}, whereas only π is used for κ in this thesis, consistent with the definition of κ in Sect 2.1.

Using the more unsteady cases in each of the experiments discussed above, Eq. 6.1 gives $\kappa_{trans} \sim 4.1$, 1.5 and 0.4 in Obremski & Fejer (1967), Studer *et al.* (2006) and the current measurements respectively. A perfect match between the three datasets is therefore not expected. Instead, the comparisons will highlight differences and similarities between the respective ranges of unsteadiness.

6.1. Unsteady surface pressures and transition location

The response of the boundary layer to the oscillating inflow angle is captured in the measurements of the unsteady surface pressures depicted in Fig. 6.1. The short time rms are plotted together with the C_3 parameter of the M-TERA intermittency method. The color maps of p_{rms} are truncated just above the electronic noise floor, indicated with blue color. For reference, the threshold value used for transition detection is $C_3 = 1 \cdot 10^5$.

In the quasi-steady case $\kappa = 0.06$ (Fig. 6.1a), the characteristic streamwise amplification of disturbances to a peak (left to right in Fig. 6.1) is clearly visible. After the peak, p_{rms} decreases to an almost constant level in the turbulent part of the boundary layer. The time instances $t/T = 0.3$ and 0.7 correspond well with the steady case depicted in Fig. 3.8. The part of the oscillation cycle with upstream movement of the transition front (decreasing inflow angle, $0 < t/T < 0.5$) is symmetric with the downstream moving part of the cycle (increasing inflow angle, $0.5 < t/T < 1.0$).

Even though the movement of α_{gen} is close to sinusoidal, the time-traces of p_{rms} exhibit a somewhat sharper shape at the upstream turning point α_{min}, and a more rounded downstream turning point at α_{max}. This is a result of the slightly non-linear behavior of $x_{tr}(\alpha)$ in this range, combined with the decrease of gust generator authority at the lower end of the α_{gen} range, see Fig. 3.6a.

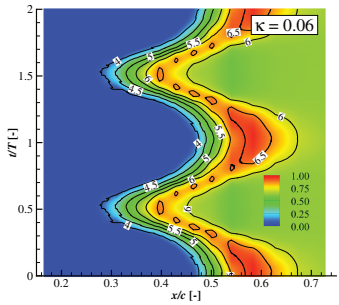

(a) $\kappa = 0.06$.

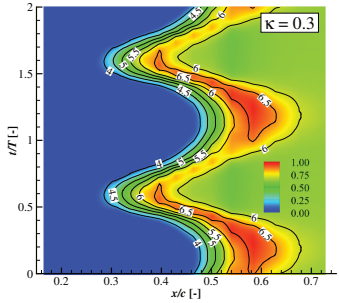

(b) $\kappa = 0.3$.

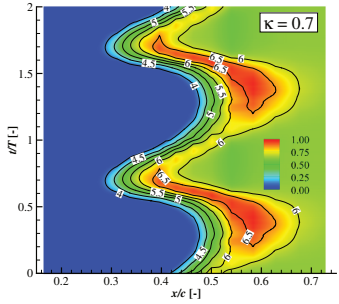

(c) $\kappa = 0.7$.

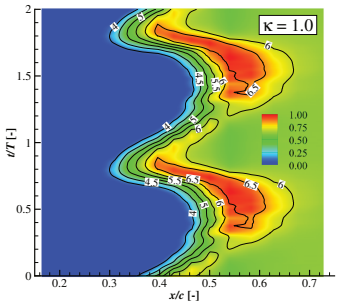

(d) $\kappa = 1.0$.

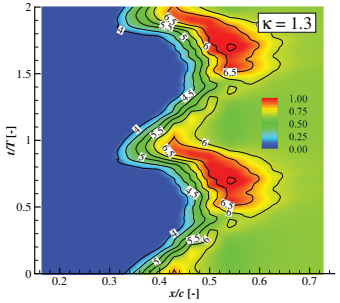

(e) $\kappa = 1.3$.

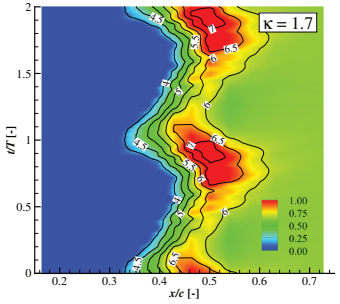

(f) $\kappa = 1.7$.

Figure 6.1.: In color, the logarithm of the cycle averaged short time, broadband rms of the unsteady surface pressures, $log(p_{rms})$ at $\alpha_{main} = \alpha_{ref}$ and $Tu_u^x = 0.02\%$. As contours, the logatithms of the C_3 parameter of the M-TERA transition detection method.

With increasing κ, the boundary layer response to the inflow angle oscillations changes gradually. The temporal symmetry of the p_{rms} time histories in the quasi-steady case is replaced with an asymmetric, "skewed" shape. The region with disturbance amplification moves faster in the upstream direction than in the downstream direction. The M-TERA C_3 parameter indicates the same trend for the transition location. For the upstream moving transition front, increasing κ causes a slight increase of the level of the peak in the $p_{rms}(x)$ distribution. In contrast, the peak decrease markedly during the downstream moving part of the cycle. These changes are well illustrated by the $\kappa = 1.0$ case in Fig. 6.1d. Similar trends were observed by Studer *et al.* (2006) in hot-wire measurements in the vicinity of the maximum of the u'_{wall} normal eigenfunction, and are further discussed below.

Above $\kappa \approx 0.5$ the time histories of p_{rms} and the C_3 parameter indicate a gradual decrease in the range of the transition location movement, and for $\kappa > 1.3$ the movement becomes more saw-tooth shaped. Part of the behavior observed above $\kappa > 1.3$ is likely an effect of the deteriorating signal-to-noise ratio toward higher κ, and not fully representative of the actual response of the boundary layer. Consequently, the highest reduced frequencies in the measurements are excluded from the analysis, where deemed necessary.

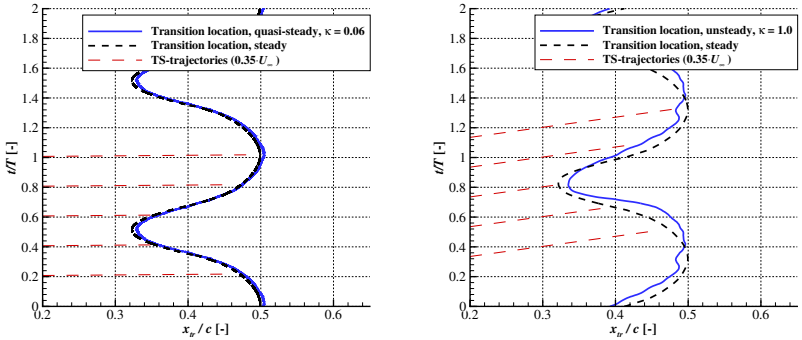

(a) $\kappa = 0.06$. (b) $\kappa = 1.0$.

Figure 6.2.: Steady and unsteady transition location as function of t/T.

The response of the transition to increasing κ becomes clear when plotting the steady and unsteady transition locations together. The steady transition location in Fig. 6.2, is derived from $\alpha_{gen}(t)$ combined with the steady dependence $x_{tr}(\alpha_{gen})$ of Fig. 3.6. To facilitate comparisons, the steady x_{tr} time-trace is shifted to match the time instance of α_{min} in the time-trace of the unsteady transition. Typical TS-trajectories are included to indicate the

level of unsteadiness. As seen in Fig. 6.2a, both the range and the shape of the quasi-steady transition movement at $\kappa = 0.06$ matches the steady behavior very well. In contrast, the time-trace at $\kappa = 1.0$ in Fig. 6.2b clearly exemplifies the "skewed" shape of the unsteady x_{tr} movement. The range of the transition movement at $\kappa = 1.0$ is $\Delta x_{tr}/c$= 0.134, which is slightly smaller than the $\Delta x_{tr}/c = 0.147$ at $\kappa = 0.06$.

The instantaneous spectra of the surface pressures from the continuous wavelet transform (CWT) provides additional information about the transition process. Figure 6.3a depicts the time-frequency spectrum at $x/c = 0.429$ during inflow angle oscillations at $\kappa = 0.06$. At this chordwise station, the boundary layer at $t/T = 0$ is laminar with a clear TS-peak centered around 640 Hz. At $t/T = 0.3$, the boundary layer is more unstable, which results in a TS-peak with a higher level and which covers a wider range of frequencies. A little further in the cycle, at $t/T = 0.4$, the spectrum shows the familiar non-linear stage of the transition process, with a fill-up of the spectrum at both below and above the primary TS-range of frequencies. Disturbances with a frequency of 680 Hz are the most amplified. See Fig. 4.6 for corresponding spectra in steady conditions. For $0.4 < t/T < 0.6$ the boundary layer is turbulent. The spectral development in the part of the oscillation with upstream moving transition, $0 < t/T < 0.5$, is practically symmetric to the development in the downstream moving part, $0.5 < t/T < 1.0$. This indicates that the case $\kappa = 0.06$ is indeed quasi-steady.

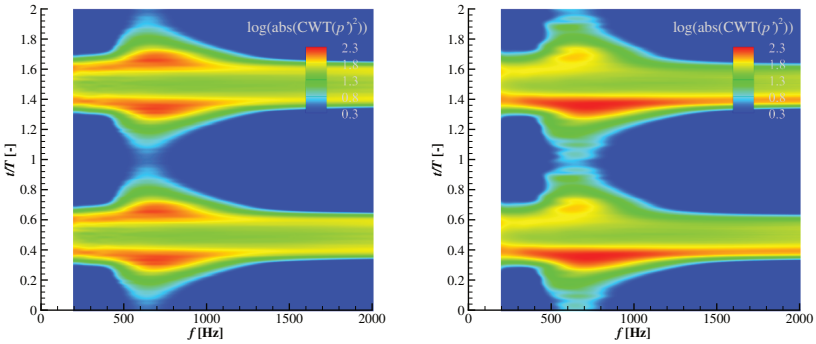

(a) $\kappa = 0.06$. (b) $\kappa = 1.0$.

Figure 6.3.: Time-frequency spectrum of cycle-averaged unsteady surface pressure signals at $x/c = 0.429$. For clarity, the $\kappa = 0.06$ data has been smoothed with a $80{\cdot}f_{gen}$ (40 Hz) LP-filter and the $\kappa = 1.0$ data has been shifted in time to match the $\kappa = 0.06$ case.

At the higher inflow oscillation frequency $\kappa = 1.0$ (Fig. 6.3b), the progression from laminar to turbulent boundary layer with upstream moving transition front ($0 < t/T < 0.5$) shows slightly higher disturbance levels in the TS-region than at $\kappa = 0.06$. The TS amplification at $t/T = 0$ is centered around 640 Hz, the same frequency as seen at $\kappa = 0.06$. The most amplified frequency at $t/T = 0.4$ is 720 Hz. In comparison, the downstream moving part of the cycle ($0.5 < t/T < 1.0$) is distinctively different. Only a trace of the TS-peak can be distinguished and the peak occurs at a lower frequency, $f = 630$ Hz. The vanishing TS-peak in the spectra during the downstream moving part of the cycle was also observed for the high frequency case 2 of Studer *et al.* (2006). Studer *et al.* (2006) report an even stronger trend than in the current measurements, with a complete absence of a TS-peak for the downstream moving part of the cycle. The stronger trend seen by Studer *et al.* (2006) is a result of their higher level of unsteadiness, compared to the current measurements, see the introduction to Chap. 6. The present shift in the frequency of the two TS-peaks can be seen in the wavelet spectra of the low frequency case 1 in Studer *et al.* (2006).

Studer *et al.* (2006) interpret the absence of a TS-peak in the downstream moving part of the cycle as an indication of a convective transition mode, where the transition front is the edge of a region with already turbulent boundary layer that is convected downstream. The small TS-peak at $t/T \approx 0.68$ in the current measurements is taken as an indication that a fully convective transition front is not present. A further indication is the velocity of the transition front that is discussed in Sect. 6.2.

However, even though the transition is "creative" during the whole inflow oscillation cycle, clearly unsteady effects are seen in Fig. 6.1 and 6.2b. As shown by Ohno *et al.* (2022), the asymmetry between the upstream and downstream movement of the transition occurs also for cases that are not unsteady enough for the fully convective transition mode to form. In the case of a TS-driven, creative transition scenario, a disturbance wave in the boundary layer travels downstream with the phase velocity u_{ph}. Along the way, it undergoes TS-amplification and once high enough amplitude is reached, non-linear effects take over and transition occurs. The amplification along the wave's trajectory depends on the pressure gradient, which in turn is a function of the airfoil shape and the inflow angle. In addition, the viscous delay of the boundary layer effects the amplification, see Ohno (2023). In the steady case, the conventional stability diagram, as exemplified by Fig. 3.7a, describes the amplification of the 2D, primary TS-waves. In the unsteady case, the angle of inflow, and thereby the amplification characteristics, change in both space and time as the TS-wave travels downstream. Therefore, the spectrum of amplified disturbances is not only a function of the instantaneous inflow angle, but the related history of pressure gradient and viscous delay that the disturbances have experienced during their travel downstream.

In the following sections, a trajectory-following LST method is used to compare the experimental results with theory, see Sect. 2.6.2 and Ohno *et al.* (2023). The merits of the 2D trajectory-following LST used here, where the base-flow is based on URANS simulations with vertical, sinusoidal gusts modeled with the DVA approach, can be seen in Fig. 6.4. The n-factors are plotted for sinusoidal gusts with the zero-to-peak amplitude $v'/U_\infty = 0.01$ in Fig. 6.4a and $v'/U_\infty = 0.02$ in Fig. 6.4b. See Sect. 6.2 for a discussion about the matching of gust amplitudes between the experiment and the simulations. The experimental $x_{tr}(t)$ and the curves of constant n-factors calculated with the unsteady LST are not expected to match perfectly because of two main factors. First, the experiment shows a slightly different behavior of $x_{tr}(\alpha_{main})$ in the range of interest, see Fig. 3.6a. This causes the upstream turning point of the transition movement (at α_{min}) to be sharper than the more rounded downstream turning point (at α_{max}). The LST does not capture this slight non-linear behavior of $x_{tr}(\alpha_{main})$, but shows a more linear relation between α_{main} and x_{tr}. Second, the gust generator efficiency decreases close to α_{max}, thus limiting the downstream travel of the transition in the experiment to some degree. In contrast, the gust in the URANS, used to determine the base flow for the unsteady LST, is fully sinusoidal.

Taking these differences into account, the $\kappa = 1.0$ case seen in Fig. 6.4b exhibits a close correspondence between the measurement and the $n = 12$ curve of the unsteady LST in both the range of transition movement and the shape of the $x_{tr}(t)$ path. A reasonable match is found also at $\kappa = 1.4$ (not shown here).

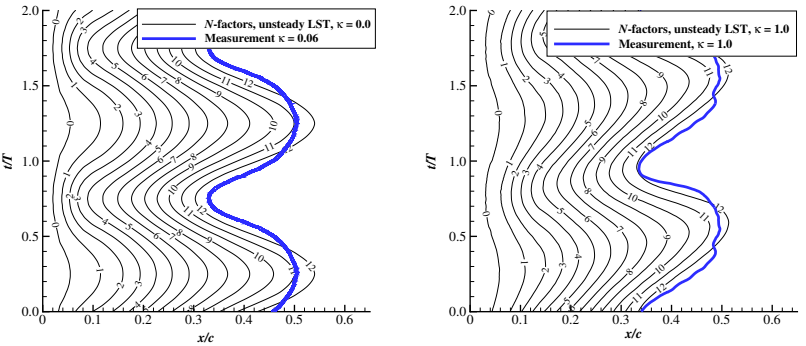

(a) Measurement at $\kappa = 0.06$, LST at $\kappa = 0.0$ and $v'/U_\infty = 0.01$.

(b) Both measurement and LST at $\kappa = 1.0$, LST at $v'/U_\infty = 0.02$.

Figure 6.4.: Measured transition location as function of t/T compared with n-factors from unsteady LST.

A similar pattern is seen for $\kappa = 0.06$ in Fig. 6.4a. However, at this low κ the range of transition movement is smaller in the experiment than the unsteady LST, despite the gust amplitude in the LST being $v'/U_\infty = 0.01$ compared to 0.02 in Fig. 6.4b. This stems from the trend of increasing range of the transition movement toward smaller κ in the LST, from which the experiment deviates for $\kappa < 0.7$, see Sect. 6.2 for more details.

From the results presented in this section, it is clear that the present measurements were conducted in an intermediate region of unsteady boundary layer response. The case $\kappa = 0.06$ is close to the steady case. However, increasing the oscillating frequency up to $\kappa = 1.7$ results in significant unsteady effects in the boundary layer response. Still, the unsteadiness does not reach a level where a convective transition mode is present, see Obremski & Fejer (1967) as well as Studer *et al.* (2006). In this intermediate region of unsteadiness, the boundary layer is clearly influenced by the unsteady inflow, but the effects can still be captured by linear stability theory. Transition prediction methods like the e^n method works surprisingly well in this intermediate region, provided that the integration of the n-factors are performed along the TS-wave trajectories. This enables the use of more or less existing transition prediction methods for a new and rather wide range of unsteady flow cases. Although the presence of the intermediate region may seem obvious, it has not been clearly described in previous literature.

6.2. Range and velocity of the transition front movement

One possibility to quantify the changes in the x_{tr}-movement with increasing κ is to determine the extremes of the movement and representative velocities of the transition front in the up- and downstream directions. However, the $x_{tr}(t)$ curves determined through the M-TERA method contain high-frequency disturbances that influence the determination of extreme points and transition front velocities. To reduce the influence of these disturbances, the $x_{tr}(t)$ curves are low-pass filtered digitally. A Butterworth filter with an effective order of 10 is applied using the "filtfilt" function in Matlab 2015b. This algorithm does not introduce a phase shift to the filtered signal. The corner frequency of the filter is set to $10 \cdot f_{gen}$, except for $\kappa = 0.06$ where $40 \cdot f_{gen}$ is used. Figure 6.6a shows the unfiltered and filtered $x_{tr}(t)$ for $\kappa = 1$ ($f_{gen} = 9$ Hz).

As seen in Fig. 6.1 and 6.4, the range of the transition movement changes with κ. Figure 6.5 summarizes the minimum and maximum of $x_{tr}(t)$ during the inflow oscillation, i.e. $x_{tr}(\alpha_{min})$ and $x_{tr}(\alpha_{max})$ respectively. For $0 \lesssim \kappa \lesssim 0.5$, the range of the transition movement increases slightly with increasing κ. This is an effect of the inflow angle induced by the gust generator falling off toward $\kappa = 0$, see Fig. 3.4. Above $\kappa = 0.5$, the range of transition movement

decreases with increasing κ. The upstream turning point (at α_{min}) is the one more effected by increasing κ. Here, $x_{tr}(\alpha_{min})$increases from 0.319 to 0.351 in the range $0.7 \leqslant \kappa \leqslant 1.4$. In the same range of κ, the downstream turning point (at α_{max}) moves upstream from 0.505 to 0.486, a change smaller by a factor of 0.6.

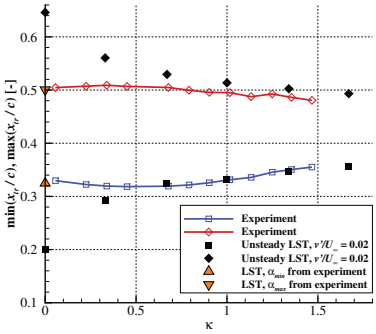

Figure 6.5.: The downstream and upstream extremes of the transition location, $\min(x_{tr}(t))$ and $\max(x_{tr}(t))$ respectively, as function of κ. $n_{crit} = 12$ is used as transition criterion in both the steady and the unsteady LST.

Figure 6.5 includes the transition locations from the unsteady LST with a gust amplitude of $v'/U_\infty = 0.02$ zero-to-peak. This amplitude is chosen to match the range of transition movement in the experiment at $\kappa = 1.0$. For $\kappa \geqslant 0.7$, the measured $x_{tr}(\alpha_{min})$ compares very well with the unsteady LST. The measured $x_{tr}(\alpha_{max})$ is slightly upstream of the unsteady LST, which can be attributed to the reduced efficiency of the gust generator around α_{min} (Fig. 3.6a), and slight differences in $x_{tr}(\alpha_{main})$ between the experiment and the LST. Below $\kappa = 0.7$ the unsteady LST shows a progressively increasing range of transition movement toward $\kappa = 0$, as opposed to the experiments that show a slight decrease. Compensating for the frequency dependent amplitude of the inflow angle, induced by the gust generator, reduces the differences somewhat (not shown here), but the general trend remains. The change in x_{tr}-range with κ of the LST results corresponds well to the predicted change in lift coefficient in the Sears theory for sinusoidal gusts (Sears, 1941). The large differences in x_{tr} seen at $\kappa = 0$ between the experiment and the unsteady LST with $v'/U_\infty = 0.02$ are due to the matching of x_{tr} amplitudes at $\kappa = 1$. If the α_{min} and α_{max} at $\kappa = 0$ from the measurements are used in the LST, the x_{tr} match the experiment well also at this reduced frequency, as seen in Fig. 6.5.

This means that for the range $\kappa < 0.7$, increased inflow angle oscillation

frequency do not produce as quick drop off in x_{tr}-range in the experiment as it does in the LST and the Sears theory. It is unclear if this observation is linked to unsteady effects of the boundary layer response or to the test setup.

Higher κ not only changes the range of the transition movement, but also the shape of the x_{tr} path, as seen in Fig. 6.2. Compared to the corresponding quasi-steady time-trace, the upstream moving transition front is faster and the downstream moving front slower. To quantify this change, the velocity of the transition front is determined by linear fits to $x_{tr}(t)$ between 15% and 60% of the range of $x_{tr}(t)$, see Fig. 6.6a. The gradients of the linear fits correspond to the upstream and downstream transition front velocities, $u_{tr,u}$ and $u_{tr,d}$ respectively. For comparison, the same analysis is performed on the steady and the unsteady $x_{tr}(t)$, compare Fig. 6.2. It should be noted that for some combinations of α_{main} and Tu analyzed in Chap. 6 and 7, the shape of the x_{tr} time-traces contain significant high-frequency components at high κ, even after the digital low-pass filtering. The proposed linear fitting method is not well suited for these time-traces and such cases are excluded from the analysis of $u_{tr,u}$ and $u_{tr,d}$.

Figure 6.6b summarises the transition front velocities with respect to κ. In the range $0.06 < \kappa < 0.7$ the increasingly "skewed" x_{tr} paths manifest themselves by a gradual departure of the unsteady $u_{tr,u}/U_\infty$ and $u_{tr,d}/U_\infty$ from their steady counterparts. Above $\kappa \approx 0.7$, the unsteady $u_{tr,u}$ and $u_{tr,d}$ gradually flattens out to essentially constant values of $u_{tr,u}/U_\infty = 0.35$ and $u_{tr,d}/U_\infty = 0.15$.

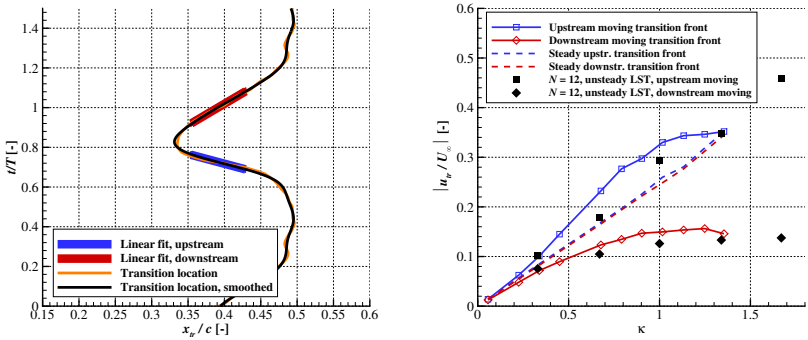

(a) The determination of the transition front velocities exemplified by $\kappa = 1.0$.

(b) The transition front velocity as function of κ.

Figure 6.6.: Velocity of the transition front.

The upper limit of $u_{tr,d}/U_\infty = 0.15$ is significantly lower than in the mea-

surements of Obremski & Fejer (1967) and of Studer *et al.* (2006). In an adverse pressure gradient, Studer et al. found the velocity of the downstream moving transition front of their case 2 to be $0.4{\cdot}U_\infty$. In a case with zero pressure gradient, Obremski & Fejer (1967) measured transition fronts moving downstream at 0.55, 0.57 and 0.64 times U_∞ at boundary layer heights where $\bar{u}/U_\infty = 0.5$, 0.7 and 0.9 respectively. For the upstream moving transition front, neither Obremski & Fejer (1967) nor Studer *et al.* (2006) report an upper limit for the velocity. In contrast, Obremski & Fejer (1967) show cases with formation of isolated turbulent spots where the transition location "jumps" to an upstream location and does not exhibit a continuous movement.

The unsteady LST generally show slightly lower values for $u_{tr,u}/U_\infty$ and $u_{tr,d}/U_\infty$ than the experiment, see Fig. 6.6. This is expected, since the more sinusoidal x_{tr} movement of the unsteady LST inherently results in lower transition front velocities. The velocity of the downstream moving transition front of the unsteady LST approaches a similar limit value towards high κ, as in the experiment. However, the LST shows $u_{tr,u}/U_\infty$ increasing with κ well beyond the measured range of κ.

In the case of a convective transition mode, the downstream moving transition fronts have similarities to the boundaries of a turbulent spot (Obremski & Fejer, 1967). A compilation of several published measurements on the development of turbulent spots is available in Gostelow *et al.* (1996). Even though those measurements are made in steady conditions, they allow a qualitative assessment of the results obtained in the present experiment. At a pressure gradient similar to the current measurements, Gostelow *et al.* (1996) estimate a trailing edge velocity of a turbulent spot moving at $u_{tr,d}/U_\infty = 0.34{\cdot}U_\infty$. This is faster by a factor of two compared to the current measurements, but somewhat slower than observed by Obremski & Fejer (1967) as well as by Studer *et al.* (2006). This is an indication that the transition in the present experiments is not driven by a convective transition mode. However, the scatter of the data in Gostelow *et al.* (1996) is considerable. According to Gostelow *et al.* (1996), the scatter comes, in part, from the different techniques and indicators used for determining the velocities in the different data sources.

It should be noted that two separate measurements campaigns with oscillating inflow angle were conducted within the frame of this thesis, a first in 2017 and a second with an improved experimental setup in 2020. The data presented in Chap. 6 and 7 are from the 2020 campaign. For the downstream moving transition front, the trends in the two campaigns agree well, but for the upstream moving front the trends are slightly different. Results from the 2017 measurements were published in Romblad *et al.* (2020), where some trends and conclusions do not fully match those in this thesis.

6.3. Amplification rates

To gain a better understanding of the stability characteristics of the boundary layer under the influence of inflow angle oscillations, it is helpful to analyze how the amplification rate, or n-factor (Sect. 2.6.1), changes over the oscillation cycle.

The n-factors of the cases with oscillating inflow angle are based on the cycle-averaged wavelet spectra. For each time-instance of the oscillation, the amplitudes of the wavelet spectrum for each pressure tap is converted from pressure fluctuations to u'_{max} as outlined in Sect. 2.6.5. The TS-frequency f_{TS} is determined from the spectrum of the x/c station with the highest peak amplitude and averaged disturbance amplitudes are calculated by integrating u'_{max} in the frequency range $0.95 \cdot f_{TS} < f < 1.05 \cdot f_{TS}$. Subsequently, n-factors are determined according to Eq. 2.10. The procedure is repeated for each time step in the cycle, thus capturing the variation of f_{TS} over the oscillation cycle. The initial amplitude A_0 is chosen to match the n-factor levels of the steady experiment and the LST calculations at f_{TS} and $x/c = 0.429$.

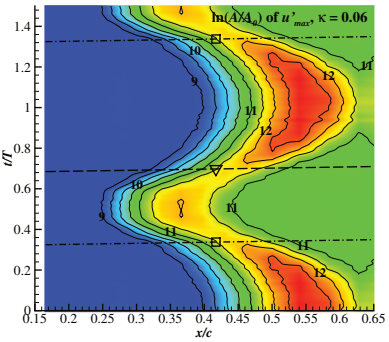

(a) n-factors as function of t/T. The instances with intermediate transition location $x_{tr,mid} = 0.5 \cdot (x_{tr}(\alpha_{max}) + x_{tr}(\alpha_{min}))$ are marked with squares for the upstream and triangles for the downstream moving part of the cycle. The TS-wave trajectories are indicated by dash-dotted and dashed lines respectively.

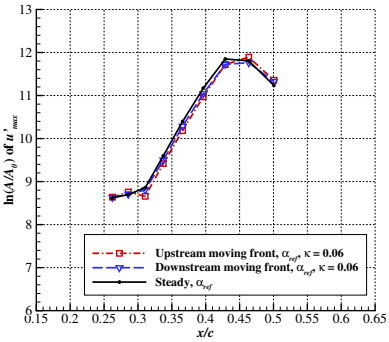

(b) Averaged n-factors along the TS-wave trajectories compared with the steady case.

Figure 6.7.: Averaged n-factors, $ln(A/A_0)$ of u'_{max} for $\kappa = 0.06$.

Figure 6.7a depicts the development of the n-factors of the case $\kappa = 0.06$ for an inflow angle cycle. The lower level of the plot is truncated just above

the noise floor of the measurement, at $n = 8.8$. As expected from the steady case, the increase of the n-factors in the x-direction is slightly faster at the most upstream transition location (α_{min}) than the most downstream one (α_{max}). Similar to the p_{rms} of Fig. 6.1, the n-factors exhibit a high level of symmetry between the part of the cycle with upstream moving transition front ($0 < t/T < 0.5$) and downstream moving front ($0.5 < t/T < 1$).

In Fig. 6.7a, the instances at which the transition is half way between its extremes, $x_{tr,mid} = 0.5 \cdot (x_{tr}(\alpha_{max}) + x_{tr}(\alpha_{min})) = 0.417$ are indicated. A square denotes the part of the cycle with upstream moving transition, $x_{tr,mid,up}$ and a triangle denotes the downstream moving one, $x_{tr,mid,down}$. By assuming a phase velocity of $u_{ph} = 0.35 \cdot U_\infty$ (based on LST results) the trajectories of the TS waves through $x_{tr,mid,up}$ and $x_{tr,mid,down}$ are calculated and plotted with dash-dot and dashed lines respectively. The n-factors along these two trajectories are plotted in Fig. 6.7b. For comparison, the steady n-factor curve derived from measurements with stationary α_{gen} is included.

At this low κ, the trajectories of the TS-waves are approximately horizontal in Fig. 6.7a, indicating that the conditions are close to steady. Consequently, the three n-factor curves of Fig. 6.7b are practically identical. The amplification region can be clearly discerned in the range $0.311 \leqslant x/c \leqslant 0.429$. The peak and drop-off for $x/c > 0.429$ are results of the transition to turbulent boundary layer. The nearly constant n-factor level for $x/c < 0.311$ indicates the noise floor of the measurement.

In the unsteady case $\kappa = 1.0$, the spatial and temporal development of the n-factors seen in Fig. 6.8a change character in a way similar to the p_{rms} of Fig. 6.1d. The region with disturbance amplification moves faster upstream than downstream and the peak of the instantaneous $n(x)$ is significantly lower in the latter part of the cycle than the former. At this higher κ, the trajectories of the TS-waves are more inclined in the spatial-temporal plot of Fig. 6.8a than those at $\kappa = 0.06$ in Fig. 6.7a. This has a strong effect on the n-factors along the respective trajectory, as depicted in Fig. 6.8b. In the case of upstream moving transition, the n-factors rise above the background noise later than in the steady case, but the level increases faster. This indicates a higher amplification in the range $0.366 \leqslant x/c \leqslant 0.429$ compared to the steady case. In the case of downstream moving transition, Fig. 6.8b shows that the n-factors increase earlier than in the steady case. The rate of amplification is initially similar to the steady case, but for $x/c \geqslant 0.337$ the n-factors gradually levels off to a broad peak at $x/c = 0.429$.

The unsteady LST shows that the primary instability point of the trajectory through $x_{tr,mid,up} = 0.413$ is slightly further downstream compared to the trajectory through the point $x_{tr,mid,down}$. For $x/c \lesssim 0.15$, the amplification along the trajectory through $x_{tr,mid,up}$ is lower than for the one through $x_{tr,mid,down}$, as opposed to $x/c \gtrsim 0.15$ for which the relation is reversed. This explains the differences in the n-factor curves of Fig. 6.8b.

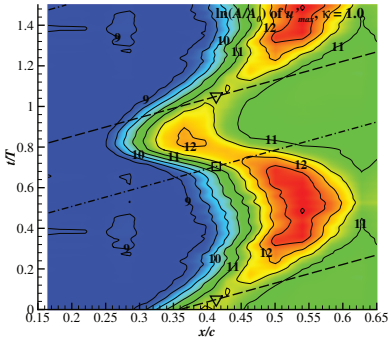

(a) n-factors as function of t/T. The instances with intermediate transition location $x_{tr,mid} = 0.5 \cdot (x_{tr}(\alpha_{max}) + x_{tr}(\alpha_{min}))$ are marked with squares for the upstream and triangles for the downstream moving part of the cycle. The TS-wave trajectories are indicated by dash-dotted and dashed lines respectively.

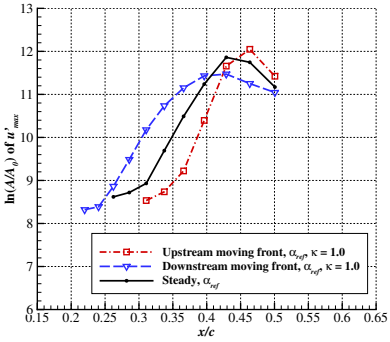

(b) Averaged n-factors along the TS-wave trajectories compared with the steady case.

Figure 6.8.: Averaged amplification ratios $ln(A/A_0)$ of u'_{max} for $\kappa = 1.0$.

Measurement data for amplification rates in oscillating flow are sparse in the literature. Studer *et al.* (2006) present amplification rates for the upstream moving part of the cycle for the high frequency case 2, but neither for the downstream moving, nor for a representative steady case. No further data has been found in the literature with which to compare the measured unsteady amplification rates across the oscillation cycle.

6.4. Comparison with DNS

Even though the unsteady LST has proven impressively accurate for the flow case studied here, its applicability is limited to the linear stage of the disturbance amplification. To complement the unsteady LST, direct numerical simulations have been performed and are compared to the experiment in the following section. The DNS results shown here have been conducted for the case $\kappa = 1.0$ and $v'/U_\infty = 0.02$ in the range $0.13 < x/c < 0.70$ on the pressure side of the airfoil. The analyzed region is $0.148 < x/c < 0.671$.

The simulations use a revised version of the high-order in-house DNS code NS3D (Babucke, 2009). URANS simulations with the DVA gust modelling provides the time dependent boundary conditions and base flow (Sect. 2.6.2). In order to provide controlled disturbances in the boundary layer, TS-waves

with $\omega = 201$ (corresponding to $f \approx 900$ Hz) are introduced by a disturbance strip at $x/c = 0.15$. A fundamental resonance case is used, consisting of both a 2D mode ($\beta = 0$ m^{-1}) and 3D modes ($\beta = \pm 333$ m^{-1} , or $\approx \pm 40°$) which are generated with amplitudes $v'/U_\infty = 5 \cdot 10^{-6}$ and $0.25 \cdot 10^{-6}$ respectively. See Ohno (2023) for further details on the numerical setup. The DNS results were kindly provided by Duncan Ohno.

Figure 6.9 shows the temporal variations of the surface pressure fluctuations extracted for $\omega = 201$ ($f \approx 900$ Hz), by means of the CWT, from the experiment and the DNS. Note that the so-called L^1 normalization (Farge, 1992) is used in the CWT for both the experimental data and the DNS. According to Farge (1992), the L^1 normalization is better suited for tracking the amplitude of single frequency signals than the L^2 normalization, see also Sect. 2.6.5. The results are plotted together with the n-factor curves from the unsteady LST for the same frequency. The LST and DNS in Fig. 6.9b are both depicted at the same phase shift relative to the external gust. The experimental data in Fig. 6.9a are manually shifted in time to approximately match the phase of the $n = 10$ curve of the LST.

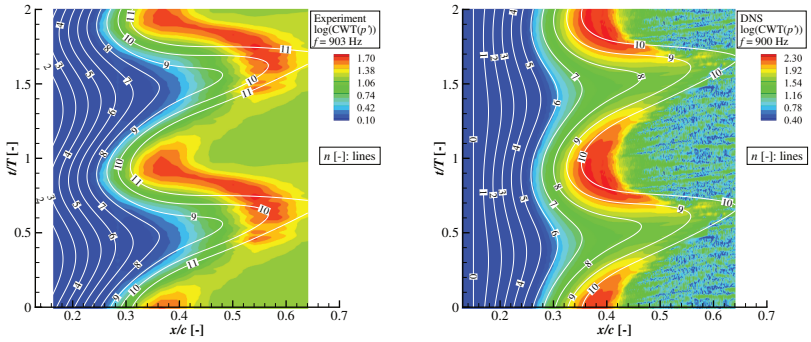

(a) Measurement and LST with moving instability point.

(b) DNS, TS waves with $f_{TS} \approx 900$ Hz introduced at $x/c = 0.15$ and LST with integration started at $x/c = 0.15$.

Figure 6.9.: Narrow band surface pressure fluctuations at $\omega = 201$ ($f \approx 900$ Hz), for $\kappa = 1.0$. L^1 normalization is used for the CWT.

The use of the disturbance strip in the DNS locks the start of the TS-waves (the effective instability point) to a fixed chordwise location, see the $n = 0$ line in Fig. 6.9b. In contrast, the primary instability point in the experiment depends on both the inflow angle and the frequency of the TS-disturbance. This results in larger variations in both surface pressures and

n-factors over the oscillation in the experiment compared to the DNS, making a direct comparison between the two difficult. Here, comparisons with the unsteady LST is used as a bridge between the two cases.

During the inflow angle oscillation, the overall spatial-temporal behavior of the narrowband CWT(p') in the experiment (Fig. 6.9a) resembles those of the broadband p_{rms} of Fig. 6.1d. The regions of high amplitude for the $f \approx 900$ Hz disturbances are shifted slightly upstream compared to the broadband ones, a consequence of lower frequencies being the more amplified at the more downstream stations. In both the narrowband and the broadband plots, the highest TS-peaks are found in the part of the oscillation cycle when the transition is moving upstream. The curves of constant n-factors from the unsteady LST exhibit a fair agreement with the measured CWT(p'), apart from the region with the most downstream transition location, i.e. $0.4 < t/T < 0.7$. In this region, the experiment shows a significantly faster growth of disturbances, probably caused by non-linear effects not captured by the LST. Transition occurs for n-factors in the order of 11 to 12.

Comparing the LST results in Fig. 6.9a with Fig. 6.9b reveals the effect of the free vs. fixed primary instability point. With the instability point free, the TS waves start growing further upstream than with the fixed instability point. As a result, the case with free instability point exhibits higher n-factor levels and larger variations across the oscillation cycle compared to the case with fixed instability point. This also affects the levels of the p' fluctuations, and the plotting scales had to be adjusted differently in Fig. 6.9a and Fig. 6.9b. In addition, differences in the spanwise wavenumber content contributes to the differences observed between experiment and DNS.

The CWT(p') from the DNS compares well with the curves of constant n-factors from the unsteady LST. Transition occurs for n-factors in the order of 9 to 10. The reduction in amplitude of the TS-peak in the part of the oscillation cycle with downstream moving transition seen in the experiment is also present in the DNS results for $0.3 < t/T < 0.5$. In contrast to the experiment, the region without clear TS-peak in the DNS extends into the part of the cycle with upstream moving transition, $0.5 < t/T < 0.7$. This may be linked to non-linear interactions between TS-modes with different frequencies in the experiment, effects that are not fully present in the DNS where a single 2D TS-mode and its $\approx \pm 40^\circ$ counterparts are excited.

Further analysis of the DNS results (Ohno, 2023) suggest that the interface between the downstream moving turbulent region and the laminar boundary layer contributes to the reduction in the TS-peak present at $0.3 < t/T < 0.5$. In the vicinity of this interface region, a small relaxation of the mean boundary layer velocity profile stabilizes the boundary layer (Gostelow *et al.*, 1997). This can be seen as a pre-stage to the calmed region that is common the boundary layer transition found in turbomachinery and is described by e.g. (Gostelow *et al.*, 1997). Ohno (2023) shows that the calming effect

behind a downstream moving transition front is gradual and not confined to the calmed region. This indicates that, even though the low velocity of the downstream moving transition front in the current experiment does not produce a fully developed calmed region, the mentioned stabilization of the boundary layer and the presence of a "weak calmed region" is possible.

6.5. Conclusions - the influence of large-scale turbulence

Chapter 6 shows measurement results for the case $\alpha = \alpha_{ref}$ and $Tu_u^x = 0.02\%$ with oscillating inflow angle. With increasing frequency of the oscillating inflow, the temporal variations of p_{rms}, the transition location and the n-factors gradually depart from their quasi-steady behavior. The region of TS amplification, and subsequent transition, moves faster upstream and slower downstream than in the steady case. In addition, the peak in the p_{rms} distribution is significantly lower as the transition moves downstream compared to the upstream moving part of the cycle.

For the unsteady LST, a gust amplitude of $v'/U_\infty = 0.02$ is chosen to match the measured range of $x_{tr}(t)$ at $\kappa = 1.0$. In the range $0.7 < \kappa < 1.4$, this results in a good correspondence between the time-traces of the measured $x_{tr}(t)$ and $n = 12$ of the trajectory-following LST method.

For $\kappa \gtrsim 0.5$, the measured range of transition movement decreases with increasing κ, the downstream extreme changing less than the upstream by a factor of 0.6. The trend of the range of the transition movement matches well with the unsteady LST in this range of κ. For $\kappa \lesssim 0.5$, the measured range of transition movement decrease slightly toward smaller κ. In contrast, the trajectory-following LST show a significantly increased range for the same oscillating frequencies. Compensating for the frequency dependent amplitude of the inflow angle from the gust generator reduces the differences somewhat (not shown here), but the general trend remains. The κ-dependency of the x_{tr}-range in the LST results correspond well to that of the lift coefficient in the Sears theory for sinusoidal gusts (Sears, 1941). LST calculations at the measured α_{min} and α_{max} for $\kappa = 0$ match the x_{tr} of the experiment well. It is not clear why the airfoil response to inflow angle oscillations does not drop off as quickly with increasing κ in the experiment as it does in the URANS-based LST and the Sears theory. Apart from the difference in range, the shapes of the $x_{tr}(t)$ and the curves of constant n-factor of the LST show a fair resemblance also for $\kappa < 0.7$.

The velocity of the upstream and downstream moving transition front increases approximately linear with κ up to $\kappa \approx 0.7$. For $\kappa > 0.7$, the increase of both velocities gradually slows down and a maximum appears to be reached for $\kappa \approx 1.4$ where $u_{tr,u}/U_\infty = 0.35$ and $u_{tr,d}/U_\infty = 0.15$. Studer *et al.* (2006) found a higher $u_{tr,d}/U_\infty$ of 0.4 for the downstream moving front but no upper

limit for $u_{tr,u}/U_\infty$. The trajectory-following LST at $n = 12$ show a similar trend as the current measurements for the downstream moving transition front, but no maximum is indicated for the velocity of the upstream moving transition front, in the range of the measurements.

Assuming that the phase velocity of the TS waves is approximately constant with respect to κ, increasing κ causes the TS waves to see progressively more variation in the base flow and stability characteristics during their travel from the instability point to the transition. The result can be seen in the measured amplification rates. For TS-trajectories through the respective mid-points of the transition movement, $x_{tr,mid,up}$ and $x_{tr,mid,down}$, the growth of TS-waves for the upstream moving transition front occurs slightly further downstream than in the steady case, but the growth is faster. For the downstream moving transition front, the relation is essentially reversed and the maximum n-factor is lower. The unsteady LST shows the primary instability point of the trajectory through $x_{tr,mid,up}$ slightly further downstream than of the one through $x_{tr,mid,down}$. The $x_{tr,mid,up}$-trajectory has a lower amplification upstream $x/c \approx 0.15$ and a higher downstream of this station, according to the LST.

The CWT(p') at 900 Hz from DNS at $\kappa = 1.0$ exhibit a good correspondence with the curves of constant n-factor from the unsteady LST. The region of transition with a significantly lower TS-peak, that occurs when the transition moves downstream in the experiment, extends into the part of the oscillation in which the transition moves upstream. This may be an effect of the single-mode excitation in the DNS as opposed to the broadband disturbance spectrum of the experiment. However, a detailed comparison is difficult due to different nature of TS-excitation in the simulation and the experiment.

The current measurements were performed at inflow angle amplitudes and frequencies that are relevant for flight in the convective part of the turbulent atmosphere. In this range of inflow conditions, the results show that increasing κ causes a gradual shift from quasi-steady to clearly unsteady boundary layer response. However, the unsteadiness is not strong enough for convective transition modes to form. Up to now, this intermediate range of unsteady boundary layer flow has not been clearly described in the literature. In this intermediate range of unsteady flow, the main features of the unsteady boundary layer behaviour are well captured by trajectory-following LST, as shown by the current experiments. The applicability of trajectory-following LST in this range of unsteady boundary layer flow is a valuable conclusion in the framework for the design of future NLF airfoils.

7. The combined influence of small- and large-scale turbulence

In Chap. 5 and 6 above, the influence of small and large turbulence scales on the boundary layer transition are treated separately. However, in flight through the turbulent atmosphere, both small and large turbulence scales are present simultaneously. The following section focuses on the combined effect of small-scale turbulence and periodic inflow angle oscillations, the latter representing the large turbulence scales.

7.1. Measurement setup

The investigation is an extension of the measurements on the MW-166-39-44-43 airfoil described in Chap. 5 and 6 and much of the measurement setup was kept the same. However, the small-scale turbulence was generated using the passive grids $d6M42$ and $d16M100$ described in Sect. 2.2.1 instead of the active grid used for the measurements in Chap. 5. The main reason for using the passive grids was their superior repeatability with respect to the generated turbulence. In the primary frequency range of TS amplification, the spectra of the turbulence generated by the active and the passive grids are similar, see Fig. 3.2. Consequently, turbulence generated by the two grid types are expected to have the same influence on the boundary layer development, as long as the turbulence level is maintained.

The investigation is conducted at a slightly weaker adverse pressure gradient than in Chap. 5 and 6 to ensure that transition occurs in the instrumented range of the airfoil $0.166 \leqslant x/c \leqslant 0.727$, for all combinations of inflow angle and Tu. The desired pressure gradient was achieved by using an angle of attack of α_{main} = -0.2° = α_{ref} + 0.5°. This change in pressure gradient moves the steady transition location at $Tu_u^x = 0.02\%$ to $x/c = 0.521$, a case that serves as the baseline in the following section.

7.2. Unsteady surface pressures

Similar to Sect. 6.1, the cycle averaged short time rms of the wall pressures and M-TERA C_3 parameter provide an overview of the transition behavior throughout the inflow angle oscillation cycle. The transition criteria $C_3 = 1 \cdot 10^5$ is employed, and the lower end of the color maps of p_{rms} are truncated

just above the electronic noise floor (blue color).

7.2.1. Base flow at $Tu_u^x = 0.02\%$

Comparing the p_{rms} at $\alpha_{main} = \alpha_{ref} + 0.5^\circ$ and $Tu_u^x = 0.02\%$ depicted in Fig. 7.1 with the case at $\alpha_{main} = \alpha_{ref}$ in Fig. 6.1, the intended downstream shift of the average transition location at the less adverse pressure gradient is evident. The movement of the transition location during the inflow angle oscillation is more sinus-shaped than at $\alpha_{main} = \alpha_{ref}$, owing to the more linear $x_{tr}(\alpha_{main})$ curve in this range of inflow angles (see Fig. 3.6b). This results in lower maximum velocities of the transition movement for the case at $\alpha_{ref} + 0.5^\circ$compared to the case at α_{ref}.

Similar to $\alpha_{main} = \alpha_{ref}$, the p_{rms} of the quasi-steady $\kappa = 0.06$ at $\alpha_{main} = \alpha_{ref} + 0.5^\circ$ in Fig. 7.1a show a high degree of symmetry between the part of the inflow angle cycle where the transition moves upstream ($0.0 < t/T < 0.5$) and downstream ($0.5 < t/T < 1.0$). Up to $\kappa \approx 1.0$, increasing κ results in a gradual reduction of the rms peak in the part of the cycle where the transition moves downstream, whereas it increases slightly in the other half of the cycle. The progressively more skewed time histories of p_{rms} and C_3 with increasing κ seen at $\alpha_{main} = \alpha_{ref}$ manifest themselves also at the higher angle of attack, albeit mainly for the downstream moving transition front. At $\kappa = 1.3$, the initially sine-shape time-traces of the p_{rms} and C_3 have become significantly distorted. Increasing the frequency to $\kappa = 1.7$ results in time-traces that are strongly saw-tooth shaped, with reduced streamwise transition movements. At this κ, the upstream moving transition is much faster than the downstream moving one. Unfortunately, the behavior for $\kappa \geqslant 1.3$ is clearly influenced by a reduction in signal to noise ratio and is not fully representative for the unsteady boundary layer response.

7.2.2. Transition at medium levels of turbulence, $Tu_u^x = 0.06\%$

At $\alpha_{main} = \alpha_{ref} + 0.5^\circ$ and $Tu_u^x = 0.06\%$, the transition occurs in a region similar to the case $\alpha_{main} = \alpha_{ref}$ and $Tu_u^x = 0.02\%$, see Fig. 7.2 and 6.1 respectively. In the quasi-steady case $\kappa = 0.06$, the similarity between the two cases (Fig. 6.1a and Fig. 7.2a) is striking. The main differences are seen at the downstream turning point of the oscillation cycle, where time-traces for the higher Tu_u are less rounded and the peak in p_{rms} is not as pronounced as at the lower Tu_u.

The trend of increasingly skewed time traces of the p_{rms} and C_3 with increasing κ, as well as the diminishing peak in p_{rms} for the downstream moving transition, closely resemble the behavior seen at α_{ref}. However, the strong change in character of the time traces observed for $\kappa \geqslant 1.3$ at $Tu = 0.02\%$ at both α_{ref} and $\alpha_{ref} + 0.5^\circ$, is only present here at $\kappa = 1.7$.

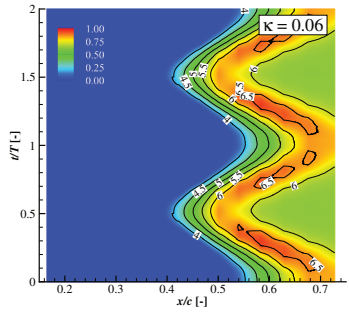

(a) $\kappa = 0.06$.

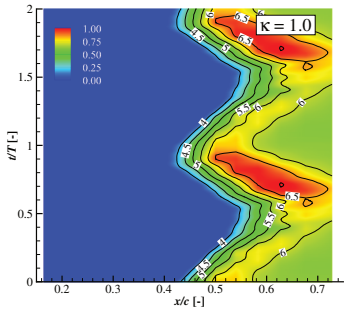

(d) $\kappa = 1.0$.

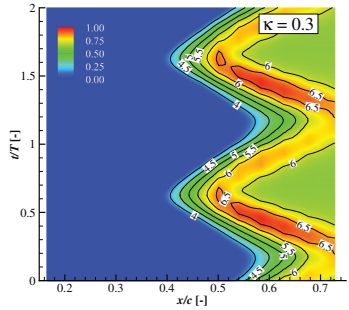

(b) $\kappa = 0.3$.

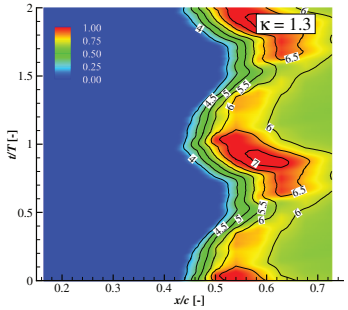

(e) $\kappa = 1.3$.

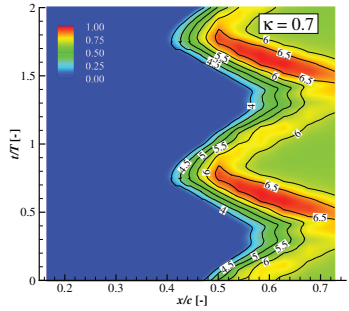

(c) $\kappa = 0.7$.

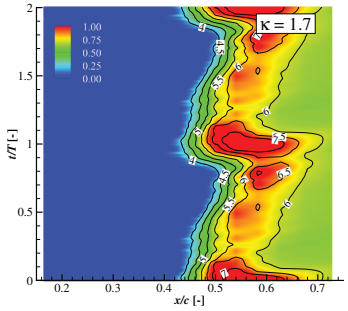

(f) $\kappa = 1.7$.

Figure 7.1.: In color, $log(p_{rms})$ at $\alpha_{main} = \alpha_{ref} + 0.5°$ and $Tu_u^x = 0.02\%$. As contours, the logarithm of the C_3 parameter of the M-TERA method.

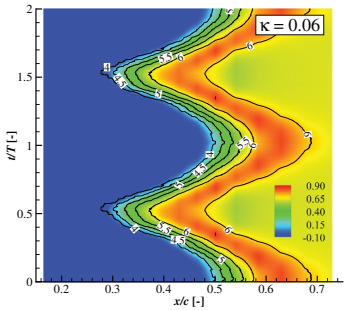

(a) $\kappa = 0.06$.

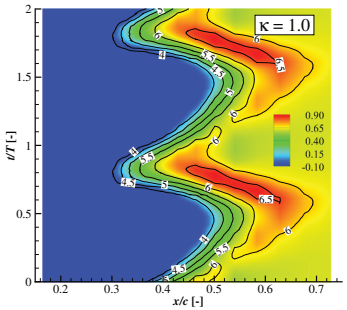

(d) $\kappa = 1.0$.

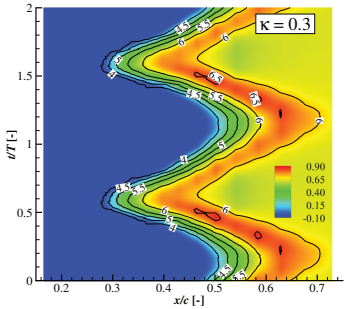

(b) $\kappa = 0.3$.

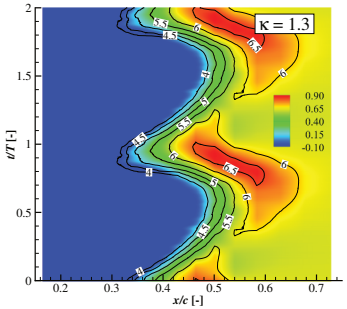

(e) $\kappa = 1.3$.

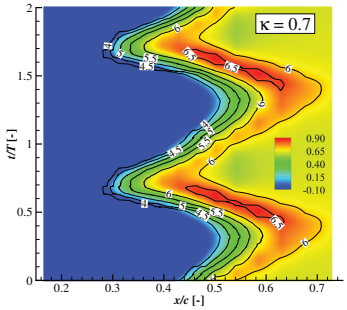

(c) $\kappa = 0.7$.

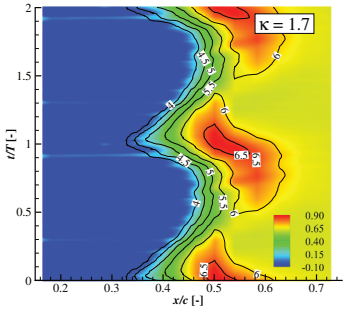

(f) $\kappa = 1.7$.

Figure 7.2.: In color, $log(p_{rms})$ at $\alpha_{main} = \alpha_{ref} + 0.5°$ and $Tu_u^x = 0.06\%$. As contours, the logarithm of the C_3 parameter of the M-TERA method.

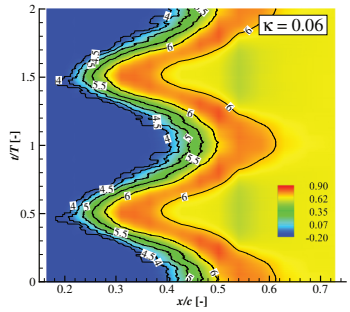

(a) $\kappa = 0.06$.

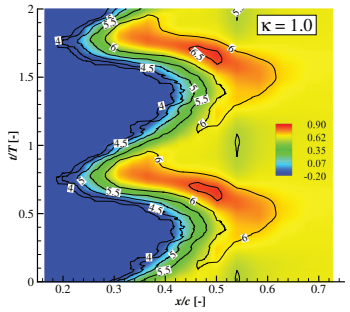

(d) $\kappa = 1.0$.

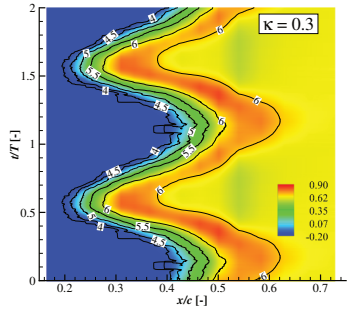

(b) $\kappa = 0.3$.

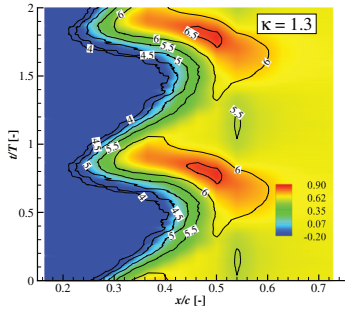

(e) $\kappa = 1.3$.

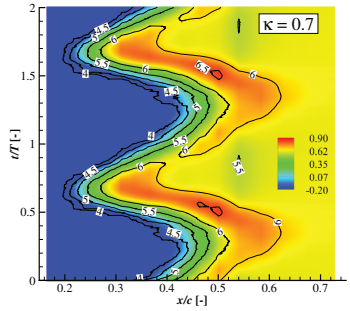

(c) $\kappa = 0.7$.

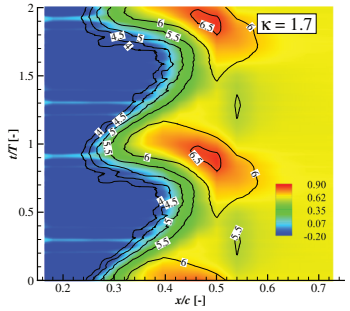

(f) $\kappa = 1.7$.

Figure 7.3.: In color, $log(p_{rms})$ at $\alpha_{main} = \alpha_{ref} + 0.5°$ and $Tu_u^x = 0.13\%$. As contours, the logarithm of the C_3 parameter of the M-TERA method.

7.2.3. Transition at higher levels of turbulence, $Tu_u^x = 0.13\%$

At $Tu_u^x = 0.13\%$, the transition region moves even further upstream, as seen in Fig. 7.3. The general pattern of p_{rms} and C_3 resembles the one at $Tu_u^x = 0.06\%$, with progressively more skewed time-traces toward higher κ. Similar to the cases with lower turbulence levels, the highest p_{rms} levels occur in the part of the oscillation cycle with upstream moving transition. However, the peak level is lower in the present case. Continuing the trend seen at $Tu_u^x = 0.06\%$, the general character of the p_{rms} and C_3 time traces are maintained to higher frequencies compared to previous cases with lower Tu. At $Tu_u^x = 0.13\%$, the shape is approximately preserved even at the highest frequency measured, $\kappa = 1.7$.

7.3. Unsteady transition location

The time-traces of the transition location in the quasi-steady cases at $\kappa = 0.06$ all exhibit a close resemblance to their respective steady counterparts at all Tu, see Fig. 7.4a. To facilitate comparisons, the steady curves for $Tu_u^x = 0.06\%$ in Fig. 7.4a and Fig. 7.4b are shifted upstream by $\Delta x/c = 0.018$. As observed in the plots of p_{rms} and C_3 parameter for the case $Tu_u^x = 0.06\%$, $x_{tr}(t)$ in the range $x/c \leqslant 0.46$ is very close to that of the case $\alpha_{main} = \alpha_{ref}$ at $Tu_u^x = 0.02\%$. In the vicinity of α_{max}, $(0.8 \leqslant t/T \leqslant 1.2)$ the transition location of the case $Tu_u^x = 0.06\%$ extends further downstream than the one at α_{ref}. This is expected from the steady $x_{tr}(\alpha_{gen})$ seen in Fig. 3.6a and 3.6c respectively.

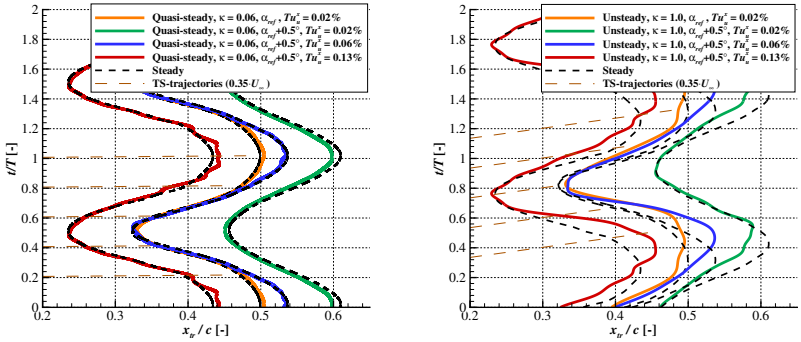

(a) $\kappa = 0.06$. (b) $\kappa = 1.0$.

Figure 7.4.: Steady and unsteady transition location as function of t/T.

At $\kappa = 1.0$, the now familiar skewed pattern of the plots of p_{rms} and C_3 in Fig. 6.1 and 7.1 to 7.3 carries over to the transition front $x_{tr}(t)$. The upstream turning points of the unsteady $x_{tr}(t)$ are all fairly close to the steady transition. At the downstream turning point, the unsteady case α_{ref} + 0.5° at $Tu_u^x = 0.02\%$ does not reach as far in the streamwise direction as the steady curve. In contrast, at $Tu_u^x = 0.13\%$ the downstream turning point is shifted further downstream than for the steady counterpart. A more detailed analysis is provided in the following sections.

7.4. Range and velocity of the transition front movement

As seen in Fig. 7.4, with increasing κ, the upstream moving transition front is faster than the steady case, the downstream moving front is slower, and the range of the transition movement decreases. This is the same trend as seen at α_{ref} in Sect. 6.2. In Fig. 7.5 the minimum and maximum of $x_{tr}(t)$ as well as the transition front velocities at α_{ref} + 0.5° are summarized for the three different Tu. The corresponding plots at α_{ref} can be found in Fig. 6.5 and 6.6.

For all three Tu, the range of the transition movement increases slightly with increasing κ up to $\kappa \approx 0.5 - 0.7$. At higher frequencies, the range decreases again. As described in Sect. 6.2, the decreasing range of $x_{tr}(t)$ toward higher κ corresponds to the trend for the lift coefficient in the Sears theory (Sears, 1941), which is closely related to the unsteady pressure distribution seen by the boundary layer. However, the experiment exhibits a smaller change for $\kappa \lesssim 0.7$, as already discussed in the cited section.

The velocities of the transition front for $Tu_u^x \geqslant 0.06\%$ at α_{ref} + 0.5° (Fig. 7.3d-f) exhibit close similarities to the reference case at α_{ref} and $Tu_u^x = 0.02\%$ plotted in Fig. 6.6b. With increasing κ, the upstream moving front becomes progressively faster than the steady case, and vice versa for the downstream moving front. The velocity of the downstream moving front $u_{tr,d}$, trends toward a limit value for high κ that is in the order of $u_{tr,d}/U_\infty = 0.18$, a level slightly higher than the $u_{tr,d}/U_\infty = 0.15$ seen at α_{ref} (Fig. 6.6b). In contrast to the case α_{ref}, no clear leveling-off is present in the velocity of the upstream moving front $u_{tr,u}$. The continuous increase of $u_{tr,u}$ is similar to the behavior seen in the unsteady LST.

Compared to the three combinations of α_{main} and Tu_u^x described above, the case α_{ref} + 0.5° at $Tu_u^x = 0.02\%$ exhibits atypical behavior of $u_{tr,u}$ and $u_{tr,d}$ as function of κ. Because of the smaller range of transition movement and the more sine-shaped $x_{tr}(t)$, the velocities of the transition fronts are lower. The upstream moving transition front moves progressively faster than the steady up to $\kappa = 0.7$, but for higher κ, $u_{tr,u}$ is slightly lower than the velocity of the steady transition front. At $\kappa = 1.2$, the downstream moving transition

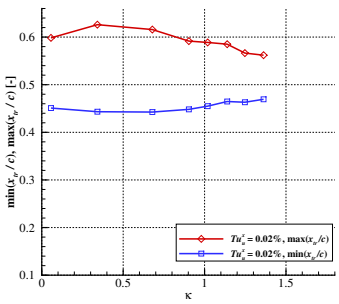

(a) Δx_{tr}, $Tu_u^x = 0.02\%$

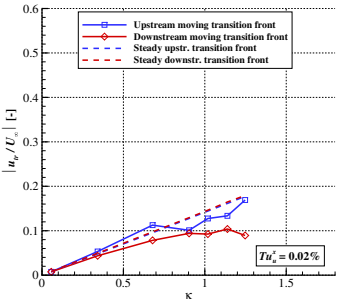

(d) Transition front vel., $Tu_u^x = 0.02\%$

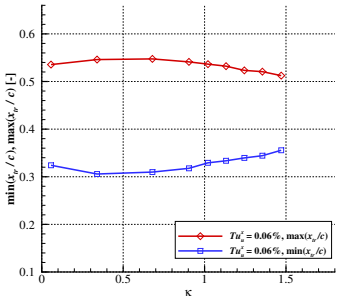

(b) Δx_{tr}, $Tu_u^x = 0.06\%$

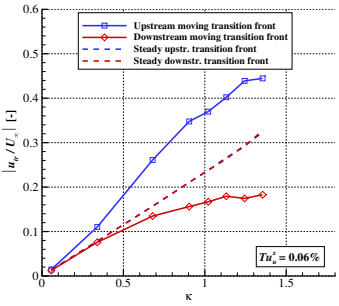

(e) Transition front vel., $Tu_u^x = 0.06\%$

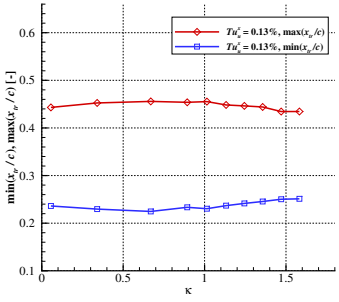

(c) Δx_{tr}, $Tu_u^x = 0.13\%$

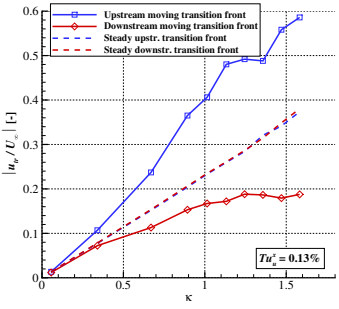

(f) Transition front vel., $Tu_u^x = 0.13\%$

Figure 7.5.: **a-c**) The most downstream and upstream transition location, $\min(x_{tr}(t))$ and $\max(x_{tr}(t))$ respectively, as function of κ and **d-f**) the transition front velocity as function of κ.

front moves at $u_{tr,d}/U_\infty = 0.09$. Although this $u_{tr,d}/U_\infty$ does not appear to represent a limit value, the increase with κ is small and an estimated limit value is lower than for the higher Tu_u. Above $\kappa = 1.2$, the employed method of determining $u_{tr,u}$ and $u_{tr,d}$ works poorly due to the distorted shape of $x_{tr}(t)$, and no transition front velocities are presented.

7.5. Amplification rates

The amplification rates at $\kappa = 1.0$ are analyzed for the three different Tu at $\alpha_{ref} + 0.5°$, using the same methodology as in Sect. 6.3. The reference case at α_{ref} with $Tu_u^x = 0.02\%$ (see Fig. 6.8) is used for comparisons.

With increasing Tu, the region with measurable amplification shifts upstream and the maximum n-factor decreases somewhat, see Fig. 7.6. Looking at TS-trajectories passing through the intermediate transition locations $x_{tr,mid,up}$ and $x_{tr,mid,down}$, the trajectory with upstream moving transition exhibits a higher peak than the downstream moving one (Fig. 7.6d-f). These are the same trends as seen at α_{ref}. The trajectory through $x_{tr,mid,up}$ at $Tu_u^x = 0.13\%$ is an exception, in that the peak n-factor level is similar to the one of the downstream moving transition, as seen in Fig. 7.6f. The reason for this behavior is discussed in connection to Fig. 7.7.

For the case at α_{ref}, the growth in n-factor for the upstream moving transition occurs further downstream than in the steady case, but at a faster rate, as seen in Fig. 6.8b. For the downstream moving transition the relation is reversed and the growth in n-factor gradually levels off to a broad peak. These characteristic features are present also at $\alpha_{ref} + 0.5°$, but at a much smaller scale. At $Tu_u^x = 0.02\%$ the difference between the two unsteady n-factor curves is barely discernible (Fig. 7.6d). With increasing Tu_u, the effect becomes larger, and at $Tu_u^x = 0.13\%$ it is approximately half as large as at α_{ref}, see Fig. 7.6f.

The n-factor curve for the upstream moving transition at $Tu_u^x = 0.13\%$ constitutes an exception, as seen in Fig. 7.6f. This trajectory passes through a region of relatively low n-factors around $0.36 \leqslant x/c \leqslant 0.42$ in the part of the cycle at $0.60 \leqslant t/T \leqslant 0.75$, see Fig. 7.6c. Consequently, the n-factors along the trajectory are correspondingly lower.

The lower amplification rates in this region are linked to how the frequency of the TS peak f_{TS}, evolves in the streamwise direction. The primary TS peak has a natural tendency to shift gradually toward lower frequencies in the downstream direction. This is clear from the stability diagram in Fig. 3.7a, which shows a higher amplification of lower frequencies further downstream. LST calculations on the MW-166-39-44-43 display a gradual change of the peak frequency in the range $0.2 \leqslant x/c \leqslant 0.7$. However, the experiment exhibits a slightly faster shift of the peak in the region $0.30 \lesssim x/c \lesssim 0.40$.

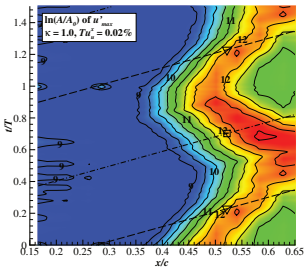

(a) $ln(A/A_0)(t)$ at $Tu_u^x = 0.02\%$

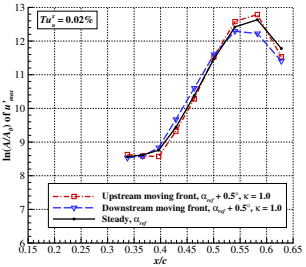

(d) $ln(A/A_0)(\kappa)$ at $Tu_u^x = 0.02\%$

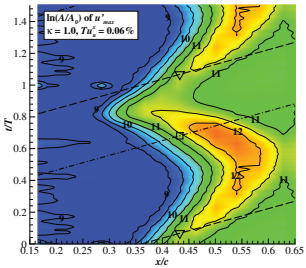

(b) $ln(A/A_0)(t)$ at $Tu_u^x = 0.06\%$

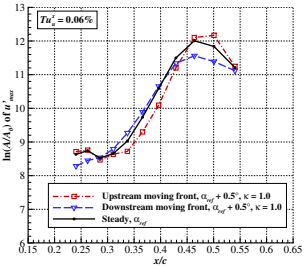

(e) $ln(A/A_0)(\kappa)$ at $Tu_u^x = 0.06\%$

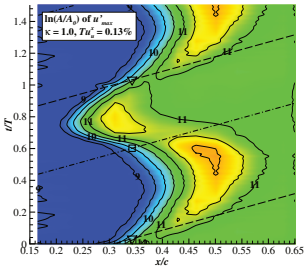

(c) $ln(A/A_0)(t)$ at $Tu_u^x = 0.13\%$

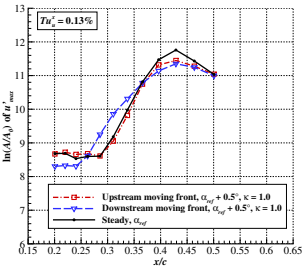

(f) $ln(A/A_0)(\kappa)$ at $Tu_u^x = 0.13\%$

Figure 7.6.: Averaged amplification ratios $ln(A/A_0)$ of u'_{max} for $\kappa = 1.0$ at Tu_u^x = 0.02%, 0.06% and 0.13%, **a-c**) as function of t/T. The instances with the intermediate transition location $x_{tr} = 0.5 \cdot (x_{tr}(\alpha_{max}) + x_{tr}(\alpha_{min}))$ are marked with squares for the upstream and triangles for the downstream moving part of the cycle. The TS-wave trajectories are indicated by dash-dotted and dashed lines respectively. **d-e**) Averaged amplification rates $ln(A/A_0)$ along the TS-wave trajectories compared with the steady case.

Figure 7.7 depicts spectra from surface pressures measured on the isolated main airfoil in steady conditions. Spectra from the wavelet analysis are used because the smoother spectra of the CWT makes the frequency of the TS peak easier to identify than in FFT spectra. At $Tu_u^x = 0.02\%$, the more rapid change in f_{TS} in the range $0.30 \lesssim x/c \lesssim 0.40$ is barely discernible (Fig. 7.7a), but at $Tu_u^x = 0.13\%$ (Fig. 7.7b) two distinct frequency regions of amplified disturbances are formed. The region with higher frequencies dominates close to the leading edge, but is "overtaken" by the region with lower frequencies at $x/c \approx 0.35$.

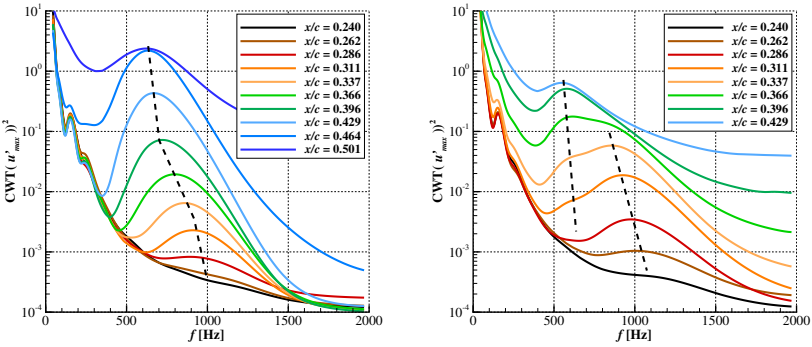

(a) $Tu_u^x = 0.02\%$, $\alpha = \alpha_{ref}$. (b) $Tu_u^x = 0.13\%$, $\alpha = \alpha_{ref} + 0.4°$.

Figure 7.7.: Spectra of unsteady surface pressures, from the CWT analysis. Isolated main airfoil.

Clearly, there is a different transition scenario involved that includes detuned subharmonic amplification (Borodulin *et al.*, 2002*a*,*c*,*b*; Kachanov, 1994). Here, the subharmonic amplification of modes can start early due to the "seeds" provided by the higher turbulence level. Those modes have higher amplification rates than the primary TS modes and thereby overtake the primary modes at a certain streamwise position. This defines the end of the "weakly non-linear stage" of transition and limits a further increase of primary modes (Würz *et al.*, 2012*a*).

As a result, in the $Tu_u^x = 0.13\%$ case, the frequency of the maximum peak shifts suddenly in the range $0.337 \leqslant x/c \leqslant 0.366$. This sudden shift influences the integration of the experimental n-factors that is performed in a range $\pm 5\%$ around the TS peak frequency. The region with lower n-factors in the upstream moving part of the cycle in Fig. 7.6c and 7.6f is a result of this shift in peak frequency.

Similar to Fig. 6.7, the peak frequency varies in a significantly smaller range

of frequencies for the downstream moving transition than for the upstream moving one. Consequently, the effect of the sudden shift in the peak frequency does not have a significant influence on the level of the n-factors for the downstream moving transition.

7.6. Conclusions - the combined influence of small- and large-scale turbulence

Chapter 7 describes the combined effect of small-scale turbulence and inflow angle oscillations on the boundary layer transition. The measurements were performed at $\alpha_{main} = \alpha_{ref} + 0.5°$ at $Tu_u^x = 0.02\%$, 0.06% and 0.13%. For these cases, the general trends with κ in the temporal variations of p_{rms}, the transition location and the amplification rates share the main characteristics with the case $\alpha = \alpha_{ref}$ at $Tu_u^x = 0.02\%$ discussed in Chap. 6. With higher frequency κ of the inflow oscillations, the region with disturbance amplification and the transition moves faster upstream and slower downstream compared to the steady case. The peak in the $p_{rms}(x)$-distribution is significantly lower when the transition moves downstream compared to upstream. The change to saw-tooth shaped time traces of p_{rms} and the C_3 parameter seen for $\kappa > 1.3$ in the case $\alpha_{main} = \alpha_{ref}$ (see Chap. 6) occurs at $\kappa = 1.7$ for $Tu_u^x = 0.06\%$. At the higher turbulence level of $Tu_u^x = 0.13\%$ no such change occurs in the measured range $\kappa \leqslant 1.7$.

Similar to the case $\alpha_{main} = \alpha_{ref}$ at $Tu_u^x = 0.02\%$ of Chap. 6, increasing frequency of the inflow angle oscillations increases the range of the transition movement slightly up to $\kappa \approx 0.7$, above which it decreases toward higher κ. At both $Tu_u^x = 0.06\%$ and 0.13% the velocity of the upstream moving transition front $u_{tr,u}$, increases faster with κ than the steady case and vice versa for the downstream moving front. The latter approaches a limit value of $u_{tr,d}/U_\infty = 0.18$, which is slightly higher than found for the reference case $\alpha_{main} = \alpha_{ref}$ at $Tu_u^x = 0.02\%$ in Chap. 6. The case $\alpha_{main} = \alpha_{ref} + 0.5°$ at $Tu_u^x = 0.02\%$ is somewhat atypical, with significantly lower transition front velocities because of the smaller range of transition movement and more sine-like time trace of $x_{tr}(t)$. Nevertheless, up to $\kappa = 0.7$, $u_{tr,u}$ behaves similar to the cases with higher Tu. For $\kappa > 1.2$ the reduced signal to noise ratio prohibits further analysis of the transition front velocity.

The spatial-temporal development of the amplification rates over the inflow oscillation cycle largely exhibits the same characteristic features as the reference case $\alpha_{main} = \alpha_{ref}$ at $Tu_u^x = 0.02\%$ studied in Chap. 6. The peak n-factor levels decrease with increasing Tu, corresponding to the trend in wall pressure fluctuations in the steady measurements, see Fig. 5.2. Similarities with the case at α_{ref} are present also in the growth of n-factors along the TS wave trajectories through $x_{tr,mid,up}$ and $x_{tr,mid,down}$. The difference

in peak levels of the n-factor curves between the upstream and downstream moving transition along these trajectories are similar to those at α_{ref}. However, the absolute differences between the n-factor curves of the upstream and downstream transition are smaller at $\alpha_{ref} + 0.5°$.

An exception is the n-factor curve for the upstream moving transition at $Tu_u^x = 0.13\%$, for which the peak level is influenced by a rapid shift in peak-frequency. This is a result of a different transition scenario linked to the higher turbulence level.

The experiments show that, in the range of the current investigation, $0.05 \leqslant \kappa \leqslant 1.7$ and $0.02\% \leqslant Tu_u^x \leqslant 0.13\%$, the influence of additional free-stream turbulence leads to a general upstream shift of the transition location, similar to the steady case. The effect of free-stream turbulence level on the unsteady response of the boundary layer to inflow angle oscillations is small. Therefore, at least for turbulence levels $Tu_u^x \leqslant 0.13\%$, both phenomena can be treated as essentially independent and can be superposed. Up until now, the influence on boundary layer transition of a similar combination of inflow angle oscillations and free-stream turbulence is not covered by the available literature.

8. Conclusions

The present study describes experimental investigations related to the impact of unsteady inflow conditions on boundary layer transition. The measurements were performed on the pressure side of an NLF airfoil at operating conditions corresponding to cruise- or dash flight of general aviation aircraft. The study is focused on the change of the transition process under the influence of small-scale free-stream turbulence, inflow angle oscillations and a combination of the two. The selected amplitudes are representative for flight in the convective part of the atmosphere. The measurements were conducted in a low-speed wind tunnel where turbulence grids and a gust generator were used to generate the desired unsteady inflow. The $Re = 3.4 \cdot 10^6$ of the wind tunnel experiments were matched to full-scale flight conditions. This allows direct comparisons with flight measurements performed at the Technical University of Darmstadt.

The MW-166-39-44-43 airfoil model is equipped with pressure taps on the pressure side. The taps are connected to transducers capable of capturing the high-frequency pressure fluctuations of the transition process. Hot-wire anemometry was used to characterize the free-stream turbulence in the test section, as well as for detailed investigations of the boundary layer on the airfoil. The base flow of the steady reference case at a turbulence level of $Tu_u^s = 0.01\%$ was compared to LST, URANS simulations and DNS. A good overall agreement was found.

The influence of small-scale free-stream turbulence on the boundary layer transition was investigated in the range $0.01\% \leqslant Tu_u^s \leqslant 0.11\%$. The additional turbulence was generated by an active, pneumatic turbulence grid placed in the settling chamber of the tunnel. In the frequency range of the most amplified TS-waves, the spectral levels of the turbulence correspond to dissipation rates $4.3 \cdot 10^{-8} \leqslant \varepsilon^s \leqslant 3.1 \cdot 10^{-3}$ m^2/s^3. Within this range of turbulence, the base-flow on the airfoil is not altered. Nevertheless, with increased turbulence level the transition moves upstream, accompanied by a broadening of the TS-peak, which also shifts to higher frequencies. This is a result of the increase of initial disturbance amplitude A_0 at branch I of the neutral stability curve, in turn caused by free-stream disturbances entering the boundary layer through receptivity. In general, the main region of receptivity to free-stream turbulence is related to the leading edge, but the characteristic linear disturbance growth caused by distributed receptivity was

also observed in the current experiments.

Increasing Tu_u^s from 0.01% to 0.11% causes the quasi-uniform nature of the TS-dominated transition to gradually change into structures showing isolated wave packages. As the wave packets appear, increasing amounts of the disturbance energy is found at high spanwise wave numbers. The likely origin of the wave packets is an interaction between TS-waves and Klebanoff modes. Although Klebanoff modes are typically associated with higher turbulence levels than in the present study, the frequency spectra of the u' component as function of wall normal distance and the broadband eigenfunctions indicate their presence at Tu_u^s as low as 0.01% in the current experiment.

Comparing the surface pressure spectra of the current wind tunnel experiments with flight measurements show similar main characteristics, when compared at non-dimensional frequency. In addition, a good agreement is seen in the quantitative distribution between straight and oblique waves in the frequency wavenumber spectra.

The variation of the critical n-factor of the pressure side of the MW-166-39-44-43 airfoil is well predicted by the modified e^n method of Mack (1977) in the investigated range $0.03\% \leqslant Tu_u^s \leqslant 0.11\%$. This is in contrast to the classic measurements on flat plate boundary layers by Schubauer & Skramstad (1947) and Wells (1967), where the transition location remained largely unaffected below $Tu \approx 0.1\%$. Compared to the MW-166-39-44-43, the XIS40mod and NACA64-418 airfoils both exhibit significantly smaller influence of the turbulence level on n_{crit}. However, for all three airfoils, the change in critical n-factor in the investigated range of turbulence level is in the order of $\Delta n \geqslant 2$, a scale that is significant in the perspective of NLF airfoil design. Similarities in the c_p-distributions of the MW-166-39-44-43 airfoil and of a flat plate probably contributes to the good match with Mack's method, as the method is based on measurements on flat plates. As indicated by a simplified evaluation, the differences between the three airfoils in their sensitivity to turbulence cannot be fully accounted for by supposed differences in local receptivity.

The boundary layer response to large-scale free-stream disturbances was investigated by 2D, single-mode inflow angle oscillations. The case at the base $Tu_u^x = 0.02\%$ is examined, and it serves as the unsteady baseline for the following studies. A gust generator provided inflow angle oscillations in the range of reduced frequency $0.06 \leqslant \kappa \leqslant 1.7$ ($0.5 \leqslant f \leqslant 15$ Hz) at an equivalent zero-to-peak amplitude of $\alpha \approx 0.5°$. These conditions are representative for glider flight in the convective part of the atmosphere. As the frequency of the inflow oscillation increases, the temporal variation of the unsteady surface pressures p_{rms}, the transition location and the corresponding n-factors gradually depart from their quasi-steady behavior. The transition region moves faster upstream than downstream. A significantly lower peak is observed in

the instantaneous p_{rms} distribution during the part of the cycle with downstream moving transition. A similar trend, although stronger, is reported in Studer *et al.* (2006).

The range of the transition movement during the oscillation Δx_{tr}, increases slightly up to $\kappa \approx 0.5$, above which it decreases steadily. For $\kappa \gtrsim 0.5$, the downstream turning point of the transition changes less than the upstream one by a factor of 0.6.

An unsteady, trajectory-following LST is applied for comparisons. The trajectory-following LST employs URANS calculations for the unsteady baseflow. Matching the unsteady LST to the experimental transition locations at $\kappa = 1.0$ by using a critical n-factor of 12 and gust amplitude of $v'/U_\infty = 0.02$ provides a good correspondence with the measured range of transition movement as well as the time traces of x_{tr} in the range $0.7 \leqslant \kappa \leqslant 1.4$. By using lower gust amplitudes in the URANS, a fair resemblance with the measured x_{tr} time traces is found also for $\kappa < 0.7$.

The velocity of the transition front during the inflow angle cycle increases approximately linearly with oscillation frequency up to $\kappa \approx 0.7$. The upstream moving front moves progressively faster than the quasi steady case and vice versa for the downstream moving front. Above $\kappa \approx 0.7$, the increase in velocity with κ slows down in both parts of the cycle, and maxima of $u_{tr,u}/U_\infty = 0.35$ and $u_{tr,d}/U_\infty = 0.15$ appear to be reached at $\kappa \approx 1.4$. The $u_{tr,d}/U_\infty$ is significantly lower than the results by Studer *et al.* (2006), who found $u_{tr,d}/U_\infty = 0.4$ for the downstream moving front. Nevertheless, for the present experiment, the unsteady LST exhibits a similar trend for the downstream moving transition, but does not indicate an upper limit for the velocity of the upstream moving transition front in the investigated range of κ.

The effect of the temporal variations in the pressure distribution and the viscous delay of the boundary layer, and thereby the stability characteristics of the boundary layer, can be seen in the amplification rates deduced from the unsteady surface pressures. Along the TS-trajectories through the respective mid-points of the transition movement, $x_{tr,mid,up}$ and $x_{tr,mid,down}$, the growth of TS-waves during the upstream moving transition front occurs slightly further downstream than in the steady case, but the rate of growth is higher. The relation is reversed for the downstream moving transition, for which the maximum n-factor is lower than for the steady case. This is in line with the unsteady LST that predicts the primary instability point of the trajectory through $x_{tr,mid,up}$ slightly further downstream compared to the one through $x_{tr,mid,down}$. Along the $x_{tr,mid,up}$-trajectory, the LST shows lower levels of amplification upstream $x/c \approx 0.15$ and a higher amplification downstream this station.

Although DNS results with oscillating inflow angle have been available, limitations e.g. in the spectral content of the boundary layer disturbances

lead to differences in the flow cases. These differences, in turn, make a direct comparison with the measurements difficult. In the DNS, a fundamental resonance mode with $\omega = 201$ (corresponding to $f_{TS} \approx 900$ Hz)is introduced by a disturbance strip at $x/c = 0.15$. A fundamental resonance case is used, consisting of both a 2D mode ($\beta = 0\ \mathrm{m}^{-1}$) and 3D modes ($\beta = \pm 333\ \mathrm{m}^{-1}$, or $\approx \pm 40°$). This differs from the experiment, in which broadband disturbances are present in the boundary layer and the location of branch I depends on both the inflow angle and the disturbance frequency. However, the unsteady LST provides a bridge between the DNS and experiment and comparisons are presented for the case at $\kappa = 1.0$. The unsteady LST captures the main characteristics of the transition development of both the experiment and the DNS rather well. The main difference between the DNS and experiment is in the region of transition with significantly lower TS-peak. In the experiment, the TS-peak is lower only where the transition front is moving downstream. However, in the DNS this region occurs slightly later in the cycle and extends into the part where the transition is starting to move upstream again. Possible reasons for the differences include the single-mode excitation in the DNS, rather than the broadband disturbance spectrum of the experiment, as well as the fixed location of the generation of TS-waves in the DNS.

In the investigated range of conditions, increasing κ causes a gradual shift from quasi-steady boundary layer response to a clearly unsteady one. Still, the unsteadiness is not strong enough for a fully convective transition mode to form. Within this regime, comparisons to the experimental results show that the unsteady LST captures the main features of the mode development in the transitional phase well. This leads to the conclusion that the trajectory based approach of the unsteady LST can be reliably used for transition prediction in this range of unsteady inflow.

During flight through the atmospheric boundary layer, both small and large turbulence scales are present simultaneously. To study possible interaction effects, measurements with oscillation inflow were conducted at $Tu_u^x = 0.02\%$, 0.06% and 0.13% at $\alpha_{ref} + 0.5°$. The results show that these cases exhibit the same general behavior. With increasing κ, the transition region moves faster upstream and slower downstream than the steady case. The peak in $p_{rms}(x)$ is significantly lower in the part of the oscillation cycle when the transition is moving downstream than in the upstream moving part. The range of the transition movement increases slightly up to $\kappa \approx 0.7$, above which it decreases toward higher κ.

At the two higher turbulence levels, $Tu_u^x = 0.06\%$ and 0.13%, the velocity of the upstream moving transition front $u_{tr,u}$, increases faster with κ than the steady case. The downstream moving front approaches a limit value of $u_{tr,d}/U_\infty = 0.18$, which is slightly higher than for the unsteady baseline case. Also the spatial-temporal development of the amplification rate during the

oscillation is largely similar to the unsteady baseline case. The peak n-factor levels decrease with increasing Tu, corresponding to the trend in wall pressure fluctuations observed in the steady measurements.

The similarities to the unsteady baseline manifest themselves also in the growth of n-factors along the trajectories of the TS waves through $x_{tr,mid,up}$ and $x_{tr,mid,down}$. Along these trajectories, at all three levels of Tu, the trends in TS-peaks between the upstream and downstream moving transition are similar, although smaller. However, an exception is the case with highest turbulence level $Tu_u^x = 0.13\%$, for which the evaluation of the peak level of the n-factor curve through $x_{tr,mid,up}$ is influenced by a rapid shift in the frequency of the TS-peak. This is a result of a different transition scenario connected to the high turbulence level.

In summary, detailed investigations have been conducted on the boundary layer transition on an NLF airfoil influenced by small-scale turbulence, inflow angle oscillations and the combinations of the two. The test conditions have been matched to cruise flight of a general aviation aircraft in the convective part of the atmospheric boundary layer.

Based on the obtained results, small-scale turbulence influences the critical n-factor even for $Tu < 0.1\%$, provided that the free stream turbulence is the dominating cause of transition. The sensitivity of n_{crit} to the turbulence level is dependent on airfoil and base flow, but for all three airfoils studied, the decrease in n_{crit} with increasing Tu_u in the range $0.01\% \leqslant Tu_u^s \leqslant 0.11\%$ is significant. Consequently, the modified e^n method of Mack (1977) is applicable in this range of Tu, but should be used with caution if applied to cases other than flat plates with zero pressure gradient.

For flows with oscillating inflow angle, the existence of an intermediate range of unsteadiness has been demonstrated, in which the response of the transition is clearly unsteady, but a fully convective transition mode is not yet established. In this range of unsteadiness, trajectory-following LST captures the main features of the unsteady behavior of the transition well.

For combined small-scale turbulence and inflow angle oscillations, no significant interaction effects have been observed. In the investigated range of inflow condition, the two types of inflow disturbances appear to be essentially independent and trajectory-following LST is still applicable.

These findings contribute to the design methodology of future NLF airfoils for operation in the convective part of the atmosphere.

Bibliography

Abbott, I. H., Von Doenhoff, A. E. & Stivers Jr, L. 1945 Summary of airfoil data. *Tech. Rep.* 824. NACA.

Amandolese, X. & Széchényi, E. 2004 Experimental study of the effect of turbulence on a section model blade oscillating in stall. *Wind Energy* **7** (4), 267–282.

Arnal, D. & Juillen, J. 1978 Contribution experimentale a l'etude de la receptivite d'une couche limite laminaire, a la turbulence de l'ecoulement general. *Tech. Rep.* 1/5018. ONERA.

Atkin, C. 2009 e^n-why it works; when it doesn't; what's next? *ERCOFTAC Bulletin* **8**0, 77–81.

Ayyalasomayajula, S. & Warhaft, Z. 2006 Nonlinear interactions in strained axisymmetric high-reynolds-number turbulence. *Journal of Fluid Mechanics* **5**66, 273.

Azevedo, R., Roja-Solorzano, L. & Bento Leal, J. 2017 Turbulent structures, integral length scale and turbulent kinetic energy (TKE) dissipation rate in compound channel flow. *Flow Measurement and Instrumentation* **5**7, 10–19.

Babucke, A. 2009 Direct numerical simulation of noise-generation mechanisms in the mixing layer of a jet. PhD thesis, Universität Stuttgart, Institut für Aerodynamik und Gasdynamik.

Barlow, J., Rae, W. & Pope, A. 1999 *Low Speed Wind Tunnel Testing*. Wiley, New York.

Batchelor, G. K. & Townsend, A. A. 1948 Decay of isotropic turbulence in the initial period. *Proceedings of the Royal Society of London. Series A. Mathematical and Physical Sciences* **1**93 (1035), 539–558.

Bodini, N., Lundquist, J. & Newsom, R. 2018 Estimation of turbulence dissipation rate and its variability from sonic anemometer and wind doppler lidar during the XPIA field campaign. *Atmospheric Measurement Techniques* **1**1 (7), 4291–4308.

Boermans, L. 2006 Research on sailplane aerodynamics at Delft University of Technology, recent and present developments. *Tech Soar* **3**0 (1-2), 1–25.

Boiko, A. V., Dovgal, A. V., Grek, G. R. & Kozlov, V. V. 2011 *Physics of Transitional Shear Flows: Instability and Laminar–Turbulent Transition in Incompressible Near-Wall Shear Layers*. Springer, Dordrecht.

Boiko, A. V., Grek, G. R., Dovgal, A. & Kozlov, V. 2002 *The Origin of Turbulence in Near-Wall Flows*. Springer, Berlin Heidelberg.

Boiko, A. V., Westin, K., Klingmann, B., Kozlov, V. & Alfredsson, P. 1994 Experiments in a boundary layer subjected to free stream turbulence. Part 2. The role of TS-waves in the transition process. *Journal of Fluid Mechanics* **2**81, 219–245.

Borodulin, V. I., Ivanov, A. V., Kachanov, Y. S., Crouch, J. D. & Ng, L. L. 2014 Criteria of swept-wing boundary-layer transition and variable N-factor methods of transition prediction. In *Proc. 17th Int. Conf. Methods of Aerophysical Research, Novosibirsk, Russia*.

Borodulin, V. I., Kachanov, Y. S. & Koptsev, D. B. 2002*a* Experimental study of resonant interactions of instability waves in a self-similar boundary layer with an adverse pressure gradient: I. Tuned resonances. *Journal of Turbulence* **3**, N62.

Borodulin, V. I., Kachanov, Y. S. & Koptsev, D. B. 2002*b* Experimental study of resonant interactions of instability waves in self-similar boundary layer with an adverse pressure gradient: III. Broadband disturbances. *Journal of Turbulence* **3**, N64.

Borodulin, V. I., Kachanov, Y. S., Koptsev, D. B. & Roschektayev, A. P. 2002*c* Experimental study of resonant interactions of instability waves in self-similar boundary layer with an adverse pressure gradient: II. Detuned resonances. *Journal of Turbulence* **3**, N63.

Bradshaw, P. 1967 Conditions for the existence of an inertial subrange in turbulent flow. *Tech. Rep.* R. & M. 3603. Aeronautical Research Council.

Bradshaw, P. 1971 *An Introduction to Turbulence and its Measurement*. Pergamon Press, Oxford.

Brandt, L., Schlatter, P. & Henningson, D. S. 2004 Transition in boundary layers subject to free-stream turbulence. *Journal of Fluid Mechanics* **5**17, 167–198.

Bruun, H. H. 1995 *Hot-Wire Anemometry: Principles and Signal Analysis*. Oxford University Press, Oxford.

Bunker, A. F. 1955 Turbulence and shearing stresses measured over the North Atlantic Ocean by an airplane-acceleration technique. *Journal of Atmospheric Sciences* **1**2 (5), 445–455.

Carr, L. W., McAlister, K. W. & McCroskey, W. J. 1977 Analysis of the development of dynamic stall based on oscillating airfoil experiments. *Tech. Rep.* TN D-8382. NASA.

Carta, F. O. 1979 A comparison of the pitching and plunging response of an oscillating airfoil. *Tech. Rep.* CR-3172. NASA.

Cebeci, T., Smith, A. & Libby, P. 1974 Analysis of turbulent boundary layers. *Journal of Applied Mechanics* **4**3 (1), 189–189.

Choi, K-S & Lumley, J. 2001 The return to isotropy of homogeneous turbulence. *Journal of Fluid Mechanics* **4**36, 59–84.

Choudhry, A., Leknys, R., Arjomandi, M. & Kelso, R. 2014 An insight into the dynamic stall lift characteristics. *Experimental Thermal and Fluid Science* **5**8, 188–208.

Chougule, A., Mann, J., Segalini, A. & Dellwik, E. 2015 Spectral tensor parameters for wind turbine load modeling from forested and agricultural landscapes. *Wind Energy* **1**8 (3), 469–481.

Comte-Bellot, G. & Corrsin, S. 1966 The use of a contraction to improve the isotropy of grid-generated turbulence. *Journal of Fluid Mechanics* **2**5 (4), 657–682.

Conte, S. 1966 The numerical solution of linear boundary value problems. *SIAM Review* **8** (3), 309–321.

Corrsin, S. 1958 Local isotropy in turbulent shear flow. *Tech. Rep.* RM 58B11. NACA.

Crouch, J. 2008 Modeling transition physics for laminar flow control. In *38th Fluid Dynamics Conference and Exhibit*. American Institute of Aeronautics and Astronautics, AIAA 2008-3832.

Crouch, J. 2015 Boundary-layer transition prediction for laminar flow control (invited). In *45th AIAA Fluid Dynamics Conference*. American Institute of Aeronautics and Astronautics, AIAA 2015-2472.

Crouch, J. & Ng, L. L. 2000 Variable N-factor method for transition prediction in three-dimensional boundary layers. *AIAA Journal* **3**8 (2), 211–216.

De Paula, I. B., Würz, W., Krämer, E., Borodulin, V. I. & Kachanov, Y. S. 2013 Weakly nonlinear stages of boundary-layer transition initiated by modulated Tollmien–Schlichting waves. *Journal of Fluid Mechanics* **7**32, 571–615.

Devenport, W., Muthanna, C., Ma, R. & Glegg, S. 2001 Two-point descriptions of wake turbulence with application to noise prediction. *AIAA Journal* **3**9 (12), 2302–2307.

Djenidi, L. & Antonia, R. 2012 A spectral chart method for estimating the mean turbulent kinetic energy dissipation rate. *Experiments in Fluids* **5**3 (4), 1005–1013.

Drela, M. 1989 XFOIL: An analysis and design system for low Reynolds number airfoils. In *Low Reynolds Number Aerodynamics*, pp. 1–12. Springer-Verlag, Berlin.

Durbin, P. 2017 Perspectives on the phenomenology and modeling of boundary layer transition. *Flow, Turbulence and Combustion* **9**9, 1–23.

Farge, M. 1992 Wavelet transforms and their applications to turbulence. *Annual Review of Fluid Mechanics* **2**4 (1), 395–458.

Fasel, H. 2002 Numerical investigation of the interaction of the Klebanoff-mode with a Tollmien–Schlichting wave. *Journal of Fluid Mechanics* **4**50, 1–33.

Fransson, J. H. M. 2017 Free-stream turbulence and its influence on boundary-layer transition. In *10th International Symposium on Turbulence and Shear Flow Phenomena, TSFP 2017, Chicago, IL*, , vol. 2. Begell House, Danbury.

Fransson, J. H. M., Matsubara, M. & Alfredsson, P. H. 2005 Transition induced by free-stream turbulence. *Journal of Fluid Mechanics* **5**27, 1–25.

Fransson, J. H. M. & Shahinfar, S. 2020 On the effect of free-stream turbulence on boundary-layer transition. *Journal of Fluid Mechanics* **8**99.

Freymuth, P. & Fingerson, L. 1997 Hot-wire anemometry at very high frequencies: Effect of electronic noise. *Measurement Science and Technology* **8** (2), 115–116.

Fuglsang, P. & Bak, C. 2004 Development of the Risø wind turbine airfoils. *Wind Energy* **7** (2), 145–162.

Fujino, M., Yoshizaki, Y. & Kawamura, Y. 2003 Natural-laminar-flow airfoil development for a lightweight business jet. *Journal of Aircraft* **4**0 (4), 609–615.

Gostelow, J. P., Melwani, N. & Walker, G. J. 1996 Effects of streamwise pressure gradient on turbulent spot development. *Journal of Turbomachinery* **1**18 (4), 737–743.

Gostelow, J. P., Walker, G. J., Solomon, W. J., Hong, G. & Melwani, N. 1997 Investigation of the calmed region behind a turbulent spot. *Journal of Turbomachinery* **1**19 (4), 802–809.

Greiner, M. & Würz, W. 2021 Laminar separation bubbles at unsteady inflow conditions–a status report. In *XXXIV OSTIV Congress*, pp. 57–61. TU Braunschweig – Niedersächsisches Forschungszentrum für Luftfahrt.

Greiner, M. & Würz, W. 2022 In–flight measurement of free stream turbulence in the convective boundary layer. *Experiments in Fluids* **6**3 (10), 1432–1114.

Guissart, A., Nemitz, T. & Tropea, C. 2020 Laminar to turbulent transition at unsteady inflow conditions: Flight experiments under calm and moderately turbulent conditions. In *New Results in Numerical and Experimental Fluid Mechanics XII, Contributions to the 21st STAB/DGLR Symposium, Darmstadt, Germany, 2018*, pp. 185–194. Springer, Cham.

Guissart, A., Romblad, J., Nemitz, T. & Tropea, C. 2021 Small-scale atmospheric turbulence and its impact on laminar-to-turbulent transition. *AIAA Journal* **5**9 (9), 3611–3621.

Hallbäck, M., Groth, J. & Johansson, A. V. 1989 A Reynolds stress closure for the dissipation in anisotropic turbulent flows. In *7th Symposium on Turbulent Shear Flows, Volume 2*, pp. 17–2.

Han, J., Arya, S., Shen, S. & Lin, Y. 2000 An estimation of turbulent kinetic energy and energy dissipation rate based on atmospheric boundary layer similarity theory. *Tech. Rep.* CR-2000-210298. NASA.

Hearst, R. & Lavoie, P. 2015 The effect of active grid initial conditions on high Reynolds number turbulence. *Experiments in Fluids* **5**6 (10), 1–20.

Heinrich, R. & Reimer, L. 2013 Comparison of different approaches for gust modeling in the CFD code TAU. In *International Forum on Aeroelasticity and Structural Dynamics 2013, 24-26, June, Bristol, UK*.

Houbolt, John C. 1973 Atmospheric turbulence. *AIAA Journal* **1**1 (4), 421–437.

Ikami, T., Fujita, K., Nagai, H. & Yorita, D. 2021 Measurement of boundary layer transition on oscillating airfoil using cntTSP in low-speed wind tunnel. *Measurement Science and Technology* **3**2 (7), 075301.

van Ingen, J. 1956 A suggested semi-empirical method for the calculation of the boundary layer transition region. *Tech. Rep.* VTH-74. Technische Hogeschool Delft, Delft, Vliegtuigbouwkunde.

van Ingen, J. L. 1977 Transition, pressure gradient, suction, separation and stability theory. In *Laminar-Turbulent Transition, Copenhagen 1977*. AGARD CP-224.

Jacoby-Koaly, S., Campistron, B., Bernard, S., Bénech, B., Ardhuin–Girard, F., Dessens, J., Dupont, E. & Carissimo, B. 2002 Turbulent dissipation rate in the boundary layer via UHF wind profiler doppler spectral width measurements. *Boundary-Layer Meteorology* **1**03 (3), 361–389.

Jayesh & Warhaft, Z. 1991 Probability distribution of a passive scalar in grid-generated turbulence. *Physical Review Letters* **6**7 (25), 3503–3506.

Joseph, L., Borgoltz, A. & Devenport, W. 2014 Transition detection for low speed wind tunnel testing using infrared thermography. In *30th AIAA Aerodynamic Measurement Technology and Ground Testing Conference*. American Institute of Aeronautics and Astronautics, AIAA 2014-2939.

Kachanov, Y. 1994 Physical mechanisms of laminar-boundary-layer transition. *Annual Review of Fluid Mechanics* **2**6 (1), 411–482.

Kachanov, Yury S 2000 Three-dimensional receptivity of boundary layers. *European Journal of Mechanics-B/Fluids* **1**9 (5), 723–744.

Kaimal, J. & Finnigan, J. 1994 *Atmospheric Boundary Layer Flows: Their Structure and Measurement*. Oxford University Press, Oxford.

Kamruzzaman, M., Lutz, T., Herrig, A. & Krämer, E. 2012 Semi-empirical modeling of turbulent anisotropy for airfoil self-noise predictions. *AIAA Journal* **5**0 (1), 46–60.

Kanevče, G & Oka, S. 1973 Correcting hot-wire readings for influence of fluid temperature variations. *Disa Info.* **1**5, 21–24.

Kendall, J. 1985 Experimental study of disturbances produced in a pretransitional laminar boundary layer by weak freestream turbulence. In *18th Fluid Dynamics and Plasmadynamics and Lasers Conference*, p. 1695. American Institute of Aeronautics and Astronautics, AIAA 85-1695.

Kendall, J. 1990 Boundary layer receptivity to freestream turbulence. In *21st Fluid Dynamics, Plasma Dynamics and Lasers Conference*, p. 1504. American Institute of Aeronautics and Astronautics, AIAA 90-1504.

Kendall, J. 1998 Experiments on boundary-layer receptivity to freestream turbulence. In *36th AIAA Aerospace Sciences Meeting and Exhibit*, p. 530. American Institute of Aeronautics and Astronautics, AIAA 1998-530.

King, L. V. 1914 On the convection of heat from small cylinders in a stream of fluid: Determination of the convection constants of small platinum wires with applications to hot-wire anemometry. *Philosophical Transactions of the Royal Society of London. Series A, Containing Papers of a Mathematical or Physical Character* **2**14 (509-522), 373–432.

Klebanoff, P. S. 1971 Effect of free-stream turbulence on a laminar boundary layer. In *Bulletin of the American Physical Society*, , vol. 16, p. 1323. Amer Inst Physics.

Knebel, P., Kittel, A. & Peinke, J. 2011 Atmospheric wind field conditions generated by active grids. *Experiments in Fluids* **5**1 (2), 471–481.

Kolmogorov, A. 1941 The local structure of turbulence in incompressible viscous fluid for very large Reynolds numbers. *Cr Acad. Sci. URSS* **3**0, 301–305.

Kowalewski, T., Ligrani, P., Dreizler, A., Schulz, C., Fey, U. & Egami, Y. 2007 Temperature and heat flux. In *Handbook of Experimental Fluid Mechanics*, pp. 487–561. Springer-Verlag, Berlin Heidelberg.

Kubrynski, K. 2012 Design of a flapped laminar airfoil for high performance sailplane. In *30th AIAA Applied Aerodynamics Conference*, pp. 2012–2662. American Institute of Aeronautics and Astronautics, AIAA 2012-2662.

Kurian, T. & Fransson, J. 2009 Grid-generated turbulence revisited. *Fluid Dynamics Research* **4**1 (2), 021403.

Lancelot, P. M. G. J., Sodja, J., Werter, N. P. M. & De Breuker, R. 2017 Design and testing of a low subsonic wind tunnel gust generator. *Advances in Aircraft and Spacecraft Science* **4** (2), 125.

Larssen, J. & Devenport, W. 2011 On the generation of large-scale homogeneous turbulence. *Experiments in Fluids* **5**0 (5), 1207–1223.

Lee, T. & Gerontakos, P. 2004 Investigation of flow over an oscillating airfoil. *Journal of Fluid Mechanics* **5**12, 313–341.

Leung, J. M., Wong, J. G., Weymouth, G. D. & Rival, D. E. 2018 Modeling transverse gusts using pitching, plunging, and surging airfoil motions. *AIAA Journal* **5**6 (8), 3271–3278.

Li, S., Tse, K., Weerasuriya, A. & Chan, P. 2014 Estimation of turbulence intensities under strong wind conditions via turbulent kinetic energy dissipation rates. *Journal of Wind Engineering and Industrial Aerodynamics* **1**31, 1–11.

Loehrke, R. I., Morkovin, M. V. & Fejer, A. A. 1975 Review–Transition in nonreversing oscillating boundary layers. *Journal of Fluids Engineering* **9**7 (4), 534–549.

Lundquist, J. & Bariteau, L. 2015 Dissipation of turbulence in the wake of a wind turbine. *Boundary-Layer Meteorology* **1**54 (2), 229–241.

Mack, L. M. 1977 Transition and laminar instability. *Tech. Rep.* CP-153203. NASA.

Mack, L. M. 1984 Boundary-layer linear stability theory. In *Spec. Course on Stability and Transition of Laminar Flow*. AGARD-R-709. AGARD, Neuilly sur Seine, France.

Makita, H. 1991 Realization of a large-scale turbulence field in a small wind tunnel. *Fluid Dyn Res* **8** (1-4), 53–64.

Mathieu, J. & Alcaraz, E. 1965 Réalisation dune soufflerie à haut niveau de turbulence. *C R Acad Sci* **2**61 (13), 2435–2438.

Matsubara, M. & Alfredsson, P. 2001 Disturbance growth in boundary layers subjected to free-stream turbulence. *Journal of Fluid Mechanics* **4**30, 149–168.

McCroskey, W. J. 1981 The phenomenon of dynamic stall. *Tech. Rep.* TM-81264. NASA.

McKeon, B., Comte-Bellot, G., Foss, J., Westerweel, J., Scarano, F., Tropea, C., Meyers, J., Lee, J., Cavone, A., Schodl, R., Koochesfahani, M., Nocera, D., Andreopoulos, Y., Dahm, W.,

Mullin, J., Wallace, J., Vukoslavčević, P., Morris, S., Pardyjak, E. & Cuerva, A. 2007 Velocity, vorticity, and Mach number. In *Handbook of Experimental Fluid Mechanics*, pp. 215–471. Springer-Verlag, Berlin Heidelberg.

Miller, J. A. & Fejer, A. A. 1964 Transition phenomena in oscillating boundary-layer flows. *Journal of Fluid Mechanics* **1**8 (3), 438–448.

Mora, D., Muñiz Pladellorens, E., Riera Turró, P., Lagauzere, M. & Obligado, M. 2019 Energy cascades in active-grid-generated turbulent flows. *Physical Review Fluids* **4** (10), 104601.

Morkovin, M. V. 1969 Critical evaluation of transition from laminar to turbulent shear layers with emphasis on hypersonically traveling bodies. *Tech. Rep.* AFFDL-TR-68-149. Martin Marietta corp. Baltimore MD Research Inst. for Advanced Studies.

Mydlarski, L. 2017 A turbulent quarter century of active grids: From Makita (1991) to the present. *Fluid Dynamics Research* **4**9 (6), 061401.

Nagata, K., Saiki, T., Sakai, Y., Ito, Y. & Iwano, K. 2017 Effects of grid geometry on non-equilibrium dissipation in grid turbulence. *Physics of Fluids* **2**9 (1), 015102.

Nandi, T. & Yeo, D. 2021 Estimation of integral length scales across the neutral atmospheric boundary layer depth: A Large Eddy Simulation study. *Journal of Wind Engineering and Industrial Aerodynamics* **2**18, 104715.

Negi, P. S., Hanifi, A. & Henningson, D. S. 2021 Unsteady response of natural laminar flow airfoil undergoing small-amplitude pitch oscillations. *AIAA Journal* **5**9 (8), 2868–2877.

Nobach, H., Tropea, C., Cordier, L., Bonnet, J. P., Delville, J., Lewalle, J., Farge, M., Schneider, K. & Adrian, R. 2007 Review of some fundamentals of data processing. In *Handbook of Experimental Fluid Mechanics*, pp. 1337–1398. Springer-Verlag, Berlin Heidelberg.

Nyland, T. W. 1971 On the dynamics of short pressure probes: Some design factors affecting frequency response. *Tech. Rep.* TN D-6151. NASA.

Obremski, H. J. & Fejer, A. A. 1967 Transition in oscillating boundary layer flows. *Journal of Fluid Mechanics* **2**9 (1), 93–111.

Obremski, H. J. & Morkovin, M. V. 1969 Application of a quasi-steady stability model to periodic boundary-layer flows. *AIAA Journal* **7** (7), 1298–1301.

Ohno, D. 2023 Laminar-to-turbulent transition in airfoil boundary layer flows at oscillating inflow conditions. PhD thesis, Universität Stuttgart, Institut für Aerodynamik und Gasdynamik, thesis accepted by the Faculty of Aerospace Engineering and Geodesy of the University of Stuttgart.

Ohno, D., Greiner, M., Müller, J. & Rist, U. 2023 Numerical investigations of laminar separation bubbles under the influence of periodic gusts. *AIAA Journal* **61** (6), 2486–2499.

Ohno, D., Romblad, J., Khaled, M. & Rist, U. 2022 Investigations of laminar to turbulent transition in an oscillating airfoil boundary layer. In *IUTAM Laminar-Turbulent Transition, 9th IUTAM Symposium, London, UK, September 2–6, 2019*, pp. 469–478. Springer, Cham.

Ohno, D., Romblad, J. & Rist, U. 2020 Laminar to turbulent transition at unsteady inflow conditions: Direct numerical simulations with small scale free-stream turbulence. In *New Results in Numerical and Experimental Fluid Mechanics XII, Contributions to the 21st STAB/DGLR Symposium, Darmstadt, Germany, 2018*, pp. 214–224. Springer, Cham.

Otten, L., Pavel, A., Rose, W. & Finley, W. 1982 Atmospheric turbulence measurements from a subsonic aircraft. *AIAA Journal* **20** (5), 610–611.

Panda, J., Mitra, A., Joshi, A. & Warrior, H. 2018 Experimental and numerical analysis of grid generated turbulence with and without mean strain. *Experimental Thermal and Fluid Science* **98**, 594–603.

Peltzer, I. 2008 Comparative in-flight and wind tunnel investigation of the development of natural and controlled disturbances in the laminar boundary layer of an airfoil. *Experiments in Fluids* **44** (6), 961–972.

Plogmann, B. & Würz, W. 2013 Aeroacoustic measurements on a NACA 0012 applying the Coherent Particle Velocity method. *Experiments in Fluids* **54** (7), 1–14.

Pope, S. 2000 *Turbulent Flows*. Cambridge University Press, Cambridge.

Quast, A. 2006 Detection of transition by infrared image techniques. *Technical Soaring* **30** (1-2), 33–38.

Reed, H., Reshotko, E. & Saric, W. 2015 Receptivity: The inspiration of Mark Morkovin. In *45th AIAA Fluid Dynamics Conference*. American Institute of Aeronautics and Astronautics, AIAA 2015-2471.

Reeh, A. & Tropea, C. 2015 Behaviour of a natural laminar flow aerofoil in flight through atmospheric turbulence. *Journal of Fluid Mechanics* **7**67, 394–429.

Reeh, A. D. 2014 Natural laminar flow airfoil behavior in cruise flight through atmospheric turbulence. PhD thesis, Technische Universität Darmstadt.

Reshotko, E. 2001 Transient growth: A factor in bypass transition. *Physics of Fluids* **1**3 (5), 1067–1075.

Reshotko, E., Saric, W., Nagib, H., Reshotko, E., Saric, W. & Nagib, H. 1997 Flow quality issues for large wind tunnels. In *35th Aerospace Sciences Meeting and Exhibit*. American Institute of Aeronautics and Astronautics, AIAA 97-0225.

Richardson, L. 1922 *Weather Prediction by Numerical Process*. Cambridge University Press, Cambridge.

Riedel, H. & Sitzmann, M. 1998 In-flight investigations of atmospheric turbulence. *Aerospace Science and Technology* **2** (5), 301–319.

Ritter, F. 2016 Aufbau und experimentelle Untersuchung eines Systems zur variablen Beeinflussung des Turbulenzgrads im Laminarwindkanal. Studienarbeit, Institut für Aerodynamik und Gasdynamik, Universität Stuttgart.

Roach, P. 1987 The generation of nearly isotropic turbulence by means of grids. *International Journal of Heat and Fluid Flow* **8** (2), 82–92.

Romano, G., Ouellette, N., Xu, H., Bodenschatz, E., Steinberg, V., Meneveau, C. & Katz, J. 2007 Measurements of turbulent flows. In *Handbook of Experimental Fluid Mechanics*, pp. 745–855. Springer-Verlag, Berlin Heidelberg.

Romblad, J., Greiner, M., Guissart, A. & Würz, W. 2022*a* Characterization of low levels of turbulence generated by grids in the settling chamber of a laminar wind tunnel. *Experiments in Fluids* **6**3 (4), 1–24.

Romblad, J., Ohno, D., Guissart, A., Würz, W. & Krämer, E. 2022*b* Response of NLF airfoils to small scale turbulence. In *IUTAM Laminar-Turbulent Transition, 9th IUTAM Symposium, London, UK, September 2–6, 2019*, pp. 243–253. Springer, Cham.

Romblad, J., Ohno, D., Nemitz, T., Würz, W. & Krämer, E. 2018 Laminar to turbulent transition due to unsteady inflow conditions: Wind tunnel experiments at increased turbulence levels. In *Deutscher Luft- und Raumfahrtkongress 2018, Friedrichshafen*. Deutsche Gesellschaft für Luft- und Raumfahrt-Lilienthal-Oberth eV, Bonn.

Romblad, J., Ohno, D., Würz, W. & Krämer, E. 2020 Laminar to turbulent transition at unsteady inflow conditions: Wind tunnel measurements at oscillating inflow angle. In *New Results in Numerical and Experimental Fluid Mechanics XII, Contributions to the 21st STAB/DGLR Symposium, Darmstadt, Germany, 2018*, pp. 254–264. Springer, Cham.

Samuelson, R. 1967 Pneumatic instrumentation lines and their use in measuring rocket nozzle pressure. *Tech. Rep.* RN-DR-0124. Aerojet-General Corp., Sacramento, Calif.(USA).

Saric, W., Reed, H. & Kerschen, E. 2002 Boundary-layer receptivity to freestream disturbances. *Annu Rev Fluid Mech* **3**4, 291–319.

Schlichting, H. 1933 Zur Enstehung der Turbulenz bei der Plattenströmung. *Nachrichten von der Gesellschaft der Wissenschaften zu Göttingen, Mathematisch-Physikalische Klasse* **1**933, 181–208.

Schlichting, H. & Gersten, K. 2016 *Boundary-Layer Theory*, 9th edn. Springer-Verlag, Berlin Heidelberg.

Schrader, L-U, Brandt, L., Mavriplis, C. & Henningson, D. S. 2010 Receptivity to free-stream vorticity of flow past a flat plate with elliptic leading edge. *Journal of Fluid Mechanics* **6**53, 245–271.

Schubauer, G. & Skramstad, H. 1947 Laminar boundary-layer oscillations and transition on a flat plate. *Journal of Research of the National Bureau of Standards* **3**8 (2), 251.

Sears, W. R. 1941 Some aspects of non-stationary airfoil theory and its practical application. *Journal of the Aeronautical Sciences* **8** (3), 104–108.

Seitz, A. & Horstmann, K.-H. 2006 In-flight investigations of Tollmien–Schlichting waves. In *IUTAM Symposium on One Hundred Years of Boundary Layer Research*, pp. 115–124. Springer, Dordrecht.

Sheih, C., Tennekes, H. & Lumley, J. 1971 Airborne hot-wire measurements of the small-scale structure of atmospheric turbulence. *Physics of Fluids* **1**4 (2), 201.

Simmons, L. F. G. & Salter, C. 1934 Experimental investigation and analysis of the velocity variations in turbulent flow. *Proc R Soc A Math Phys Eng Sci* **1**45 (854), 212–234.

Sjögren, T. & Johansson, A. 1998 Measurement and modelling of homogeneous axisymmetric turbulence. *Journal of Fluid Mechanics* **3**74, 59–90.

Smith, A. M. O. & Gamberoni, N. 1956 Transition, pressure gradient, and stability theory. *Tech. Rep.* ES 26388. Douglas Aircraft Company Inc.

Sollo, A. 2021 P. 180 Avanti: An iconic airplane and the achievement of an historical milestone. *Aerotec Missili Spaz* **1**00 (1), 69–78.

Steiner, J. 2019 Untersuchung der Druckeigenfunktionen von Tollmien-Schlichting-Wellen für verschiedene Grenzschichtströmungen. Bachelorarbeit, Institut für Aerodynamik und Gasdynamik, Universität Stuttgart.

Studer, G., Arnal, D., Houdeville, R. & Seraudie, A. 2006 Laminar–turbulent transition in oscillating boundary layer: Experimental and numerical analysis using continuous wavelet transform. *Experiments in Fluids* **4**1 (5), 685–698.

Suder, K., Obrien, J. & Reshotko, E. 1988 Experimental study of bypass transition in a boundary layer. *Tech. Rep.* TM-100913. NASA.

Tan-atichat, J., Nagib, H. & Loehrke, R. 1980 Effects of axisymmetric contractions on turbulence of various scales. *Tech. Rep.* CR-165136. NASA.

Taylor, G. 1938 The spectrum of turbulence. *Proceedings of the Royal Society of London. Series A - Mathematical and Physical Sciences* **1**64 (919), 476–490.

Theodorsen, T. 1935 General theory of aerodynamic instability and the mechanism of flutter. *Annual Report of the National Advisory Committee for Aeronautics* **2**68, 413.

Timmer, W. & Van Rooij, R. P. J. O. M. 2003 Summary of the Delft university wind turbine dedicated airfoils. *Journal of Solar Energy Engineering* **1**25 (4), 488–496.

Tollmien, W. 1928 Über die Entstehung der Turbulenz. *Nachrichten von der Gesellschaft der Wissenschaften zu Göttingen, Mathematisch-Physikalische Klasse* **1**929, 21–44.

Trush, A., Pospíšil, S. & Kozmar, H. 2020 Comparison of turbulence integral length scale determination methods. In *Advances in Fluid Mechanics XII – papers from the 12th International Conference on Advances in Fluid Mechanics*, , vol. 128, pp. 113–123. WIT Press, Southampton.

Uberoi, M. 1956 Effect of wind-tunnel contraction on free-stream turbulence. *Journal of the Aeronautical Sciences* **2**3 (8), 754–764.

Watmuff, J. 1997 Interactions between Klebanoff modes and TS waves in a Blasius boundary layer. In *35th Aerospace Sciences Meeting and Exhibit*, p. 558. AIAA 97-0558.

Weismüller, M. 2012 A new approach to aerodynamic performance of aircraft under turbulent atmospheric conditions. PhD thesis, Technische Universität Darmstadt.

Wells, C. S. 1967 Effects of freestream turbulence on boundary–layer transition. *AIAA Journal* **5** (1), 172–174.

Wester, T. T. B., Krauss, J., Neuhaus, L., Hölling, A., Gülker, G., Hölling, M. & Peinke, J. 2022 How to design a 2D active grid for dynamic inflow modulation. *Flow, Turbulence and Combustion* **1**08 (4), 955–972.

Westin, K. J. A., Boiko, A. V., Klingmann, B. G. B., Kozlov, V. V. & Alfredsson, P. H. 1994 Experiments in a boundary layer subjected to free stream turbulence. Part 1. Boundary layer structure and receptivity. *Journal of Fluid Mechanics* **2**81, 193–218.

Wilder, M. & Telionis, D. 1998 Parallel blade–vortex interaction. *Journal of Fluids and Structures* **1**2 (7), 801–838.

Williams, G. 2016 Aerospace technology demonstration: Blade, the flagship laminar flow project within the clean sky programme. *Tech. Rep.* Technical Paper 2017-01-2016. SAE.

Wortmann, F. & Althaus, D. 1964 Der Laminarwindkanal des Instituts für Aero- und Gasdynamik an der Technischen Hochschule Stuttgart. *Z. Flugwiss* **1**2 (4), 129–134.

Wu, X. & Choudhari, M. 2001 Linear and nonlinear instabilities of a Blasius boundary layer perturbed by streamwise vortices. Part 2. Intermittent instability induced by long-wavelength Klebanoff modes. *Journal of Fluid Mechanics* **4**83, 249–286.

Wubben, F. J. M., Passchier, D. M. & Van Ingen, J. L. 1990 Experimental investigation of Tollmien-Schlichting instability and transition in similar boundary layer flow in an adverse pressure gradient. *Tech. Rep.* LR-604. Delft Technical University.

Würz, W. 1995 Hitzdrahtmessungen zum laminar-turbulenten Strömungsumschlag in anliegenden Grenzschichten und Ablöseblasen sowie Vergleich mit der linearen Stabilitätstheorie und empirischen Umschlagskriterien. PhD thesis, Universität Stuttgart, Institut für Aerodynamik und Gasdynamik.

Würz, W., Sartorius, D., Kloker, M., Borodulin, V. I., Kachanov, Y. S. & Smorodsky, B. V. 2012*a* Detuned resonances of Tollmien–Schlichting waves in an airfoil boundary layer: Experiment, theory, and direct numerical simulation. *Physics of Fluids* **2**4 (9), 094103.

Würz, W., Sartorius, D., Kloker, M., Borodulin, V. I., Kachanov, Y. S. & Smorodsky, B. V. 2012*b* Nonlinear instabilities of a non-self-similar boundary layer on an airfoil: Experiments, DNS, and theory. *European Journal of Mechanics-B/Fluids* **3**1, 102–128.

Wygnanski, I., Champagne, F. & Marasli, B. 1986 On the large-scale structures in two-dimensional, small-deficit, turbulent wakes. *Journal of Fluid Mechanics* **1**68 (-1), 31.

Wyngaard, J. 1968 Measurement of small-scale turbulence structure with hot wires. *Journal of Physics E: Scientific Instruments* **1** (11), 1105–1108.

Wyngaard, J. 1992 Atmospheric turbulence. *Annual Review of Fluid Mechanics* **2**4 (1), 205–234.

Zanin, B. 1985 Transition at natural conditions and comparison with the results of wind tunnel studies. In *Laminar-Turbulent Transition, IUTAM Symposium, Novosibirsk, USSR July 9–13, 1984*, pp. 541–546. Springer, Berlin Heidelberg.

Zanin, B. Y. 2020 Experimental study of the influence of atmospheric turbulence on the boundary layer flow on the glider wing. *Journal of Applied Mechanics and Technical Physics* **6**1 (5), 700–709.

Zhang, D. H., Chew, Y. T. & Winoto, S. H. 1996 Investigation of intermittency measurement methods for transitional boundary layer flows. *Experimental Thermal and Fluid Science* **1**2 (4), 433–443.

Zhu, C. & Wang, T. 2018 Comparative study of dynamic stall under pitch oscillation and oscillating freestream on wind turbine airfoil and blade. *Applied Sciences* **8** (8), 1242.

Zhu, Y. & Antonia, R. 1996 The spatial resolution of hot-wire arrays for the measurement of small-scale turbulence. *Measurement Science and Technology* **7** (10), 1349–1359.

A. Airfoil coordinates

See table on next page.

x/c	y/c	x/c	y/c	x/c	y/c	x/c	y/c
1.000175	0.000468	0.404393	0.127442	0.000367	0.003158	0.410086	-0.038714
0.997305	0.002293	0.395485	0.127370	0.000162	0.002064	0.419577	-0.038548
0.992710	0.004689	0.386581	0.127234	0.000039	0.000999	0.429065	-0.038366
0.987587	0.006912	0.377679	0.127033	0.000000	-0.000033	0.438554	-0.038166
0.981902	0.009151	0.368788	0.126771	0.000046	-0.001058	0.448045	-0.037950
0.975657	0.011478	0.359912	0.126443	0.000187	-0.002102	0.457534	-0.037718
0.968858	0.013911	0.351046	0.126049	0.000436	-0.003150	0.467024	-0.037469
0.961530	0.016454	0.342198	0.125590	0.000809	-0.004188	0.476516	-0.037203
0.953738	0.019102	0.333367	0.125063	0.001323	-0.005199	0.486012	-0.036921
0.945572	0.021837	0.324554	0.124469	0.001991	-0.006160	0.495511	-0.036624
0.937126	0.024638	0.315763	0.123805	0.002805	-0.007061	0.505009	-0.036312
0.928507	0.027473	0.306992	0.123072	0.003741	-0.007911	0.514507	-0.035983
0.919755	0.030317	0.298244	0.122269	0.004783	-0.008728	0.524008	-0.035640
0.910888	0.033176	0.289529	0.121396	0.005924	-0.009519	0.533507	-0.035282
0.901967	0.036035	0.280841	0.120447	0.007168	-0.010292	0.543006	-0.034909
0.893003	0.038883	0.272180	0.119425	0.008517	-0.011053	0.552508	-0.034520
0.883996	0.041728	0.263553	0.118328	0.009977	-0.011808	0.562005	-0.034118
0.874977	0.044564	0.254956	0.117154	0.011558	-0.012560	0.571498	-0.033700
0.865964	0.047380	0.246395	0.115903	0.013271	-0.013316	0.580988	-0.033268
0.856958	0.050172	0.237876	0.114575	0.015131	-0.014081	0.590470	-0.032820
0.847957	0.052940	0.229400	0.113167	0.017154	-0.014860	0.599944	-0.032357
0.838969	0.055680	0.220971	0.111679	0.019365	-0.015654	0.609407	-0.031877
0.829992	0.058390	0.212593	0.110109	0.021787	-0.016468	0.618856	-0.031380
0.821018	0.061070	0.204270	0.108456	0.024452	-0.017305	0.628293	-0.030865
0.812054	0.063720	0.196005	0.106716	0.027396	-0.018167	0.637709	-0.030332
0.803106	0.066335	0.187796	0.104887	0.030661	-0.019059	0.647102	-0.029778
0.794170	0.068912	0.179644	0.102969	0.034296	-0.019988	0.656471	-0.029202
0.785240	0.071452	0.171558	0.100963	0.038346	-0.020961	0.665811	-0.028603
0.776323	0.073952	0.163544	0.098867	0.042858	-0.021974	0.675119	-0.027977
0.767413	0.076411	0.155607	0.096681	0.047871	-0.023023	0.684394	-0.027323
0.758505	0.078830	0.147753	0.094403	0.053413	-0.024101	0.693626	-0.026640
0.749606	0.081209	0.139989	0.092032	0.059486	-0.025195	0.702812	-0.025923
0.740727	0.083542	0.132318	0.089566	0.066071	-0.026290	0.711948	-0.025170
0.731869	0.085824	0.124747	0.087005	0.073130	-0.027371	0.721029	-0.024378
0.723031	0.088054	0.117282	0.084349	0.080605	-0.028428	0.730048	-0.023543
0.714212	0.090228	0.109932	0.081598	0.088416	-0.029449	0.739001	-0.022661
0.705410	0.092344	0.102706	0.078754	0.096486	-0.030416	0.747883	-0.021728
0.696628	0.094400	0.095615	0.075822	0.104777	-0.031323	0.756689	-0.020741
0.687869	0.096390	0.088681	0.072809	0.113251	-0.032169	0.765413	-0.019694
0.679109	0.098311	0.081921	0.069721	0.121869	-0.032959	0.774048	-0.018582
0.670321	0.100173	0.075355	0.066569	0.130593	-0.033689	0.782593	-0.017394
0.661510	0.101986	0.069012	0.063368	0.139412	-0.034361	0.791070	-0.016112
0.652706	0.103743	0.062923	0.060136	0.148311	-0.034979	0.799540	-0.014717
0.643906	0.105436	0.057117	0.056892	0.157275	-0.035544	0.808069	-0.013209
0.635098	0.107069	0.051620	0.053657	0.166294	-0.036059	0.816689	-0.011601
0.626289	0.108640	0.046460	0.050462	0.175363	-0.036525	0.825395	-0.009913
0.617479	0.110149	0.041658	0.047332	0.184482	-0.036946	0.834153	-0.008167
0.608662	0.111595	0.037226	0.044295	0.193646	-0.037325	0.842930	-0.006413
0.599838	0.112979	0.033169	0.041375	0.202849	-0.037666	0.851670	-0.004692
0.591008	0.114300	0.029483	0.038587	0.212087	-0.037970	0.860247	-0.003033
0.582171	0.115559	0.026151	0.035937	0.221359	-0.038240	0.868585	-0.001488
0.573326	0.116755	0.023151	0.033427	0.230662	-0.038479	0.876711	-0.000079
0.564476	0.117889	0.020454	0.031052	0.239989	-0.038688	0.884621	0.001179
0.555620	0.118959	0.018031	0.028809	0.249339	-0.038868	0.892333	0.002261
0.546758	0.119967	0.015856	0.026690	0.258711	-0.039023	0.899912	0.003158
0.537893	0.120911	0.013900	0.024685	0.268100	-0.039152	0.907428	0.003876
0.529019	0.121791	0.012141	0.022787	0.277505	-0.039257	0.914903	0.004431
0.520140	0.122609	0.010558	0.020985	0.286927	-0.039340	0.922331	0.004828
0.511261	0.123364	0.009132	0.019271	0.296361	-0.039402	0.929715	0.005068
0.502378	0.124053	0.007849	0.017636	0.305803	-0.039443	0.937039	0.005153
0.493489	0.124678	0.006694	0.016072	0.315258	-0.039464	0.944290	0.005080
0.484595	0.125240	0.005656	0.014572	0.324725	-0.039467	0.951461	0.004854
0.475696	0.125737	0.004727	0.013129	0.334194	-0.039452	0.958518	0.004481
0.466791	0.126171	0.003896	0.011739	0.343667	-0.039418	0.965435	0.003963
0.457879	0.126542	0.003154	0.010397	0.353149	-0.039367	0.972181	0.003313
0.448964	0.126850	0.002497	0.009099	0.362635	-0.039299	0.978694	0.002549
0.440049	0.127096	0.001923	0.007841	0.372123	-0.039215	0.984935	0.001688
0.431136	0.127278	0.001425	0.006620	0.381611	-0.039115	0.990837	0.000781
0.422223	0.127396	0.001000	0.005434	0.391101	-0.038997	0.996351	-0.000031
0.413308	0.127450	0.000647	0.004281	0.400593	-0.038863	0.999824	-0.000468

Table A.1.: Coordinates MW-166-39-44-43 airfoil

B. Turbulence characterization - passive grids

Passive grids offer a simple and reliable tool for generating turbulence in wind tunnels. The grids used in the current work are described in detail in Sect. 2.2.1. Details about the measurement techniques employed for characterizing the generated turbulence can be found in Sect. 2.5. Unless otherwise noted, the measurements were conducted at $x_{ts} = 1.8$ m, corresponding to the center of the turntable. This appendix is a slight adaptation of Romblad *et al.* (2022*a*).

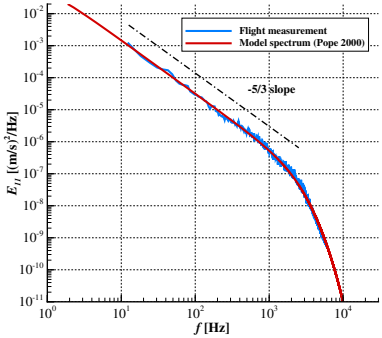

Figure B.1.: One-dimensional turbulence spectrum measured in flight Guissart *et al.* (2021) and a model spectrum according to Pope (2000) with $U_\infty = 45.6$ m/s, $\varepsilon = 7.15 \cdot 10^{-3}$ m^2/s^3 and $\nu = 17 \cdot 10^{-6}$ m^2/s. From Romblad *et al.* (2022*a*)[1].

B.1. Energy spectra

The basic properties of inflow turbulence can be discussed in terms of their spectral content. The turbulence spectrum can be separated into three ranges of frequency, or corresponding length scales (Kolmogorov, 1941; Pope, 2000). The energy containing range where turbulent energy is generated, the inertial subrange in which eddy break-up transports energy to progressively smaller

[1] Used under Creative Commons Attribution 4.0 International License, http://creativecommons.org/licenses/by/4.0/

scales, and the dissipative subrange where the viscosity dissipates the turbulence energy to heat. Figure B.1 shows a typical power spectrum of the longitudinal turbulence E_{11} measured in flight in the convective part of the atmospheric boundary layer, see Guissart *et al.* (2021) for details. A model spectrum (Pope, 2000) is fitted to the measurement. The energy containing range with its very large length scales is found at lower frequencies than are resolved in the measurement, and is not present in the figure. The inertial subrange, with its characteristic -5/3 exponent slope, covers the range $f \lesssim$ 1000 Hz in the figure, above which the dissipative subrange is clearly seen.

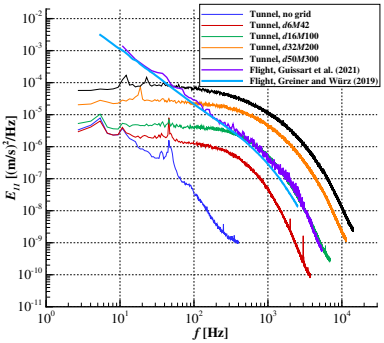

Figure B.2.: Turbulence spectrum for tunnel and flight for $U_\infty = 40$ m/s, u-component. From Romblad *et al.* (2022*a*)[2].

The spectral distribution of grid-generated turbulence in wind tunnels is inherently different to atmospheric turbulence. The dissipative subrange is often well represented, but the inertial subrange does not extend as far into the lower frequencies as in the case of atmospheric turbulence. Figure B.2 shows spectra of the longitudinal component for $U_\infty = 40$ m/s for grid generated turbulence in the LWT wind tunnel and atmospheric turbulence measured in flight. See Guissart *et al.* (2021) and Greiner & Würz (2021) for descriptions of the respective flight measurements. The flight measurements were conducted at flight speeds of approximately 40 m/s and the data have been recalculated to $U_\infty = 40$ m/s from the corresponding wavenumber spectrum using Taylor's frozen turbulence assumption (Taylor, 1938). In the wind tunnel spectra, the peaks at $f \approx 5$ Hz and 10 Hz are caused by standing acoustic waves along the length of the open tunnel circuit. The peaks in the range 10 $< f <$ 100 Hz are linked to the blade-stator passing frequency of the tunnel fan and the power grid frequency. The spectra measured in flight and in

[2] Used under Creative Commons Attribution 4.0 International License, http://creativecommons.org/licenses/by/4.0/

the wind tunnel with grids correspond well in the dissipative subrange, $f \geqslant$ 400 Hz, but the differences increase progressively toward lower frequencies. As discussed in Sect. 2.2, the current grids are intended for investigations of TS-driven transition on NLF airfoils where amplification of disturbances occur for $500 \lesssim f \lesssim 3000$ Hz. In this range, the turbulence spectra measured in the wind tunnel and in flight show a good agreement. The four grids provide convenient incremental shifts in turbulence energy across practically the whole frequency range of the measurements. Thereby, different atmospheric conditions can be covered, ranging from "calm" up to "severe" (Weismüller, 2012) and reflecting a range of dissipation rates discussed below.

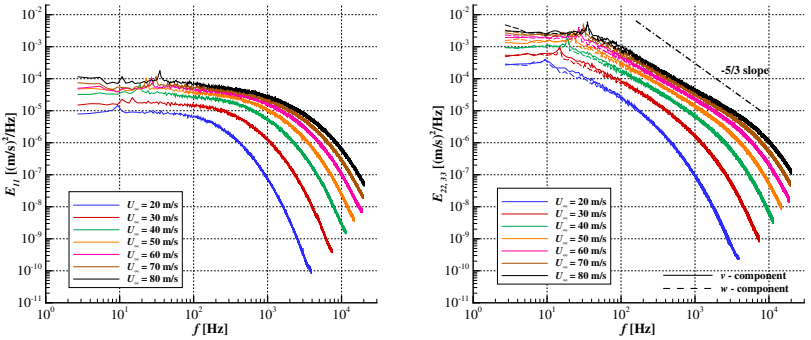

(a) u-component. (b) v and w-components.

Figure B.3.: Spectra for grid $d32M200$ for $20 \leqslant U_\infty \leqslant 80$ m/s. From Romblad *et al.* (2022*a*)[3].

The spectra of the transverse components match the longitudinal component well in the dissipative subrange, as exemplified by the grid $d32M200$ in Figures B.3a and B.3b respectively. At the low frequency part of the spectrum there is significantly more energy in the transverse directions than in the longitudinal. This observation is consistent with the investigations of Uberoi (1956), Tan-atichat *et al.* (1980) and Ayyalasomayajula & Warhaft (2006) regarding the influence of contractions on isotropic turbulence. Both Uberoi (1956) and Ayyalasomayajula & Warhaft (2006) show spectra where the contraction attenuates the energy at low frequencies in the longitudinal direction. In the same range of frequencies, they show that the energy in the transverse directions are maintained or slightly increased.

[3]Used under Creative Commons Attribution 4.0 International License, http://creativecommons.org/licenses/by/4.0/

The v and w-components in Fig. B.3b exhibit an inertial subrange for 10 $\leqslant f \leqslant$ 100 Hz at 20 m/s, which becomes more pronounced as the free-stream velocity increases, covering 50 $\leqslant f \leqslant$ 3000 Hz at 80 m/s. The slope of the spectra in the inertial subrange is less steep than the -5/3 of the Kolmogorov spectrum. Other authors, including Kurian & Fransson (2009) and Mora *et al.* (2019) have also reported slopes deviating from -5/3 in the inertial subrange. Mora *et al.* (2019) observed a less steep slope than -5/3 in the longitudinal spectrum of turbulence from a stationary (inactive), vane type active grid and the slope appears largely unaffected by free-stream velocity. Kurian & Fransson (2009) measured slopes that varied slightly, both above and below -5/3 in isotropic grid turbulence, the slope becoming less steep with increasing free-stream velocity.

As demonstrated for the grid $d32M200$ in Fig. B.3, the energy of both the longitudinal and transverse turbulence increase across the whole frequency range with increasing free-stream velocity. This is contrary to flight through turbulent air where, according to Taylor's hypothesis of frozen turbulence (Taylor, 1938), increasing velocity shifts the spectrum to higher frequencies and reduces the power spectral density.

B.2. Flow uniformity across test section

The flow just downstream a turbulence grid is inherently non-uniform with discrete wakes shed from each rod of the grid. The turbulent wakes need a certain distance to merge and for the turbulence to become uniform. As described in Sect. 2.2, different criteria for the distance required for uniform turbulence have been proposed, most being based on the mesh width M. However, as described by Wygnanski *et al.* (1986), the development of the wake behind a cylinder depends strongly on its diameter. The experiments by Wygnanski *et al.* (1986) show that the width of both the velocity deficit and the distribution of turbulence in the wake downstream a cylinder is close to self-similar if expressed in terms of

$$y_{norm} = \frac{y}{L_0} \tag{B.1}$$

where y is the coordinate across the width of the wake and L_0 is the width from the wake center to the point where the velocity deficit is half of the value in the center of the wake. This equation is based on the assumption of a self-preserving flow state for a small deficit far-wake at zero pressure gradient. Taking the drag coefficient of the cylinder into account, the equations of Wygnanski *et al.* (1986) can be reformulated to express the width of the velocity deficit as

$$L_0 = \sqrt{\frac{d \cdot C_D \cdot (x - x_o) \cdot B}{4}} \tag{B.2}$$

where d is the diameter of the cylinder, C_D is the drag coefficient and B is a universal constant. The streamwise distance downstream of the cylinder x, is corrected depending on the shape of the cylinder by x_0.

Measurements by Wygnanski *et al.* (1986) show that the universal constant B is only marginally dependent on the type of wake generator. Very similar behavior is found for cylinders with different diameters as well as screens having a solidity in the range of 30% to 70%.

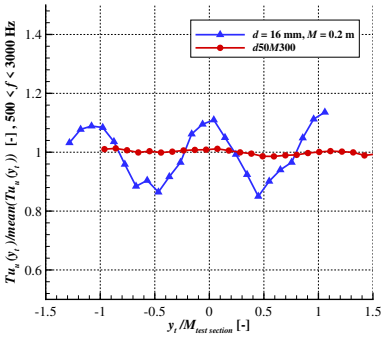

(a) $Tu_u^x(y_t)/\text{mean}(Tu_u^x(y_t))$ across the test section.

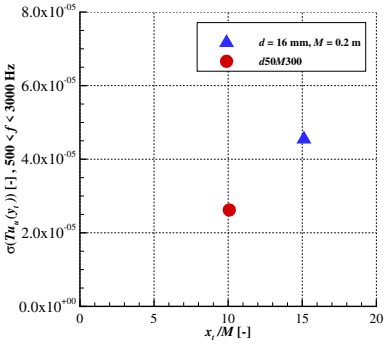

(b) The standard deviation $\sigma(Tu_u^x(y_t))$ of the two grids as function or x_t/M.

Figure B.4.: The flow uniformity across the test section for grid $d50M300$ compared to a demonstrator grid $d = 16$ mm, $M = 200$ mm. After Romblad *et al.* (2022*a*).

Based on Eq. B.2 follows that grids with smaller rod diameter d require a longer distance downstream the grid to become homogenous, assuming the mesh width M is kept constant. An example can be seen in Fig. B.4a, where the distribution of $Tu_u^x(y_t)/\text{mean}(Tu_u^x(y_t))$ across the width of the test section is plotted. Here the turbulence level is calculated for the main TS frequency range $500 \leqslant f \leqslant 3000$ Hz. Spanwise Tu variations were found to be more easily distinguished in this frequency range, compared to the wider $10 \leqslant f \leqslant 5000$ range. In Fig. B.4a, a demonstrator grid with $d = 16$ mm, $M = 200$ mm (twice the mesh width compared to the $d16M100$ grid used in the current thesis) is compared to the $d50M300$ at $U_\infty = 40$ m/s. The distance between the grids and the hot-wire probe expressed in x_t/M is 33 and 22 for the demonstrator grid and $d50M300$ grid respectively. As seen in Fig. B.4a,

the distribution of turbulence for the $d50M300$ grid is practically constant across the test section. Despite a smaller mesh width M, the demonstrator grid exhibits clear variations in Tu, corresponding to the grid spacing (scaled with the contraction ratio in y_t-direction). Figure B.4b shows the same trend for the standard deviation of $Tu_u^x(y_t)$. Clearly, a criterion for homogenous turbulence downstream a turbulence grid based solely on mesh size M can be misleading.

All grids employed in the current study exhibit an essentially uniform distribution in the y_t-direction of both mean velocity and turbulence level for all three velocity components, i.e. $\frac{\sigma(\bar{u}(y_t)}{\bar{u}(y_t)} < 0.5$ % and $\frac{\sigma(Tu(y_t))}{Tu(y_t)} < 2.7$%, $500 \leqslant f \leqslant 3000$ Hz respectively.

B.3. Turbulence level, anisotropy and dissipation rate

The results presented in this appendix were obtained with x-wire probes. These probes are typically more intrusive than single wire probes and tend to show higher values for Tu and the dissipation rate ε, in particular at low levels of turbulence (the determination of the dissipation rate is discussed in the latter part of this section, in relation to Fig. B.8). Because this phenomenon might influence the findings presented here, a comparison was conducted of measurements using the x-wire probe and a single wire probe with a 0.5 mm long, 2.5 μm diameter wire. Without turbulence grid, both probes agree fairly well at 20 m/s. With increasing U_∞ the ratio $\Theta = \frac{\varepsilon_{x-wire}}{\varepsilon_{singlewire}}$ increases to 3.2 at 60 m/s, above which it falls to $\Theta = 2.6$ at $U_\infty = 75$ m/s. For the finest grid, $d6M42$ the ratio is close to constant, $\Theta \approx 1.3$, independent of U_∞. For the coarser grids, the two probes typically measure dissipation rates differing less than ± 10%, which is regarded as acceptable in the current study.

A first, coarse characterization of the grid turbulence is obtained by the integral turbulence level calculated for a frequency range of $10 \leqslant f \leqslant 5000$ Hz, see Fig. B.5. The isotropic turbulence generated by two grids studied by Kurian & Fransson (2009) is used for comparison, the finer "LT3" with $d = 0.45$ mm, $M = 1.8$ mm and the coarser "E" with $d = 10$ mm, $M = 50$ mm. The data from Kurian & Fransson (2009) were acquired at a constant $x_t/M = 100$. In contrast, the current measurements were made at a constant distance to the grids of $x_t = 6.7$ m, resulting in different x_t/M depending on the grid dimension, see Table 2.1.

The current grids produce turbulence levels in the range $0.04\ \% < Tu_u^x < 0.40\ \%$ and $0.08\ \% < Tu_u^x < 0.52\ \%$ for $U_\infty = 20$ and 80 m/s respectively. This is significantly lower than the LT3 and E grids of Kurian & Fransson (2009), which cover $0.93\ \% < Tu_u < 1.01\ \%$ and $1.45\ \% < Tu_u < 1.93\ \%$

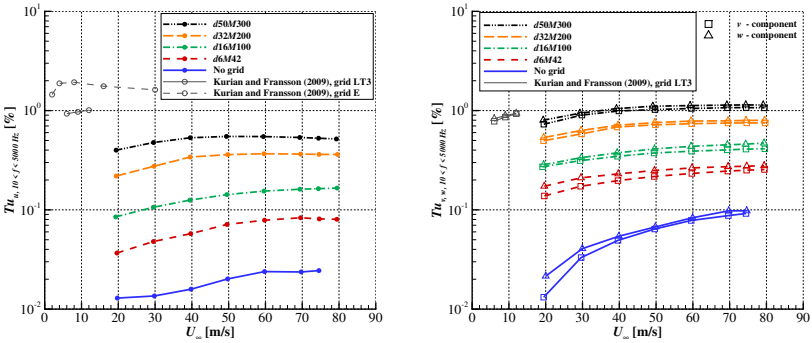

(a) u-component. (b) v and w-components.

Figure B.5.: Tu for the different grids as function of U_∞. From Romblad *et al.* (2022*a*)[4].

in their respective range of U_∞. The differences reflect the lower design Tu for the grids in the current study. For the $d6M42$ and $d16M100$ grids, the Tu level increases monotonically with free-stream velocity. For the coarser grids $d32M200$ and $d50M300$, the level of Tu in both the longitudinal and the transverse directions reaches a plateau at high U_∞. In the longitudinal direction the turbulence level even drops slightly at the highest velocities for the $d50M300$ grid. This behavior can be linked to Re_d, the Reynolds number calculated from the grid rod diameter and the free-stream velocity at the grids, based on U_∞ and the contraction ratio. The plateau occurs for $Re_d \gtrsim 5000 - 8000$ in the current measurement, a level only reached for the $d32M200$ and $d50M300$ grids. A similar trend is seen in the data of Kurian & Fransson (2009) for $Re_d \gtrsim 3000 - 6000$ for their two coarsest grids A and E. The slight reduction in Tu_u^x at $U_\infty \geqslant 70$ m/s for the $d6M42$ grid is related to scatter in the measurement data, and is most likely not linked to the plateau seen for $Re_d \gtrsim 5000 - 8000$.

By comparing the levels of Tu_u^x in Fig. B.5a with the Tu_v and Tu_w of Fig. B.5b, it is clear that the turbulence in the test section is anisotropic. The disturbance level ratios v_{rms}/u_{rms} and w_{rms}/u_{rms} in Fig. B.6 highlights the anisotropy because $v_{rms}/u_{rms} = w_{rms}/u_{rms} = 1$ can be expected for isotropic turbulence. At $U_\infty = 20$ m/s the disturbance level ratios from the different grids fall in the range $1.8 \leqslant v_{rms}/u_{rms} \leqslant 3.8$ and $2.1 \leqslant w_{rms}/u_{rms} \leqslant 3.2$. At $U_\infty = 80$ m/s the range is slightly reduced to $2.0 \leqslant v_{rms}/u_{rms} \leqslant 4.7$ and $2.2 \leqslant w_{rms}/u_{rms} \leqslant 3.5$. Coarser grids show lower values of the disturbance level ratios. The v_{rms}/u_{rms} and w_{rms}/u_{rms} levels decrease with increasing

U_∞ for grids $d6M42$ and $d16M100$, whereas they increase for the other cases. This anisotropy is expected, because the turbulence generating grid is placed upstream of the contraction in the wind tunnel, as described in Sect. 2.2. Although grids generate turbulence that is approximately isotropic, the contraction between the grid and the test section attenuates the large length scales in the u-component but leaves the v and w-components less affected, as seen in e.g. Uberoi (1956) and Ayyalasomayajula & Warhaft (2006).

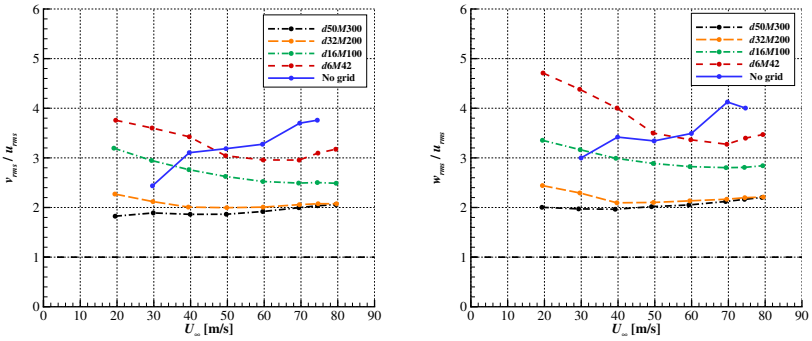

(a) $v_{rms}/\ u_{rms}$. (b) $w_{rms}/\ u_{rms}$.

Figure B.6.: Disturbance level ratios for the different grids. From Romblad *et al.* (2022*a*)[5].

The frequency-dependent influence of the contraction is clearly seen when comparing the spectra in Fig. B.3a and Fig. B.3b. To describe the anisotropy with respect to frequency, it is helpful to define an anisotropy coefficient a_r, that describes the anisotropy as a function of the frequency, i.e.

$$a_r(f) = \frac{E_{11}(f)}{E_{22}(f)} \tag{B.3}$$

Figure B.7 shows a_r for the different grids at $U_\infty = 40$ m/s. Isotropic turbulence is represented by a model spectrum (Pope, 2000) which uses values for ν and ε that are taken from the measurement with the $d50M300$ grid. For all four grids, the anisotropy is large for low frequencies with $a_r \approx 0.06$ for $f \lesssim 10$ Hz, above which the anisotropy gradually decreases. The anisotropy coefficient is close to the theoretical value for isotropic turbulence of 0.75 (Sheih *et al.*, 1971) in the range of $900 \lesssim f \lesssim 3000$ Hz. The increased isotropy toward higher frequencies corresponds well with the hypothesis of

[5] Used under Creative Commons Attribution 4.0 International License, http://creativecommons.org/licenses/by/4.0/

local isotropy of Kolmogorov (1941). In the current measurements, a_r exhibits a maximum above which it steadily decreases. The decrease in a_r with increasing frequency, i.e. well into the dissipation range, is also seen for the model spectrum. The finer grids shift the range of low anisotropy toward higher frequencies. This shift has an influence on the anisotropy seen in the disturbance level ratios of Fig. B.6. For the finer grids, a larger part of the frequency range with high anisotropy falls inside the $10 \leqslant f \leqslant 5000$ Hz range over which the rms values are integrated, compared to the coarser grids. Consequently, the grid dependent anisotropy seen in the disturbance level ratio in Fig. B.6 does not mean that the turbulence generated by coarser grids is more isotropic across the entire frequency range than the one generated by finer grids.

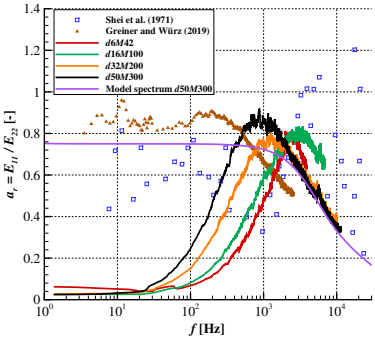

Figure B.7.: Anisotropy coefficient ar as function of frequency for the four grids at $U_\infty = 40$ m/s, compared to flight measurements. The isotropic model spectrum (Pope, 2000) uses ν and ε values extracted from the $d50M300$ measurement. From Romblad *et al.* (2022*a*)[6].

Included in Fig. B.7 are flight measurement data from Sheih *et al.* (1971) and Greiner & Würz (2021). The flight data has been transformed from wave number to frequency using the Taylor hypothesis. The two flight measurements show somewhat different results and the data from Sheih *et al.* (1971) exhibits a high degree of scatter. However, apart from a few outliers, both fall in the range of $0.4 \lesssim a_r \lesssim 0.9$. In the frequency range of interest ($500 \leqslant f \leqslant 3000$ Hz), the ar of the two coarser grids fall in the same range as the flight measurements. In contrast, the two finer grids show an $a_r < 0.4$ at the low frequency end of the range.

[6]Used under Creative Commons Attribution 4.0 International License, http://creativecommons.org/licenses/by/4.0/

As discussed in Sect. B.1, the spectral differences between turbulence in the wind tunnel and the free atmosphere occur primarily in the low frequency part of the spectrum. For typical general aviation aircraft and wind turbines applications, TS-amplification mainly occurs in the range $500 \lesssim f \lesssim 3000$ Hz. The part of the turbulence spectrum below $f \approx 100$ Hz, which constitutes the dominating part of the integral turbulence level, represents unsteady variations in angle of attack, which influences the transition in a different way than the small-scale turbulence. Consequently, the turbulence level integrated over the range $10 \leqslant f \leqslant 5000$ Hz is a poor parameter for comparing the effect of small-scale turbulence on NLF airfoils in the atmosphere and wind tunnels. A more suitable parameter is the dissipation rate ε, which describes the rate by which turbulence energy is transported from low frequencies to high frequencies in the inertial subrange.

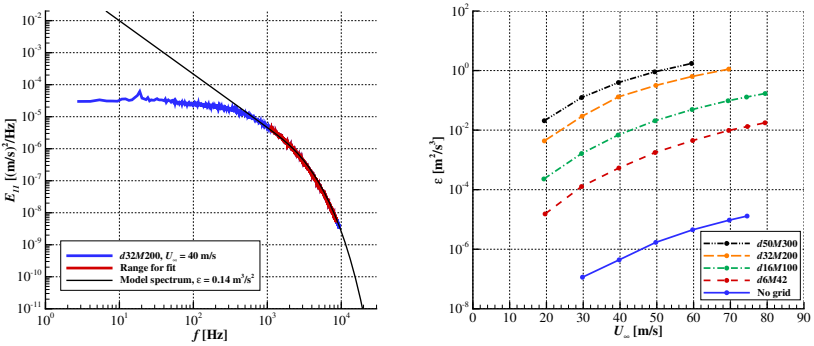

(a) Fitting of a model spectrum to determine the dissipation rate, ε according to (Djenidi & Antonia, 2012).

(b) Dissipation rate for the different grids as function of U_∞.

Figure B.8.: Turbulence dissipation rate. From Romblad *et al.* (2022*a*)[7].

For determining the dissipation rate, the method of Djenidi & Antonia (2012) is adopted, where ε is estimated by fitting a model spectrum to the measured E_{11} spectrum. As demonstrated by Djenidi & Antonia (2012), the method works well also for anisotropic turbulence. An example of the fitting is seen in Fig. B.8a. The resulting dissipation rates shown in Fig. B.8b exhibit a steady increase of ε with increasing flow velocity for all grids. The total range of dissipation rate generated by the grids covers $1.5 \cdot 10^{-5} \leqslant \varepsilon \leqslant 1.7$ m^2/s^3. Including the case without grid, it is possible to achieve $4.4 \cdot 10^{-7} \leqslant$

[7] Used under Creative Commons Attribution 4.0 International License, http://creativecommons.org/licenses/by/4.0/

$\varepsilon \leqslant 4.0 \cdot 10^{-1}$ m^2/s^3 at $U_\infty = 40$ m/s.

The suitability of the dissipation rate as a descriptor for the impact of small-scale turbulence on TS-driven boundary layer transition is demonstrated in Fig. B.2. For $f \geqslant 400$ Hz, the spectrum from the flight measurements of Guissart *et al.* (2021) ($\varepsilon = 7.1 \cdot 10^{-3}$ m^2/s^3) corresponds very well with the spectrum of the turbulence generated by the $d16M100$ grid ($\varepsilon = 6.8 \cdot 10^{-3}$ m^2/s^3). This leads to a good match of the amplitudes of vortical disturbances in the TS-frequency range $500 \leqslant f \leqslant 3000$ Hz for the two cases. Nevertheless, the integral Tu_u for $10 \leqslant f \leqslant 5000$ Hz are 0.33 % and 0.12 % in the flight measurement and in the wind tunnel respectively, a difference by nearly a factor of 3. In addition, the dissipation rate is independent of the flight speed. With increasing U_∞, the level of the power density spectrum, $E_{xx}(f)$ of the turbulence decreases and the spectrum shifts to higher frequencies. Both these effects influences the integral Tu, if a fixed frequency range is used for integrating the turbulence level. Consequently, the dissipation rate is a better descriptor for the impact of small-scale turbulence on TS-driven boundary layer transition than Tu.

The dissipation rate in the atmosphere depends on various factors including the heat flux from the sun, the weather conditions and the terrain, which is reflected in the measurements of other authors. Guissart *et al.* (2021) measured dissipation rates in flight ranging from $4 \cdot 10^{-9}$ to $8 \cdot 10^{-3}$ m^2/s^3 in conditions labeled as "calm" to "turbulent". The corresponding measured rms velocities range from 0.002 to 0.1 m/s for $20 \leqslant f \leqslant 1000$ Hz. In measurements during cross-country flight with a glider aircraft (Greiner & Würz, 2021), dissipation rates of $4.2 \cdot 10^{-4} \leqslant \varepsilon \leqslant 2.0 \cdot 10^{-2}$ m^2/s^3 were recorded in thermals and $2.0 \cdot 10^{-5} \leqslant \varepsilon \leqslant 1.0 \cdot 10^{-2}$ m^2/s^3 in the straight flight between thermals. This corresponds to $0.04 \leqslant u_{rms} \leqslant 0.2$ m/s and $0.01 \leqslant u_{rms} \leqslant 0.2$ m/s respectively for $20 \leqslant f \leqslant 1000$ Hz. The measurements of Guissart *et al.* (2021) and Greiner & Würz (2021) were both conducted in the lower, convective part of the atmosphere. At altitudes relevant for wind turbine applications (here $\lesssim$ 200 m above ground), dissipation rates commonly reported in literature fall in the range $1 \cdot 10^{-4} \lesssim \varepsilon \lesssim 1.5 \cdot 10^{-2}$ m^2/s^3, see for example Sheih *et al.* (1971), Jacoby-Koaly *et al.* (2002) and Bodini *et al.* (2018). Han *et al.* (2000) measured levels down to $1.3 \cdot 10^{-5}$ m^2/s^3 in neutral and stable atmosphere over flat terrain, a large contrast to Li *et al.* (2014) who observed dissipation rates as high as $2.2 \cdot 10^{-1}$ m^2/s^3 in storms (typhoons). Examples of other cases with high dissipation rates are the wake behind a wind turbine where Lundquist & Bariteau (2015) measured $3.5 \cdot 10^{-2} \leqslant \varepsilon \leqslant 1.1 \cdot 10^{-1}$ m^2/s^3, and above a forest, where Chougule *et al.* (2015) observed $\varepsilon \approx 5 \cdot 10^{-2}$ m^2/s^3. Comparing with the published measurements listed here, Fig. B.8b shows that the current set of grids generate turbulence with dissipation rates that covers most of the meteorological conditions experienced by glider aircraft and wind turbines.

B.4. Characteristic length scales

The scales of atmospheric turbulence span a wider range compared to the size of disturbances that can be generated in a wind tunnel. In the following section the integral length scale Λ, the Taylor length scale λ and the Kolmogorov microscale η, are used to characterize the wind tunnel environment, see Romano *et al.* (2007). Data for grids LT3 and E of Kurian & Fransson (2009) are used for comparison. However, Kurian and Fransson did not have a contraction between the grid and the test section, which limits a direct comparison.

It should be noted that in the LWT, the case without turbulence grid exhibits an exceptionally low level of turbulence ($Tu_u^x \leqslant 0.02\%$) and parts of the measured spectra are a combination of vortical and acoustic modes as well as electronic noise of the hot-wire equipment. On one hand this translates into an increased uncertainty in the calculation of the dissipation rate and the characteristic length scales for the "no grid" configuration. On the other hand, the low Tu provides a very low background level for the grid cases and can be neglected when processing the grid results.

The integral length scale Λ is a measure for the large-scale turbulence structures, and various methods can be used for its estimation, see Nandi & Yeo (2021). Here, the single point autocorrelations in the x_t-direction of the respective velocity signals are used to determine the integral time scales, which in turn are transformed to length scales using the Taylor hypothesis of frozen turbulence in the streamwise direction (Kaimal & Finnigan, 1994). It should be noted that for v and w, this method determines different elements of the length scale tensor than those derived from the corresponding two-point correlations in y_t and z_t-direction, see Kamruzzaman *et al.* (2012). For a discussion on the relation between integral length scales determined from single and two-point correlations, see e.g. Devenport *et al.* (2001) and Kamruzzaman *et al.* (2012). Here, the integral length scale of the u-component, Λ_u is defined as

$$\Lambda_u = U_\infty \int_0^\infty \frac{\overline{u'(t)u'(t+\Delta t)}}{\sigma_u^2} d\Delta t \tag{B.4}$$

where t is an instance in time, Δt is a time lag with respect to t and σ_u is the standard deviation of the u-velocity.

The integral length scales for the velocity components v and w, (Λ_v and Λ_w) are evaluated correspondingly by substituting the respective velocity components and standard deviation under the integral. Determining the integral in Eq. B.4 from experimental data can be an intricate procedure, depending on the shape of the autocorrelation function. Here, Λ is determined as the correlation length at which the autocorrelation of the velocity signal drops

below the level $1/e$, see Romano *et al.* (2007). This method, sometimes referred to as the exponential method, is reported by Azevedo *et al.* (2017) and Trush *et al.* (2020) to be more consistent and repeatable than using the first minimum or the zero crossing of the auto correlation function. In general, the exponential method results in somewhat lower values of the integral length scale compared to other methods.

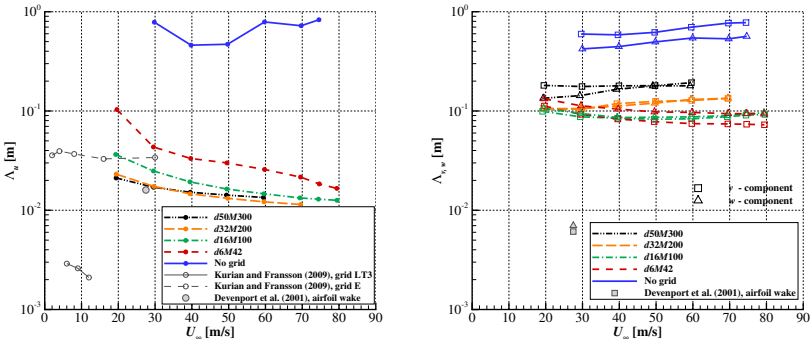

(a) u velocity component.

(b) v and w velocity components.

Figure B.9.: Integral length scale Λ for the different grids as function of U_∞. Λ is based on the autocorrelation in the streamwise direction. From Romblad *et al.* (2022*a*)[8].

The turbulence generated by all four grids exhibits integral length scales Λ_u in the range of $0.011 < \Lambda_u < 0.10$ m in comparison to $\Lambda_u \sim 0.6$ m without grid. For all grids, the integral length scale decreases with increasing U_∞. Although it constitutes a different flow situation, the $\Lambda_u = 0.016$ m measured by Devenport *et al.* (2001) in the fully developed wake 8.33 chords (1.69 m) downstream a NACA0012 airfoil at $Re = 3.28 \cdot 10^5$, falls within the range of the current measurements. The current values of Λ_u are also comparable to those measured by Kurian & Fransson (2009) for grid E, but significantly larger than those for grid LT3. It should be noted that the turbulence in Kurian & Fransson (2009) was not influenced by a contraction. The different grids of Kurian & Fransson (2009) were designed to generate turbulence with approximately the same Tu-level, but covering a large range of length scales. This explains the large difference in Λ_u between grids E and LT3. In the current measurement, Λ_u decreases for coarser grids (Fig. B.9a), with the exception of the $d50M300$ grid. In contrast, Kurian & Fransson (2009) found

[8] Used under Creative Commons Attribution 4.0 International License, http://creativecommons.org/licenses/by/4.0/

an increase of Λ_u for coarser grids, a difference that may be linked to a) the influence of the contraction in the current measurement, as well as b) Kurian & Fransson (2009) performing their measurements at constant $x_t/M = 100$, rather than at constant x_t. In the current study $x_t = 6.7$ m is used, see Table 2.2-1. A constant x_t reflects the impact of the grids in the intended NLF airfoil tests, where the model is mounted at the center of the test section turntable.

For the transverse velocity components seen in Fig. B.9b, the three finer grids all show integral length scales in the order of $\Lambda_v \sim \Lambda_w \sim 0.1$ m whereas the $d50M300$ grid and the case without grid generate integral length scales in the order of 0.2 m and 0.5 m respectively. These are significantly higher values compared to the Λ_v and $\Lambda_w \sim 0.006 - 0.007$ m measured by Devenport *et al.* (2001) and reflects the anisotropy of large scales in the current investigation.

The present measurements exhibit no consistent trend between the grids for the ratio $\Lambda_v\ /\Lambda_w$. For grids $d16M100$ and $d32M200$ we find $\Lambda_v\ /\Lambda_w \approx 1$, although for the case without grid and for $d50M300$ at $U_\infty < 40$ m/s a ratio of $\Lambda_v\ /\Lambda_w > 1$ is observed. For the grid $d6M42$ the relation is reversed, with $\Lambda_v/\Lambda_w < 1$. It is possible that the relation between Λ_v and Λ_w is linked to the differences between the horizontal (y_t) and the vertical (z_t) direction in the contraction ratio as well as in the test section dimensions, but the contradicting trends in Fig. B.9b do not allow a clear conclusion to be drawn from the present data.

For isotropic turbulence one would expect $\Lambda_u \approx 2\Lambda_v \approx 2\Lambda_w$, see e.g. Devenport *et al.* (2001) and Kamruzzaman *et al.* (2012). In the present measurements the ratio is reversed, with Λ_v and Λ_w being up to 14 times larger than Λ_u. This is a direct consequence of the attenuation of large turbulence scales in the longitudinal direction, which is caused by the contraction in the inlet section of the tunnel, see Sect. 2.2. In fact, this is one of the most obvious drawbacks of installing turbulence grids upstream of the contraction. It remains open to further investigations to quantify the impact of the scale dependent anisotropy on transition scenarios of NLF airfoils.

It is common practice to define the so-called macro-scale Reynolds number, or turbulent Reynolds number, using the integral length scale

$$Re_{\Lambda u} = \frac{u_{rms} \cdot \Lambda_u}{\nu} \tag{B.5}$$

with Re_{Λ_v} and Re_{Λ_w} defined correspondingly. See Table 2.2 for the ranges of Re_Λ of the present measurements.

The Taylor microscale, λ describes the size of intermediate flow structures. Following Romano *et al.* (2007), the Taylor microscale is estimated by fitting a parabola to the correlation function in the vicinity of correlation length

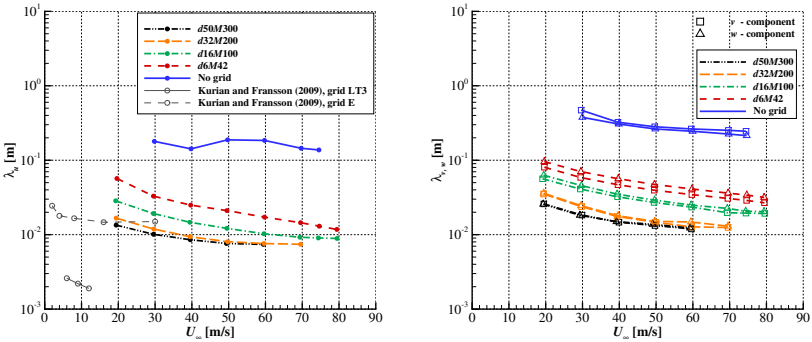

(a) u-component. (b) v and w-components.

Figure B.10.: Taylor length scale λ for the different grids as function of U_∞. From Romblad *et al.* (2022*a*)[9].

$r_x = 0$. The correlation length at which the parabola intersects the r_x axis represents the Taylor length scale. Analogous to the integral length scale, the autocorrelation in the x_t-direction is employed for all the three velocity components. Hallbäck *et al.* (1989) present a correlation-based method for determining Taylor scales, in which the range of correlation length for the analysis is selected to provide adequate resolution while avoiding problems with noise and AD-converter resolution. On the current dataset, the two methods yield similar results, but the method of Romano *et al.* (2007) was found to be slightly more robust.

The Taylor length scales of the turbulence generated by the four grids cover the ranges $7.4 \cdot 10^{-3} < \lambda_u < 57 \cdot 10^{-3}$ m and $12 \cdot 10^{-3} < \lambda_v$, $\lambda_w < 96 \cdot 10^{-3}$ m, see Fig. B.10. The range for λ_u corresponds well with the $15 \cdot 10^{-3} < \lambda_u < 25 \cdot 10^{-3}$ m reported by Kurian & Fransson (2009) for their coarser grid E. In contrast, their LT3 grid generates turbulence with smaller Taylor scales, $2.1 \cdot 10^{-3} < \lambda_u < 2.9 \cdot 10^{-3}$ m. In the current measurements, coarser grids and increasing U_∞ shortens the Taylor length scales. Kurian & Fransson (2009) measured largely similar trends with U_∞, but the reversed behavior with respect to grid dimensions.

Similar to the definition of Re_Λ, the micro-scale Reynolds number is defined as

$$Re_{\lambda u} = \frac{u_{rms} \cdot \lambda_u}{\nu} \tag{B.6}$$

with $Re\lambda_v$ and $Re\lambda_w$ following the same pattern. The ranges of Re_λ of the

present measurements can be found in Table 2.2.

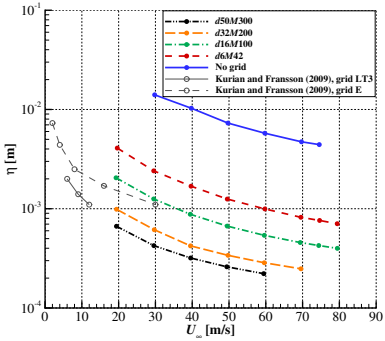

Figure B.11.: Kolmogorov length scale η for the different grids as function of U_∞. From Romblad *et al.* (2022*a*)[10].

The smallest turbulence scales in the flow are defined by the dissipation rate and the viscosity. These scales are known as the Kolmogorov length and time scales. The following section will focus on the former of the two. The local isotropy at the higher frequencies discussed in Sect. B.3 motivates calculating the Kolmogorov length scale η according to Pope (2000)

$$\eta = \left(\frac{\nu^3}{\varepsilon}\right)^{1/4} \tag{B.7}$$

where ν is the kinematic viscosity and ε is the dissipation rate.

The Kolmogorov length scales determined for the four grids cover the ranges $2.2 \cdot 10^{-4} < \eta < 4.1 \cdot 10^{-3}$ m. Similar to the Taylor length scale, coarser grids and higher free-stream velocity result in a reduction of the Kolmogorov length scales, see Fig. B.11. The η levels in the current measurements are better comparable to those measured by Kurian & Fransson (2009) than is the case for Λ and λ. This is to be expected, because η depends only on how much energy is fed into the dissipation range and how fast this energy is transferred into heat by the viscosity. Increasing U_∞ shortens η in the present measurements, a trend that corresponds to the results of Kurian & Fransson (2009). However, the decrease in η currently observed for coarser grids is the opposite tendency compared to Kurian & Fransson (2009).

[10] Used under Creative Commons Attribution 4.0 International License, http://creativecommons.org/licenses/by/4.0/

[11] Used under Creative Commons Attribution 4.0 International License, http://creativecommons.org/licenses/by/4.0/

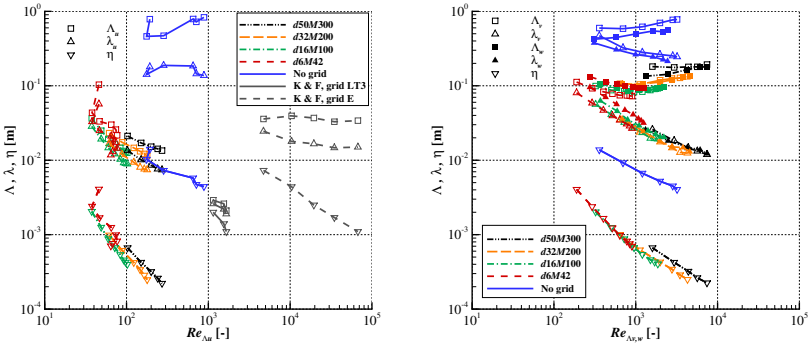

(a) u-component. (b) v and w-components.

Figure B.12.: Characteristic length scales as function of Re_Λ, including data from Kurian & Fransson (2009), designated K & F. From Romblad *et al.* (2022*a*)[11].

Figure B.12 summarizes the measured characteristic length scales by presenting them as function of the macro-scale Reynolds number, Re_Λ. Grid E (Kurian & Fransson, 2009) exhibits the expected behavior of isotropic turbulence. The integral length scale Λ_u is essentially constant over Re_Λ, as opposed to λ_u and η that decrease with increasing Re_Λ, the latter more than the former. In the current measurements, this behavior can be recognized only for the v and w-components. For the u-component, the integral length scale is closer to the Taylor scale, both in magnitude and trend with Re_Λ. This is a direct result of the contraction attenuating the larger turbulence scales of the u-component. The higher values of Re_Λ in the measurements by Kurian & Fransson (2009) are mainly a result of the higher rms-values of the velocity fluctuations in their measurements.

B.5. Normalized spectra

To facilitate comparisons between different turbulence spectra, the energy and frequency can be normalized according to Roach (1987), where

$$f_u^* = f\frac{\Lambda_u}{U_\infty} \tag{B.8}$$

$$E_{11}^* = \frac{E_{11}U_\infty}{\overline{u'^2}\Lambda_u} \tag{B.9}$$

Normalization of the v and w-components are performed correspondingly.

The normalized longitudinal spectra of the different grids collapse well together as seen in Fig. B.13a, where spectra for $U_\infty = 40$ m/s are plotted. Both the shape and the levels match well with spectra published by Roach (1987) and Kurian & Fransson (2009). The isolated peaks in the u-component spectra in the range $1 \cdot 10^{-3} < f_u^* < 1 \cdot 10^{-2}$ and at $f_u^* \approx 1 \cdot 10^{-1}$ are an effect of the blade/stator passing frequency of the tunnel fan.

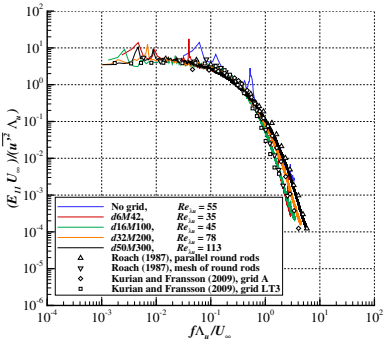

(a) u-component

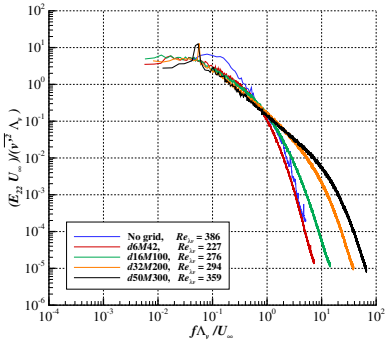

(b) v-component

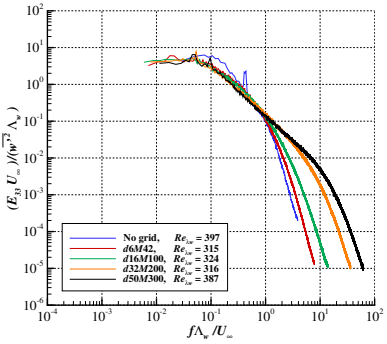

(c) w-component

Figure B.13.: Normalized spectra for the different grids at $U_\infty = 40$ m/s. From Romblad *et al.* (2022*a*)[12].

Bradshaw (1967) proposed $Re_\lambda > 100$ as criteria for the existence of an inertial subrange, based on measurements in both grid turbulence and boundary

[12] Used under Creative Commons Attribution 4.0 International License, http://creativecommons.org/licenses/by/4.0/

layers. Bradshaw's limit is significantly lower than the one found by Corrsin (1958), who suggested $Re_\lambda > 250$ from observations in turbulent pipe flow. With $35 \leqslant Re_\lambda \leqslant 113$ for the u-component in the present measurements, no extended inertial subrange is expected, which is in line with Fig. B.13a. The v and w-components (Fig. B.13b and c) show higher values, $227 \leqslant Re_\lambda \leqslant 397$, and an inertial subrange is present for the coarser grids. However, the finest grid, $d6M42$ exhibits only a hint of an inertial subrange. The more distinguished inertial- and dissipative subranges of the coarser grids, despite their lower corresponding x_t/M, suggests a slower development of the turbulence behind the finer grids. This is likely to be linked to the local Reynolds number based on the rod diameter, Re_d. The closer Re_d is to the onset of wake instability behind the rod ($Re_d \approx 40$), the more pronounced vorticity is being shed (Kurian & Fransson, 2009), thus requiring a longer distance for the turbulence to become homogenous.

Another effect contributing to the differences seen in the dissipative subrange of the longitudinal and transverse spectra of Fig. B.13 is the change in behavior of Λ with grid dimension. In the current measurements, there is a general trend toward shorter characteristic length scales for the u-component for the coarser grids. However, for Λ_v and Λ_w the trend is reversed for the all grids apart from the $d6M42$. Because Λ is related to the larger length scales, the normalization works well in the low frequency part of the transverse spectra. At the higher frequencies, to which λ and η relate, the normalization with Λ_v and Λ_w contributes to the spread of between the spectra.

The normalized spectral behavior of the turbulence generated by the grid $d32M200$ is plotted for different flow speeds in Fig. B.14. There is an increase in energy at the high frequency end of the spectra with increasing free-stream velocity, a trend most distinguishable in the transverse components. The dissipative subrange for the transverse components becomes more pronounced with increasing free-stream velocity and the inertial subrange becomes more discernible, an effect that may also be linked to Re_d, as described in the discussion of Fig. B.13 above.

The scales Λ_v and Λ_w exhibit a different behavior with U_∞ compared to the other characteristic length scales, similar to what is seen for grid the dimension in Fig. B.13b and c. This contributes to the spread between the normalized spectra in the dissipative subrange in Fig. B.14b and c.

B.6. Turbulence development in the flow direction

Two of the main characteristics which differentiates grid generated turbulence from atmospheric turbulence are 1) the significantly smaller length scales at which the turbulence is generated by the grid and 2) the absence of turbulence generation downstream of the grid. This leads to a lack of energy at the large

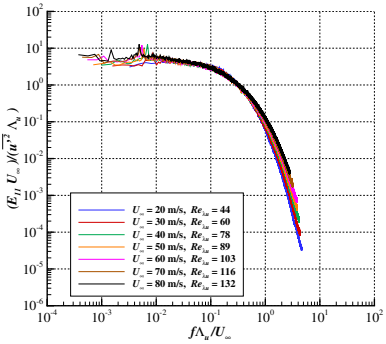

(a) u-component.

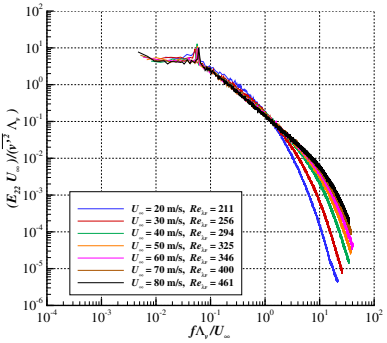

(b) v-component.

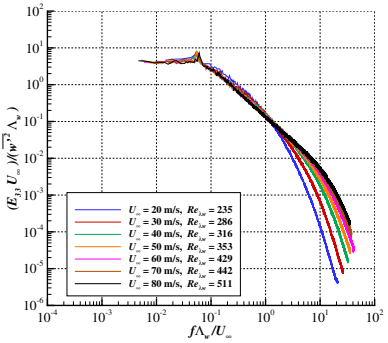

(c) w-component.

Figure B.14.: Normalized spectra for grid $d32M200$ for $20 \leqslant U_\infty \leqslant 80$ m/s. From Romblad *et al.* (2022*a*)[13].

length scales in grid generated turbulence, and the downstream development of the turbulence is dominated by energy diffusion along the Richardson-Kolmogorov energy cascade, i.e. it is a decaying turbulence.

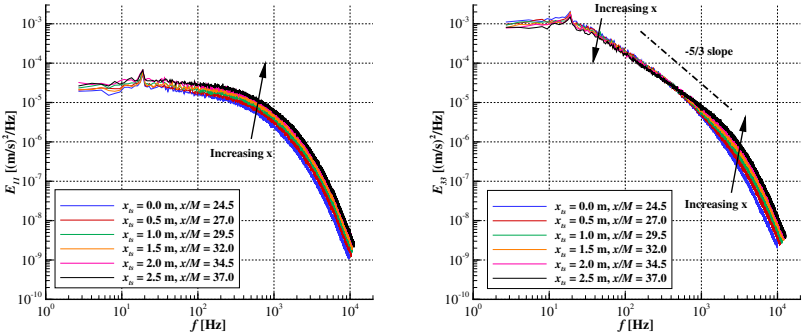

(a) u-component. (b) w-component.

Figure B.15.: Spectra for grid $d32M200$ at different streamwise positions. The distance x_{ts} refers to the start of the test section and x_t/M refers to the geometrical distance to the grids, normalized with the mesh width M. From Romblad *et al.* (2022*a*)[14].

The development of the turbulence in the free-stream direction, along the test section, was measured for the grid $d32M200$ at 40 m/s. Here, the beginning of the test section ($x_{ts} = 0$), which is located 4.9 m downstream of the turbulence grids, is used as reference. The mean velocity can be considered constant along the x_t-direction. Surprisingly, when moving downstream, the spectra in Fig. B.15a show a broadband increase of turbulence energy for the longitudinal component. In contrast, for the transverse components in Fig. B.15b, the energy decreases for frequencies below $f \approx 400$ Hz and increases for higher frequencies. The inertial subrange of the transverse turbulence is developing progressively and the dissipative subrange becomes more pronounced.

A possible interpretation of the changes in the transverse spectra is that the turbulence generated at large length scales by the grid undergoes break-up into progressively smaller eddies according to the Richardson-Kolmogorov energy cascade, transporting energy toward smaller length scales. As the ed-

[13] Used under Creative Commons Attribution 4.0 International License, http://creativecommons.org/licenses/by/4.0/

[14] Used under Creative Commons Attribution 4.0 International License, http://creativecommons.org/licenses/by/4.0/

dies become small enough, the energy is fed into the dissipation range, which becomes more pronounced further downstream. Concurrently, the flow is returning toward isotropy, in the current case redistributing energy from the transverse directions to the longitudinal (Choi & Lumley, 2001). The longitudinal turbulence sees a development of the dissipative subrange due to eddy-breakup, which is similar to the transverse component. For the larger length scales, additional energy is provided from the transverse part through the reduction of anisotropy. The combination of these two mechanisms explains the increase in turbulence energy across the frequency spectrum in the longitudinal direction.

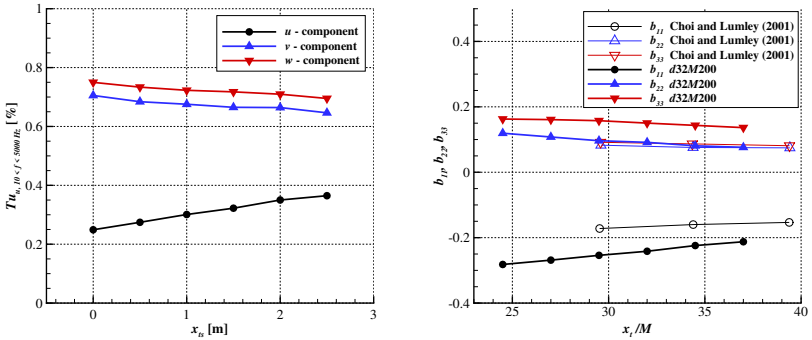

(a) Tu_u^x as function of streamwise position in the test section.

(b) b_{ii} as function of the normalized distance from the grid, x_t/M.

Figure B.16.: Tu_u^x and the principal values of the anisotropy tensor in the streamwise direction. After Romblad *et al.* (2022*a*).

As indicated by the spectra, the turbulence level in u-direction increases downstream, as opposed to the Tu in the v and w directions decreases, see Fig. B.16a. Nevertheless, the change in Tu over a typical 0.6 m airfoil chord in the center of the test section is acceptable for the intended type of investigations. The streamwise progression can also be expressed in terms of the principal values of the anisotropy tensor

$$b_{ii} = \frac{\overline{u_i' u_i'}}{2k} - \frac{1}{3} \qquad i = 1, 2, 3 \tag{B.10}$$

where b_{ii} are the principal values of the anisotropy tensor, $\overline{u_i' u_i'}$ is the mean of the square of the velocity fluctuations in direction i, and k is the turbulent kinetic energy.

With increasing distance to the grid x_t/M, the anisotropy is reduced, as

indicated by b_{ii} in Fig. B.16b. The trend corresponds well with the measurements of Choi & Lumley (2001) on the return to isotropy of turbulence downstream a 9:1 axisymmetric contraction. In the present study, the area reduction from the grid location to the test section (see Sect. 2.2.1) is 14.7 and it is larger in w than in the v-direction. This explains the higher levels of anisotropy compared to Choi & Lumley (2001) as well as the relation $b_{33} > b_{22}$ between the w and v-components. In both the present study and in the measurements of Choi & Lumley (2001), the return to isotropy appears to be faster than the dissipation of the turbulence.

B.7. Conclusion, passive turbulence grids

The generation of inflow turbulence with controlled characteristics is essential for wind tunnel investigations covering the aspects of laminar to turbulent boundary layer transition on airfoils operating in the convective part of the lower atmospheric boundary layer. In the current study, passive grids are developed specifically to approximate the characteristics of small-scale atmospheric turbulence that are relevant for nominally 2D, TS driven transition on NLF airfoils. In contrast to previous investigations (e.g. Comte-Bellot & Corrsin (1966) and Kurian & Fransson (2009)) the intended range of turbulence levels is rather low, with $Tu_u \lesssim 0.5\%$. Detailed hot-wire measurements were performed to characterize the turbulence generated by four different turbulence grids placed in the settling chamber of the Laminar Wind Tunnel at the University of Stuttgart.

In a wind tunnel with a short test section, typical for aeronautical tunnels, turbulence grids placed in the settling chamber provide a more constant turbulence level along the test section, compared to grids at the entrance of the test section. However, the resulting turbulence is not isotropic. The measured turbulence spectra of the u-component shows the typical suppression of larger length scales caused by the contraction between the location of the grids and the test section. In contrast, the spectra of the v and w-components exhibit a distinct inertial subrange, which becomes more pronounced for increasing U_∞ and coarser grids. The slope of the transverse spectra, in the inertial subrange, is less steep than the $\kappa^{-5/3}$ of the Kolmogorov spectrum. The frequency range relevant for the planned investigations on NLF airfoils is $500 \lesssim f \lesssim 3000$ Hz, corresponding to a non-dimensional viscous frequency of $40 \cdot 10^{-6} \lesssim F \lesssim 80 \cdot 10^{-6}$. In this range, the turbulence produced by the grids provides a good mapping of the spectra obtained from flight measurements in the convective part of the lower atmosphere.

Traverses across the width of the test section were performed to verify that the distance to the grid is sufficient for attaining turbulence that is homogenous in a plane perpendicular to the flow. Based on the work of

Wygnanski *et al.* (1986), it is shown that the required distance is strongly influenced by the diameter of the grid rods d and that the common expressions for minimum distance based solely on the mesh width M can be misleading.

In general, the turbulence level in both longitudinal and transverse directions increases monotonically with free-stream velocity for the two finer grids, similar to the tunnel flow without grid. For the coarser grids $d32M200$ and $d50M300$, the turbulence level Tu reaches a plateau when approaching higher flow speeds. The plateau occurs for rod diameter Reynolds numbers $Re_d \gtrsim 5000-8000$, which is only reached by the grids $d32M200$ and $d50M300$. A similar behavior is seen in the measurements of Kurian & Fransson (2009) for $Re_d \gtrsim 3000 - 6000$.

The suppression of the larger turbulence scales in the longitudinal direction, induced by the contraction, results in a frequency dependent anisotropy of the turbulence. For all four grids, the anisotropy is very large at low frequencies with $a_r = E_{11}/E_{22} \approx 0.06$ obtained for $f \lesssim 10$ Hz, above which it is gradually reduced. In the range of $900 \lesssim f \lesssim 3000$ Hz the anisotropy coefficient is fairly close to the theoretical value of isotropic turbulence of $a_r = 0.75$ (Sheih *et al.*, 1971). For higher frequencies, a_r decreases again, similar to a model spectrum proposed by Pope (2000).

A general characteristic of turbulence in wind tunnels, compared to atmospheric turbulence, is the significantly lower energy level at the lower frequency end of the spectrum. This is directly reflected in the integral turbulence level (e.g. for a frequency range of $10 \leqslant f \leqslant 5000$ Hz), which is therefore not optimally suited for quantitative comparisons related to transition experiments. The dissipation rate ε is a better descriptor for the impact of small-scale turbulence, in particular for TS-driven transition on NLF airfoils for general aviation aircraft and wind turbines. By employing the grids presented here, and including the case without grid, dissipation rates in the range of $4.4 \cdot 10^{-7} \leqslant \varepsilon \leqslant 4.0 \cdot 10^{-1}$ m^3/s^2 ($U_\infty = 40$ m/s) are achieved, which covers representative conditions for free flight and wind turbine operation.

The grids generate turbulence with integral length scales for the u-component in the ranges of $0.011 \leqslant \Lambda_u \leqslant 0.10$ m and for the v and w-components $0.07 \leqslant \Lambda_v, \Lambda_w \leqslant 0.19$ m. The range of the Taylor length scales are $7.1 \cdot 10^{-3} < \lambda_u < 57 \cdot 10^{-3}$ m and $12 \cdot 10^{-3} < \lambda_v, \lambda_w < 96 \cdot 10^{-3}$ m, and the Kolmogorov scales cover the range of $2.1 \cdot 10^{-4} < \eta < 4.1 \cdot 10^{-3}$ m. There is a general trend of shorter characteristic length scales being observed for increasing U_∞ and for coarser grids. However, the integral length scales for the v and w-components show the reversed trend related to the grid dimensions and for the coarser grids, Λ_v and Λ_w increase slightly with increasing U_∞.

The normalized spectra in the longitudinal direction collapse well together for all grids and compare favorably with the results of Roach (1987) and Kurian & Fransson (2009). For the transverse components, a wider inertial subrange followed by a distinctive dissipative subrange can be seen, in

particular for the coarser grids and higher flow speeds.

The spectral evolution in the streamwise direction of the transverse turbulence is characterized by increasingly pronounced inertial and dissipative subranges, as well as by a reduction of energy in the low frequency part, below $f \approx 400$ Hz. In contrast, the energy of the longitudinal turbulence increases across the whole frequency range when moving downstream. This is believed to be a combination of two mechanisms: 1) The absence of energy supply for the large scales and the Kolmogorov cascade which only transports energy from large scales to smaller ones, thus explaining the progressive forming of distinguished inertial and dissipative subranges. 2) The tendency of the flow to return toward isotropy, a process that here redistributes energy from the transverse directions to the longitudinal one. These trends, expressed in terms of the principal values of the anisotropy tensor along the test section, agree well with observations by Choi & Lumley (2001).